T.R.
NİĞDE ÖMER HALİSDEMİR UNIVERSITY
GRADUATE SCHOOL OF NATURAL AND APPLIED SCIENCES
DEPARTMENT OF MECHANICAL ENGINEERING

PhD THESIS

DEVELOPMENT OF A HORIZONTAL AXIS WIND TURBINE BLADE PROFILE BASED ON PASSIVE FLOW CONTROL METHODS

RIAD MORINA

FEBRUARY 2021

NİĞDE ÖMER HALİSDEMİR UNIVERSITY
GRADUATE SCHOOL OF NATURAL AND APPLIED SCIENCES

T.R.
NİĞDE ÖMER HALİSDEMİR UNIVERSITY
GRADUATE SCHOOL OF NATURAL AND APPLIED SCIENCES
DEPARTMENT OF MECHANICAL ENGINEERING

DEVELOPMENT OF A HORIZONTAL AXIS WIND TURBINE BLADE PROFILE BASED ON PASSIVE FLOW CONTROL METHODS

RIAD MORINA

Doctor of Philosophy Thesis

Supervisor

Prof. Dr. Yahya Erkan AKANSU

FEBRUARY 2021

This study titled "**Development of a Horizontal Axis Wind Turbine Blade Profile Based on Passive Flow Control Methods**" prepared from **Riad MORINA** under supervision of **Prof. Dr. Yahya Erkan AKANSU** was accepted by our jury as a Doctoral thesis in Niğde Ömer Halisdemir University Graduate School of Natural and Applied Sciences Department of **Mechanical Engineering**.

Chair : Prof. Dr. Hakan YAVUZ, Çukurova University

Member : Prof. Dr. Yahya Erkan AKANSU, Niğde Ömer Halisdemir University

Member : Prof. Dr. Murat GÖKÇEK, Niğde Ömer Halisdemir University

Member : Assoc. Prof. Dr. Mustafa SARIOĞLU, Karadeniz Technical University

Member : Asst. Prof. Dr. Mehmet Kürşat YALÇIN, Niğde Ömer Halisdemir University

APPROVAL:

This thesis was approved on …./…./20.... by the above jury members assigned by the Graduate School of Natural and Applied Sciences Board of Directors and was approved by the Institute of Directors on …./…./20.... ..... accepted by the decision.

...../...../20...

Prof. Dr. Murat BARUT
MÜDÜR

DECLARATION

I hereby declare that all the information in the thesis is obtained and presented within the framework of scientific and academic rules and that in this study prepared in accordance with the thesis rules, all kinds of statements and information that do not belong to me are fully cited.

Riad MORINA

SUMMARY

DEVELOPMENT OF A HORIZONTAL AXIS WIND TURBINE BLADE PROFILE BASED ON PASSIVE FLOW CONTROL METHODS

MORINA, Riad

Niğde Ömer Halisdemir University

Graduate School of Natural and Applied Sciences

Department of Mechanical Engineering

Supervisor : Prof. Dr. Yahya Erkan AKANSU

February 2021, 142 pages

In this thesis, the development of a horizontal axis wind turbine blade profile based on passive flow control methods was conducted experimentally. S809, S812, S822, and NACA63$_3$618 airfoils were chosen as a starting point in the process of developing a new blade profile. Based on the experimental results obtained for Reynolds numbers of $5 \cdot 10^4$ and $1 \cdot 10^5$, S822 profile was selected as the best model. The fact that the present study focuses on low Reynolds numbers, two passive flow control techniques were employed with the aim of enhancing the aerodynamic performance of the rotor by means of preventing the early flow separation along the rotor blades. In this study, leading-edge tubercles and vortex cavity techniques were adopted on blade geometry along the leading edge and upper surface. Several blade configurations for variable amplitude, wavelength, step location, step size, and step depth along the upper surface of the blades were investigated. Eleven fixed-pitch rotor configurations with diameters 0.28 m were generated and tested in the wind tunnel at chord-based Reynolds number of $4.7 \cdot 10^4$ under different free-stream conditions. Among these models, especially the model M2 has approximately 2.8% higher power coefficient than the base model and also maintains higher performance values for a wider range of tip speed ratios.

Keywords: wind turbines, small scale wind turbines, power coefficient, passive flow control techniques, wind tunnel testing, wind energy, renewable energy, blade element momentum theory.

ÖZET

PASİF AKIŞ KONTROL YÖNTEMLERİNE DAYALI YATAY EKSENLİ RÜZGAR TÜRBİNİ KANAT PROFİLİNİN GELİŞTİRİLMESİ

MORINA, Riad
Niğde Ömer Halisdemir Üniversitesi
Fen Bilimleri Enstitüsü
Makine Mühendisliği AnaBilim Dalı

Danışman : Prof. Dr. Yahya Erkan AKANSU

Şubat 2021, 142 sayfa

Bu tez çalışmasında pasif akış kontrol yöntemlerine dayalı yatay eksenli rüzgar türbini kanat profilinin geliştirilmesi deneysel olarak gerçekleştirilmiştir. Yeni kanat profili geliştirme sürecinde başlangıç noktası olarak S809, S812, S822 ve NACA 63_3618 gibi kanat modelleri seçilmiştir. En yüksek performansa sahip S822 profilinin seçimi, Reynolds sayısının $5 \cdot 10^4$ and $1 \cdot 10^5$ değerlerinde elde edilen deneysel sonuçlara göre yapılmıştır. Bu çalışmada, düşük Reynolds sayılarındaki çalışma şartlarına odaklanılması nedeniyle, rotor kanatları boyunca erken akış ayrımını önleyerek rotorun aerodinamik performansını artırmak amacıyla iki pasif akış kontrol tekniği kullanılmıştır. Bunun için türbin kanadının hücum kenarında tüberküller (dalgalı yapı) ve üst yüzeyinde girdap boşluğu teknikleri uygulanmıştır. Değişken genlik, dalga boyu, adım konumu, adım boyutu ve adım derinliği gibi kontrol yöntemi parametrelerinin çeşitli değerleri için 0.28 m çapa sahip onbir tane sabit kanat açılı rotor konfigürasyonu oluşturulmuş ve rüzgar tünelinde farklı serbest akış şartları altında veter uzunluğuna bağlı Reynolds sayısının $4.7 \cdot 10^4$ değerinde test edilmiştir. Bu modellerden özellikle M2 modeli temel modele kıyasla yaklaşık %2.5 daha fazla güç katsayısı oluşmakta ve ayrıca daha geniş bir uç hızı oranı aralığı için bu yüksek performans değerini sürdürmektedir.

Anahtar Sözcükler: rüzgar türbinleri, küçük ölçekli rüzgar türbinleri, güç katsayısı, pasif akış kontrol teknikleri, rüzgar tüneli testi, rüzgar enerjisi, yenilenebilir enerji, kanat elemanı momentum teorisi.

ACKNOWLEDGEMENTS

One of the most important factors for future energy usage is energy efficiency, in this study, leading-edge tubercles and vortex cavity flow control methods were adopted to enhance the power performance of the wind turbine. To implement this, several blade design configurations consisting of S822 airfoil type were generated by varying the geometric parameters such as amplitude, wavelength, step location, step size, and step depth. Experiments were conducted in the wind tunnel test setup for eleven blade models. This was an arduous and time-consuming process and I received valuable supports from many people during my study. First of all, I would like to thank my supervisor, Prof. Dr. Yahya Erkan AKANSU, for his sincerity, contribution, and unselfish support throughout this thesis. For this, I will always be grateful expressing my deepest appreciation for him. A special thanks go to the members of the jury: Prof. Dr. Hakan YAVUZ, Prof. Dr. Murat GÖKÇEK, Assoc. Prof. Dr. Mustafa SARIOĞLU, and Asst. Prof. Dr. Mehmet Kürşat YALÇIN who, with their comments and recommendations, gave to my thesis quality and precious value. I am also very grateful to Prof. Dr. Selahaddin Orhan AKANSU from the Kayseri Erciyes University for his kind support and hospitality all the while I was doing the lab tests in the wind tunnel. Many thanks go to Mr. Mustafa ÖZTÜRK and Mr. Yasar DOKAK for their valuable assistance during the first cycle of the wind tunnel testing since printing the airfoil profiles, making them ready for testing, and conducting experiments in the wind tunnel.

I would like to thank and appreciate Niğde Ömer Halisdemir University for the hospitality and support offered and the academic staff of our faculty for their commitment, for which I would be most thankful.

Finally, I would like to thank my wife Vlora MORINA, my lovely children Nard, Inara, and Nil, and my dear parents: Rexhep MURINA and Mejreme MURINA for their patience, understanding, courage, and continued support until the completion of my doctoral studies to whom I owe my whole life.

TABLE OF CONTENTS

SUMMARY iv
ÖZET v
ACKNOWLEDGEMENTS vi
TABLE OF CONTENTS vii
LIST OF TABLES x
LIST OF FIGURES xi
SYMBOLS AND ABBREVIATIONS xv
CHAPTER I 1
INTRODUCTION 1
1.1 Basics Of Wind Energy 4
1.1.1 The genesis of wind 4
1.1.2 Wind velocity profile 5
1.1.3 Power in the wind 7
1.2 Wind Turbines And Their Classification 10
1.3 Aerodynamics Of Wind Turbines 13
1.3.1 Airfoil characteristics 13
1.3.2 Dimensionless coefficients 13
1.3.2.1 Power, torque, and thrust coefficients 14
1.3.2.2 Lift, drag, and moment coefficients 15
1.3.2.3 Reynolds number (Re) 16
1.3.2.4 Tip speed ratio (λ) and solidity (σ) 18
1.3.3 Blade design and performance analysis 19
1.3.3.1 Blade element momentum method (BEM) 19
1.4 Flow Control Techniques 25
1.4.1 Leading edge tubercles technique 27
1.4.2 Vortex cavity – backward-facing step technique 29
CHAPTER II 31
LITERATURE REVIEW 31
2.1 Review of published studies relating to airfoil aerodynamics 31

2.2 Review of published studies relating to passive flow control techniques 35
2.3 Review of published studies relating to aerodynamics of wind turbines 38
2.4 Review of published studies relating to wind tunnel testing 42
CHAPTER III 47
SCOPE OF THE STUDY 47
Thesis outline 48
CHAPTER IV 50
METHODOLOGY AND EXPERIMENTAL SETUP 50
4.1 Wind Tunnel Description 51
4.2 Aerodynamic Testing Of Airfoils 52
4.2.1 Airfoil manufacturing 52
4.2.2 Airfoil experimental setup 53
4.2.3 Airfoil testing procedure and data recording 56
4.2.4 Blockage correction for airfoil experiments 57
4.3 Wind Turbine Rotor Blade Design And Testing 59
4.3.1 Design of the wind turbine rotor blade geometry 59
4.3.2 Generation of wind turbine blade configurations 61
4.3.3 Wind turbine experimental set-up 66
4.3.4 Wind turbine testing procedure and data recording 68
4.3.4.1 Method 1: Constant free stream velocity 68
4.3.4.2 Method 2: Constant angular velocity 68
4.3.4.3 Method 3: Constant relative velocity 69
4.3.5 Blockage correction for wind turbine experiments 72
CHAPTER V 73
EXPERIMENTAL RESULTS FOR AIRFOIL TESTING AND COMMENTS 73
5.1 Airfoil Testing Results 73
5.1.1 Experimental results for S809 airfoil 73
5.1.2 Experimental results for S812 airfoil 77
5.1.3 Experimental results for S822 airfoil 81
5.1.4 Experimental results for NACA63$_3$618 airfoil 85
CHAPTER VI 90
EXPERIMENTAL RESULTS FOR WIND TURBINE TESTING AND COMMENTS .. 90
6.1 Wind Turbine Experimental Test Results 90
6.1.1 Pre-experimental testing results 90

6.1.1.1 Determination of average power coefficient curve 90
6.1.1.2 Wind tunnel blockage corrections 95
6.1.2 M1 rotor model experimental results 96
6.1.3 M2 rotor model experimental results 97
6.1.4 M3 rotor model experimental results 98
6.1.5 M4 rotor model experimental results 99
6.1.6 M5 rotor model experimental results 100
6.1.7 M6 rotor model experimental results 101
6.1.8 M7 rotor model experimental results 102
6.1.9 M8 rotor model experimental results 103
6.1.10 M9 rotor model experimental results 104
6.1.11 M10 rotor model experimental results 105
6.1.12 M11 rotor model experimental results 106
6.1.13 Summary of wind turbine power coefficient graphs 107
CHAPTER VII 113
CONCLUSIONS 113
REFERENCES 115
APPENDICES 130
CURRICULUM VITAE 141
PUBLICATIONS PRODUCED DURING THESIS WORK 142

LIST OF TABLES

Table 4.1. Geometric characteristics of the airfoil models 54
Table 4.2. Chord and twist distributions of original scale wind turbine blade..... 60
Table 4.3. Chord length and twist angle distributions of scaled wind turbine blade 60
Table 4.4. M1 – Base rotor blade model 62
Table 4.5. M2 – Tubercled rotor blade model - A1λ3.5 62
Table 4.6. M3 – Tubercled rotor blade model – A2λ5 63
Table 4.7. M4 – Tubercled rotor blade model – A3λ7 63
Table 4.8. M5 – Tubercled rotor blade model – A4λ9 63
Table 4.9. M6 – Tubercled rotor blade model – A5λ14 64
Table 4.10. M7 – Vortex cavity rotor blade model – X30cL10cD20t 64
Table 4.11. M8 – Vortex cavity rotor blade model – X40cL20cD35t 64
Table 4.12. M9 – Vortex cavity rotor blade model – X50cL25cD19t 65
Table 4.13. M10 – Vortex cavity rotor blade model – X50cL30cD50t 65
Table 4.14. M11 – Vortex cavity rotor blade model – Hybrid (M2+M9) 65

LIST OF FIGURES

Figure 1.1. Renewables share on world total primary energy consumption (TPEC) in 2019 (Looney, 2020) 1
Figure 1.2. World wind power capacity installed until 2019 (Lee and Zhao, 2020) 2
Figure 1.4. Natural phenomenon of the wind cycle creation (adapted from Reynolds *et al.*, 2017) 5
Figure 1.6. Averaged wind velocity profiles (adapted from EWEA, 2009) 6
Figure 1.7. Power curves (adapted from Xiao *et al.,* 2020) 9
Figure 1.8. Wind turbine components (URL-2) 10
Figure 1.9. Wind turbine types: a) horizontal axis wind turbine, b) Darrieus wind turbine (Hau, 2016), and c) Savonius wind turbine (URL-3) 11
Figure 1.10. Small wind turbine model (Wood, 2011) 12
Figure 1.11. Airfoil geometry features (Bertin and Cummings, 2013) 13
Figure 1.12. Airfoil aerodynamic coefficients (adapted from Gasch and Twele, 2012) 16
Figure 1.13. The range of typical application of Reynolds numbers (Corda, 2017) 17
Figure 1.14. Discretization of the rotor blade according to BEM theory (Burton *et al.*, 2011) 20
Figure 1.15. Laminar separation bubble formation (adapted from Mo and Rho, 2020) 26
Figure 1.16. The wavy shape of the humpback whale flippers (URL-1) 27
Figure 1.17. The wave shape airfoil characteristics (Wei *et al.*, 2015) 28
Figure 1.18. The leading edge tubercles technique modele implemented on the blade (present study) 28
Figure 1.19. The wave shape airfoil characteristics (Hansen *et al.*, 2009) 28
Figure 1.20. Backward-facing step airfoil geometric parameters: c - chord length, x_u - step location, d_u - step depth, and l_u - step length (Finaish and Witherspoon, 1998) 29
Figure 1.21. The vortex cavity implemented on the upper surface of the blade (present study) 30
Figure 4.1. Niğde Ömer Halisdemir University open-circuit wind tunnel with closed test section 51
Figure 4.2. Airfoil profile in the process of printing 52

Figure 4.3. Final state of an airfoil profile 52
Figure 4.4. 2D schematic view of wind tunnel experimental setup 53
Figure 4.5. Selected airfoil section models for experimental investigation 53
Figure 4.6. Airfoil model with endplates 54
Figure 4.7. The airfoil profile mounted inside test section and in the load cell-rotary unit 56
Figure 4.8. Micromanometer device type ManoAir 500 56
Figure 4.9. Orientation of the positive and negative angles of attack 57
Figure 4.10. Small scaled wind turbine rotor model 66
Figure 4.11. Wind turbine placed in the test section 66
Figure 4.12. The digital torque and tachometer sensor DYN-200 67
Figure 4.13. DC motor graphite brushed Maxon RE50 Ø50 mm 67
Figure 4.14. Wind turbine experimental setup 67
Figure 4.15. Illustration of the wind tunnel setup for wind turbine testing 68
Figure 4.16. Electronic load unit (Rigol DL3021 Precision) 70
Figure 4.17. DC power supply (TT T-ECHNI-C YH-605D) 70
Figure 4.18. Optical laser rpm sensor (Monarch Instrument ROS) 71
Figure 4.19. Frequency inverter (Schneider electric, Altivar 71, 4 kW) 71
Figure 5.1. Lift curves for S809 at Re = $5 \cdot 10^4$ 74
Figure 5.2. Drag curves for S809 at Re = $5 \cdot 10^4$ 74
Figure 5.3. Lift to drag ratio curves for S809 at Re = $5 \cdot 10^4$ 75
Figure 5.4. Lift curves for S809 at Re = $1 \cdot 10^5$ 76
Figure 5.5. Drag curves for S809 at Re = $1 \cdot 10^5$ 76
Figure 5.6. Lift to drag curves for S809 at Re = $1 \cdot 10^5$ 77
Figure 5.7. Lift curves for S812 at Re = $5 \cdot 10^4$ 78
Figure 5.8. Drag curves for S812 at Re = $5 \cdot 10^4$ 78
Figure 5.9. Lift to drag curves for S812 at Re = $5 \cdot 10^4$ 79
Figure 5.10. Lift curves for S812 at Re = $1 \cdot 10^5$ 80
Figure 5.11. Drag curves for S812 at Re = $1 \cdot 10^5$ 80
Figure 5.12. Lift to drag curves for S812 at Re = $1 \cdot 10^5$ 81
Figure 5.13. Lift curves for S822 at Re = $5 \cdot 10^4$ 82
Figure 5.14. Drag curves for S822 at Re = $5 \cdot 10^4$ 82
Figure 5.15. Lift to drag ratio curves for S822 at Re = $5 \cdot 10^4$ 83
Figure 5.16. Lift curves for S822 at Re = $1 \cdot 10^5$ 84
Figure 5.17. Drag curves for S822 at Re = $1 \cdot 10^5$ 84

Figure 5.18. Lift to drag ratio curves for S822 at Re = $1 \cdot 10^5$ 85
Figure 5.19. Lift curves for NACA 63_3618 at Re = $5 \cdot 10^4$ 86
Figure 5.20. Drag curves for NACA 63_3618 at Re = $5 \cdot 10^4$ 86
Figure 5.21. Lift to drag ratio curves for NACA 63_3618 at Re = $5 \cdot 10^4$ 87
Figure 5.22. Lift curves for NACA 63_3618 at Re = $1 \cdot 10^5$ 88
Figure 5.23. Drag curves for NACA 63_3618 at Re = $1 \cdot 10^5$ 88
Figure 5.24. Lift to drag ratio curves for NACA 63_3618 at Re = $1 \cdot 10^5$ 89
Figure 6.1. Power coefficient curve drawn from the values obtained from the first cycle of experimental measurement 91
Figure 6.2. Power coefficient curve drawn from the values obtained from the second cycle of experimental measurement 91
Figure 6.3. Power coefficient curve drawn from the values obtained from the third cycle of experimental measurement 92
Figure 6.4. Averaged power coefficient curves of the three measurement cycles 93
Figure 6.5. Average of the three cycles and smoothed power coefficient curves 93
Figure 6.6. Smoothed power coefficient curve with measurement points 94
Figure 6.7. Power curves for the three testing methods: constant free stream velocity-variable rpm, constant rpm-variable free stream velocity, and constant relative velocity-variable rpm 95
Figure 6.8. Power curves corrected for wind tunnel blockage 96
Figure 6.9. Power coefficient versus tip speed ratio for M1 rotor model 97
Figure 6.10. Power coefficient versus tip speed ratio for M2 rotor model 98
Figure 6.11. Power coefficient versus tip speed ratio for M3 rotor model 99
Figure 6.12. Power coefficient versus tip speed ratio for M4 rotor model 100
Figure 6.13. Power coefficient versus tip speed ratio for M5 rotor model 101
Figure 6.14. Power coefficient versus tip speed ratio for M6 rotor model 102
Figure 6.15. Power coefficient versus tip speed ratio for M7 rotor model 103
Figure 6.16. Power coefficient versus tip speed ratio for M8 rotor model 104
Figure 6.17. Power coefficient versus tip speed ratio for M9 rotor model 105
Figure 6.18. Power coefficient versus tip speed ratio for M10 rotor model 106
Figure 6.19. Power coefficient versus tip speed ratio for M11 rotor model 107
Figure 6.20. Power coefficient curves of all wind turbine rotor configurations 108
Figure 6.21. Power coefficient curves of M1 rotor model and tubercled rotor configurations 109

Figure 6.22. Power coefficient curves of M1 rotor model and vortex cavity rotor configurations 110
Figure 6.23. Power coefficient curves of M1 rotor model and M11 rotor model 111
Figure 6.24. Power coefficient curves of M1 rotor model and two most efficient rotor configurations 112

SYMBOLS AND ABBREVIATIONS

Symbol	Definition
a	Axial induction factor
a'	Tangential induction factor
$\propto$	Wind shear exponent or Hellmann exponent
α_d	Design angle of attack (deg)
A	Planform area of airfoil (m^2)
α	Angle of attack (deg)
α_u	Uncorrected angle of attack (deg)
α_c	Corrected angle of attack (deg)
A_{blade}	Blade planform area (m^2)
A_R	Rotor swept area (m^2)
A_m	Amplitude (m)
A_{ts}	Wind tunnel cross-sectional area (m^2)
B	Number of blades
β	Twist angle (deg)
β_i	Local twist angle (deg)
c	Chord length (m)
c_i	Local chord length (m)
C_n	Axial force coefficient
C_{Betz}	Maximum theoretical power coefficient according to Betz
$C_{n,i}$	Local axial force coefficient
C_t	Tangential force coefficient
$C_{t,i}$	Tangential force coefficient
C_L	Lift coefficient
C_{Lu}	Uncorrected lift coefficient
C_{Lc}	Corrected lift coefficient
C_D	Drag coefficient
C_{Du}	Uncorrected drag coefficient
C_{Dc}	Corrected drag coefficient

C_M	Pitching moment
C_P	Power coefficient
C_{P_c}	Power coefficient
C_{P_u}	Power coefficient
C_Q	Torque coefficient
C_T	Thrust coefficient
d	Zero plane displacement (m)
d_r	Width of blade element (m)
D	Rotor diameter (m)
D_F	Drag force (N)
D_u	Step depth (m)
ε_T	Total correction factor
ε_{SB}	Solid blockage correction factor
ε_{WB}	Wake blockage correction factor
f	Coriolis parameter
F	Total Prandtl correction factor
F_i	Local total Prandtl correction factor
F_n	Axial force (N)
$F_{n,i}$	Local axial force (N)
F_t	Tangential force (N)
$F_{t,i}$	Local tangential force (N)
F_{tip}	Tip loss correction factor
$F_{tip,i}$	Local tip loss correction factor
F_{hub}	Hub loss correction factor
$F_{hub,i}$	Local hub loss correction factor
φ_i	Local inflow angle (deg)
h_{ts}	Height of the test section (m)
H	Height of the object or obstacle (m)
κ	von Karman constant
K	Vertical wing spaning
L_F	Lift force (N)
L_u	Step length (m)
λ	Tip speed ratio

λ_i	Local tip speed ratio
λ_d	Design tip speed ratio
λ_m	Wavelength (m)
M_F	Moment force (Nm)
ν	Air kinematic viscosity (m^2/s)
μ	Air dynamic viscosity (kg/m·s)
n	Rotor rotational speed (rpm)
Ω	Earth's rate of rotation (rad/s)
P_i	Power generated by a blade element (W)
P_{wind}	Power available in the wind (W)
P_{Betz}	Maximum power extractable in the wind according to Betz (W)
P_{out}	Power generated (W)
q	Dynamic pressure (Pa)
q_u	Uncorrected dynamic pressure (Pa)
q_c	Corrected dynamic pressure (Pa)
Q	Tangential force or torque (Nm)
Q_i	Local tangential force or local torque (Nm)
r_i	Local blade radius (m)
r_{root}	Radius of the blade root (m)
R	Rotor radius (m)
Re	Reynolds number
Re_u	Ucorrected Reynolds number
Re_c	Corrected Reynolds number
Re_i	Local Reynolds number
ρ	Air density (kg/m^3)
σ_i	Local solidity (%)
σ_R	Rotor solidity (%)
σ_{sc}	Streamline curvature correction factor
t	Thickness of airfoil (%c)
Θ	Latitude (degree)
u_*	Friction velocity in air (m/s)
U_{A_F}	Uncertainty in the airfoil frontal area (%)
U_c	Uncertainty in the chord length of airfoil (%)

$U_{c_{11}}$	Uncertainty in the tip chord length (%)
U_{C_L}	Uncertainty in the lift coefficient (%)
U_{C_D}	Uncertainty in the drag coefficient (%)
U_D	Uncertainty in the rotor diameter (%)
U_{F_L}	Uncertainty in the lift force (%)
U_{F_D}	Uncertainty in the drag force (%)
U_{C_P}	Uncertainty in the power coefficient (%)
$U_{P_{atm}}$	Uncertainty in the atmospheric pressure measurement (%)
U_Q	Uncertainty in the torque (%)
U_r	Uncertainty in the experimental result (%)
U_{R_e}	Uncertainty in the Reynolds number (%)
U_R	Uncertainty in the blade radius (%)
U_{T_∞}	Uncertainty in the air temperature (%)
U_{V_R}	Uncertainty in the tip blade speed (%)
U_V	Uncertainty in the freestream velocity (%)
U_λ	Uncertainty in the tip speed ratio (%)
U_ρ	Uncertainty in the air density (%)
U_μ	Uncertainty in the air viscosity (%)
V	Wind speed (m/s)
V_u	Uncorrected wind speed (m/s)
V_c	Corrected wind speed (m/s)
V_d	Design wind speed (m/s)
V_m	Model volume (m^3)
V_R	Blade tip speed (m/s)
$V(z)$	Wind profile at height z (m/s)
V_{rel}	Relative velocity (m/s)
$V_{rel,i}$	Local relative velocity (m/s)
V_g	Geostrophic wind speed (m/s)
ω	Angular speed (rad/s)
X_u	Step location (m)
γ	Length scale
z_0	Surface roughness length (m)

z	Height above ground (m)
z_r	Reference height above ground according to WMO (10 m)
Z_S	Surface layer height (m)
Z_G	Geostrophic wind at given height (m)

Abbreviation	**Description**
BEMT	Blade element momentum theory
BloomberNEF	Bloomberg new energy finance
CFD	Computational fluid dynamics
DTU	Danish technical university
DNV GL	Det norske veritas germanischer lloyd
EWEA	European wind energy association
EIA	Energy information administration
GWEC	Global wind energy council
GW	Gigawatt
HAWT	Horizontal axis wind turbine
IEC	International electromechanical commission
IEA	International energy agency
IRENA	International renewable energy agency
NREL	National renewable energy laboratory
REN21	Renewable energy policy network for the 21st Century
TUDelf	Delf university of technology
TPEC	Total primary energy consumption
TWh	Terawatt hour
VAWT	Vertical axis wind turbine
WMO	World meteorology oranization

CHAPTER I

INTRODUCTION

A long time ago the wind energy was used by humankind mainly to replace the body force, which was not sufficient for them to perform their physical work. With the increase of life quality and advances in technology, the needs of humankind also changed. Nowadays, the wind as a renewable energy source is estimated to become a source of hope for a better life, without pollution, being present everywhere on the earth's surface and sufficient to provide the world's needs for energy more than a few times.

According to data published by (Looney, 2020), it is seen that about 12% of the total global primary energy consumption (around 160,000 TWh) was provided by renewables such as wind (~1%), solar (0.5%), hydro (3%), geothermal and biomass (~8%), while about one-fifth of it was in the form of electricity (Figure 1.1). In some scenarios projected by DNV GL Energy (2020), U.S. EIA, (2019), Letcher, (2017), Sumathi *et al.*, (2015), the share of fossil fuels is expected to decrease from about 80% in 2019 to nearly 50% by 2050.

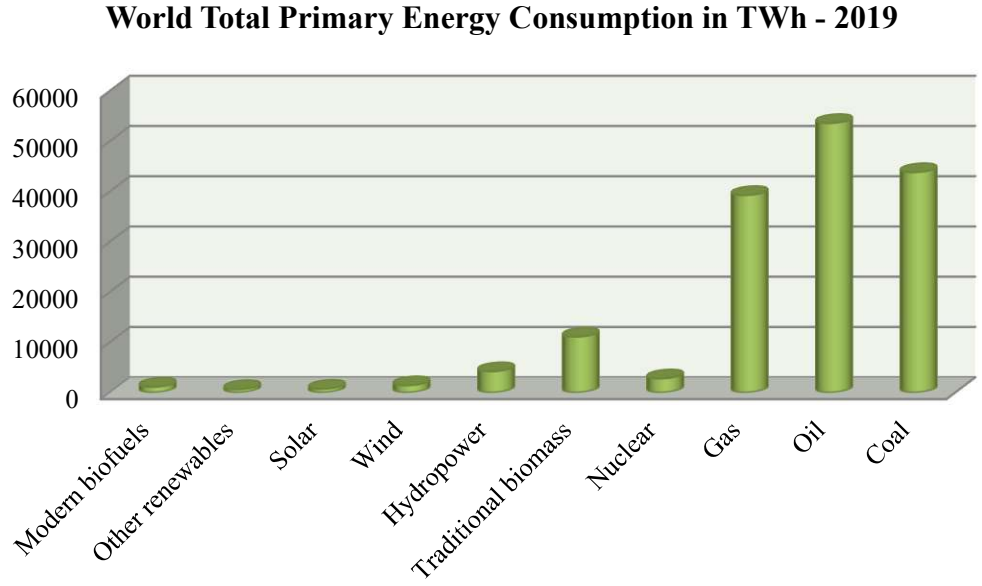

Figure 1.1. Renewables share on world total primary energy consumption (TPEC) in 2019 (Looney, 2020)

As a matter of fact, until 2019 around 651 GW (621 GW onshore, 30 GW offshore) of wind power capacity was installed globally which represents an increase of forty times more since 2000 (Lee and Zhao, 2020) (Figure 1.2). The global small scale wind turbine power capacity was about 1727 MW in 2018 (www.statista.com).

Also, based on recent analysis conducted by several international organizations dealing with renewable energy such as IEA, IRENA, REN21, BloombergNEF, etc, they give the forecast that the global demand for energy will increase less than 2% per year over the next three decades mostly with the increase of global population and living standard. It is also projected that the electricity demand will increase by approximately two times more than in 2019 whereas the share of wind energy is expected to rise by 10% from about 1% in 2019. On the other hand, the global requirements derived from the Paris Agreement (2015) for reducing air pollutants and more extensive and efficient use of clean energy from nature, have simulated the need of increasing the existing renewable energy capacities and reduce dependence on traditional sources such as: coal (28%), oil (34%), and natural gas (25%), as the heaviest environmental pollutants (Looney, 2020).

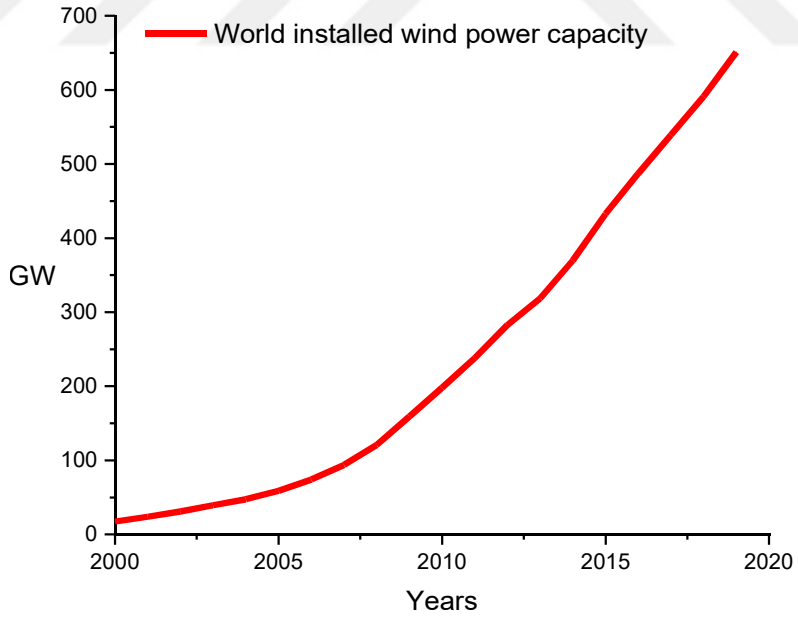

Figure 1.2. World wind power capacity installed until 2019 (Lee and Zhao, 2020)

However, to meet this growing trend of global energy demand and at the same time reaching the objectives derived from the international commitment to keep the global temperature rise below 2 degrees within this century, require an almost equal share of

renewable energy with respect to fossil fuels that currently occupy more than 80% of the world's needs for energy (www.ourworldindata.org).

Another very important factor for future energy usage is the energy efficiency in general and in this case study the efficiency of wind harvesting systems, in particular, that is an invisible source of energy since more energy can be gained by using it and can affect directly the demand for primary energy (Hasanuzzaman and Rahim, 2020).

Generally, the wind machines are distinguished mainly by the rotor shaft orientation: horizontal and vertical one, and consists of components that serve to harvest the wind energy, ensure the system is functioning, and offers the stability of the structure as a whole. In fact, horizontal axis wind turbines are more powerful when it comes to performance than the vertical shaft turbines, therefore it is more common to observe them with extraordinary sizes and capacities.

The wind turbine performance is attributed precisely to the aerodynamic efficiency of the rotor blades, whose structure is built from a single or different type of airfoils along the blade span.

In this thesis, a dedicated airfoil with the highest level of aerodynamic performance that will show in different Reynolds number regimes will be selected and then utilized as a base profile to generate the three-dimensional shape of the rotor blades.

In this study, two passive fluid flow control methods will be used with the aim of developing an existing blade profile to improve the aerodynamic efficiency, starting behavior, and to ensure the smooth operation of the small wind turbine under low Reynolds number regime. With tubercles added on the leading-edge and vortex cavity (backward-facing step) along the upper surface (suction side), several configurations will be generated separately to determine the efficiency of each technique. The cases selected for application in this subject are supported by scientific sources.

The purpose of this thesis is to study the performance improvement potential of small wind turbine blades under low Reynolds number regime and off-design conditions by applying two passive flow control methods. This study will be experimental and the

performance of all blade configurations will be tested in a low-speed open-circuit wind tunnel with closed test-section at a low chord-based Reynolds number of $4.7 \cdot 10^4$ under different free stream conditions.

1.1 Basics Of Wind Energy

In the global context, the winds never stop, day and night, every season of the year and as such present an extraordinary energetic potential therefore it shall be used since it is renewable and a clean source from nature. In fact, efforts have to be made in finding ways or technologies for more efficient use of this kinetic wind energy with minimum costs, as well, as depositing or retaining it for a longer time or for other applications.

1.1.1 The genesis of wind

The sun rays manage to penetrate the earth atmosphere and heat its (curved) surface unequally (or one-fourth of Earth's surface according to Husher, 2009), causing like this the global energy transport from the equator toward the poles to compensate for this change in energy.

A slim and dense layer of air close to the ground starts to heat up through the conduction process, in which case air pressure and density decreases and via the convection mechanism, the heated air mass starts rising by leaving the place to the cold air with higher density retracted from the force of gravity and thus provoking the wind's natural cycle. Such a natural phenomenon or the cycle of wind creation is illustrated in Figure 1.4.

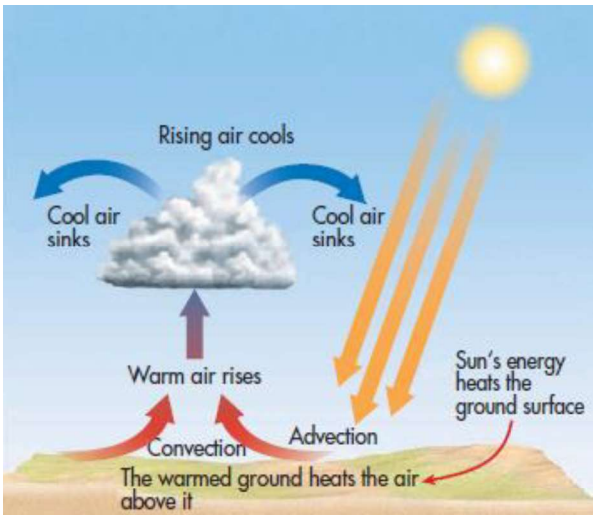

Figure 1.4. Natural phenomenon of the wind cycle creation (adapted from Reynolds *et al.*, 2017)

However, a very small percentage, around 1-2 % (Corke, 2018; Wagner, 2018; Nelson and Starcher, 2018; Hau, 2013; King, 2018) of 51% (or 696 W/m^2 from the total solar constant of 1366 W/m^2) of the total energy absorbed from the earth's surface (Ahrens, 2009; Husher, 2009) is estimated available to be harvested from the wind machines.

1.1.2 Wind velocity profile

To present the wind speed profile (Figure 1.6), based on the instructions from the International Electrotechnical Commission (IEC 61400) and recommendations from the World Meteorology Organization (WMO) for heights 10 m above ground, a couple of mathematical equations are used: logarithmic and power laws (Gasch and Twele, 2012).

Logarithmic wind profile according to Holmes (2001) is given by:

$$V(z) = \frac{u_*}{\kappa} \cdot ln\left(\frac{z}{z_0}\right) \tag{1.1}$$

For the case of very rough terrain (urban and forest areas), the height z is replaced by $(z - d)$.

Where; $V(z)$ – wind speed at height z (m/s), z – the height above ground (m), z_0 – the roughness length (m), $u_* = \sqrt{\tau/\rho_{air}}$ – the friction velocity in air (m/s), $d = (3/4) \cdot H$ – the zero-plane displacement (m), H – the height of the object or obstacle (m).

In practice, friction velocity is determined experimentally, but there are some approximately values presented by Reible (2017) which can be used as preliminary or orientation values.

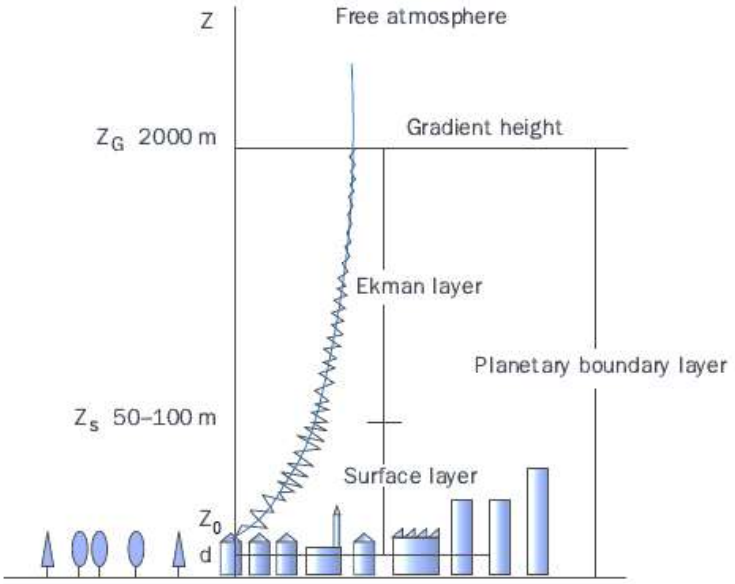

Figure 1.6. Averaged wind velocity profiles (adapted from EWEA, 2009)

Another mathematical expression to describing the wind profile which is widely in use, according to IEC 61400 standard is given by:

$$V(z) = V(z_r) \cdot \frac{ln(z/z_0)}{ln(z_r/z_0)} \tag{1.2}$$

While, power law wind profile according to IEC 61400 is defined as:

$$V(z) = V(z_r) \cdot \left(\frac{z}{z_r}\right)^{\propto} \tag{1.3}$$

Where; $V(z)$ – wind speed at height z (m/s), z – the height above ground (m), $z_r = 10$ m – the reference height above ground according to WMO, z_0 – the roughness length (m), Z_s – surface layer height (m), Z_G – geostrophic wind at a given height (m), $u_* = \sqrt{\tau/\rho_{air}}$ – the friction velocity in air (m/s), $d = (3/4) \cdot H$ – the zero-plane displacement (m), H – the height of the object or obstacle (m), $\kappa = 0.4$ – von Karman constant, $\propto$ – the wind shear exponent or Hellmann exponent.

On the other hand, the laws for the vertical presentation of wind profile in the surface layer does not serve for the Ekman layer since in this zone the Coriolis force impact is evident, therefore according to Gasch and Twele (2012) the wind speed profile in this atmospheric layer is presented with the following expression:

$$V(z) = V_g \cdot \sqrt{(1 - 2e^{-\gamma z}) \cdot coc(\gamma z) + e^{-2\gamma z}} \tag{1.4}$$

Where; $V_g = \Delta p/(f \cdot \rho \cdot d)$ – geostrophic wind speed (m/s), $\gamma = \sqrt{f/2 \cdot K_M}$ – length scale, $f = 2 \cdot \Omega \cdot \sin(\theta)$ - Coriolis parameter, $\Omega = 7.29 \cdot 10^{-5}$ – Earth's rate of rotation (rad/s), θ – latitude (degree).

In this study, the wind tunnel provides a uniform wind profile in the test section, thus experimental research will be done under these conditions.

1.1.3 Power in the wind

Our planet receives an enormous sun's energy of around 174,300 terawatts per hour and where 1-2% of it is transformed in the form of kinetic wind energy (Emeis, 2013). Of this huge amount of wind energy available, only 0.035% can be harvested from wind machines (Emeis, 2013).

The available power in the wind is given by the equation:

$$P_{wind} = \frac{1}{2} \cdot \rho \cdot V^3 \cdot A_R \ (W) \tag{1.5}$$

Where; ρ - the air density (kg/m^3), V – freestream velocity (m/s), and A_R - the rotor swept area (m^2).

The maximum theoretical power, according to Betz's theory, is defined as:

$$P_{Betz} = \frac{1}{2} \cdot \rho \cdot V^3 \cdot A_R \cdot C_{Betz} \ \ (W) \tag{1.6}$$

Where C_{Betz} = 0.593 - is the maximum power coefficient.

Meanwhile, the power output of the wind turbine can be written as:

$$P_{out} = \frac{1}{2} \cdot \rho \cdot V^3 \cdot A_R \cdot C_P \ \ (W) \tag{1.7}$$

Where C_P is the power coefficient of the wind turbine.

Also, the power generated by the wind turbine or mechanical power can be calculated by measuring the torque and angular speed in the rotor shaft using the formula:

$$P_{out} = Q \cdot \omega \ \ (W) \tag{1.8}$$

Where; Q - tangential force (N), ω – angular speed (rad/s).

As is depicted in Figure 1.7, the green curve represents the unhindered wind potential or power available in the wind which is determined using Eq. 1.5, which is the product of air density, rotor swept area, and the cube of wind speed which is the key parameter. In this context, the natural wind speed cannot be adjusted and this is the reason why nowadays it can be encountered in turbines with ever larger sizes.

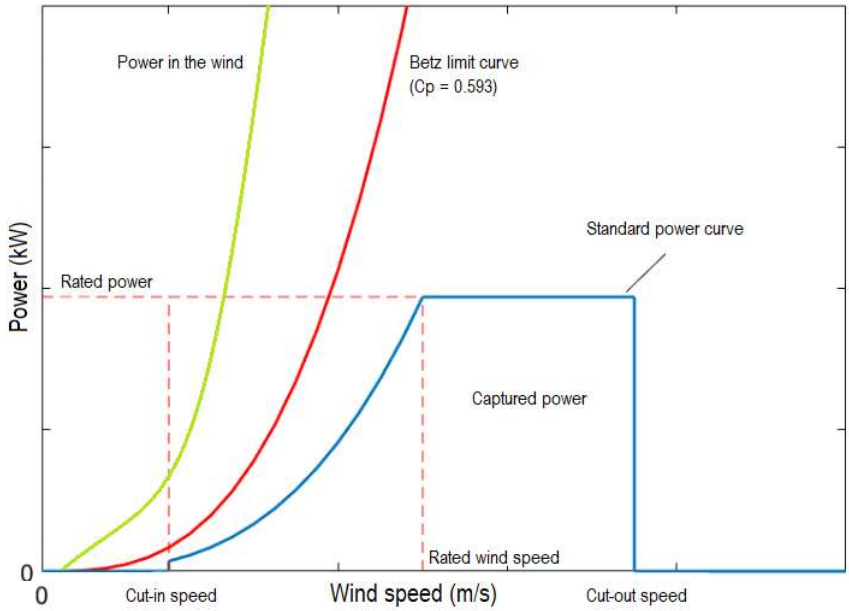

Figure 1.7. Power curves (adapted from Xiao *et al.,* 2020)

Meanwhile, in the case when a wind machine is present in the wind stream, referring to Figure 1.7 as the red power curve, this means that this machine operates at maximum efficiency or as it is otherwise known as the ideal condition defined based on some assumptions by Betz. In other words, if a machine is capable to slow down the original wind speed by one-third just before reaching the rotor blades and maintains this amount after crossing them, it is considered that the rotor is operating at an ideal condition where the speed of the wind through the blades is as much as two-thirds of the original speed (Gasch and Twele, 2012; Ragheb and M., 2011).

On the other hand, in real terms, this is difficult to achieve as many factors neglected by Betz in his theory such as losses due to free stream direction, number of blades, wake rotation (no tangential motion), rotor hub, air compressibility, heat transfer, etc., as illustrated in Figure 1.7 with the blue line power curve (Burton *et al.*, 2011; Gasch and Twele, 2012; Ragheb and M., 2011; Schubel and Crossley, 2014).

Typically, a standard wind turbine starts to operate at a wind speed of around 3 m/s and reach their maximum generation at a wind speed of up to 14 m/s, and beyond this speed limit the rotor will start to stall or shutdown at 25 m/s (Burton *et al.*, 2011; Ehrlich, 2013).

1.2 Wind Turbines And Their Classification

Overall, there are two main components of the wind turbines such as the rotor and tower. The rotor is comprised of blades and nacelle that envelopes the generator, gearbox, and other components as depicted in Figure 1.8.

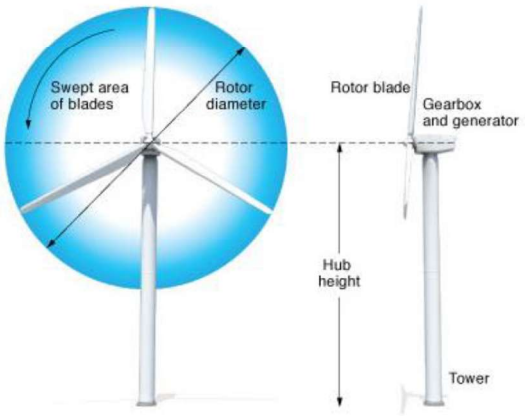

Figure 1.8. Wind turbine components (URL-2)

According to physicist Albert Betz, no wind machine can surpass the efficiency of 59.3% which represents the maximum theoretical limit or Betz's limit. To illustrate this fact with regard to some renewable energy technologies, most modern turbines have an efficiency no higher than 50% despite the advances made (Earnest and Rachel, 2019; Emeis, 2013). In this context, solar PV systems and coal-based power plant have efficiencies of about 20% and 35% respectively (King, 2018; Kishore *et al.*, 2018). To enrich the fact, the performance of small wind turbines is even lower than that of large ones with maximum efficiency from around 25% (Kishore *et al.*, 2018) to about 30% (Gipe, 2004).

The turbine rotor as the main part of the wind turbine may possess one or several blades mounted on its body but three-bladed designs are commonly in use because of some economic, aerodynamic, and structural reasons (Anderson, 2020; Rosato, 2018; Paraschivoiu, 2002) (Figure 1.9).

In principle, the higher the blade numbers the greater the efficiency, but it is argued that this characteristic affects little on rotor power (Hau, 2013). In addition, the rotor's blade geometry is built from a single or different airfoil sections along its entire length which plays a key role in the aerodynamic performance. The blade shape, due to the variable

nature of airflow, usually is tapered and twisted in its entire length to maintain its effectiveness (Burton *et al.*, 2011; Manwell *et al.*, 2010, Hansen, 2015; Letcher, 2017).

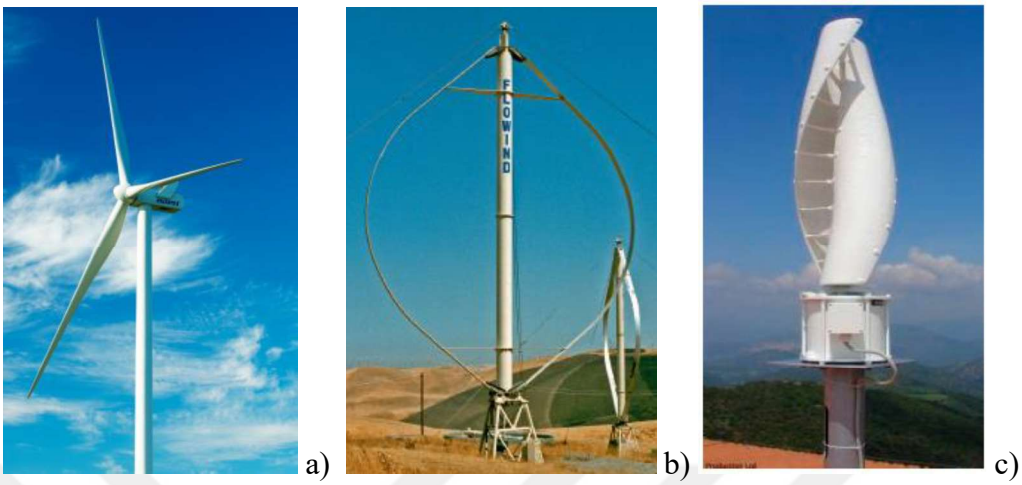

Figure 1.9. Wind turbine types: a) horizontal axis wind turbine, b) Darrieus wind turbine (Hau, 2016), and c) Savonius wind turbine (URL-3)

On the other hand, wind turbines are mainly divided into horizontal and vertical axis and consist of components that serve to harvest the wind energy, ensure the system is functioning, and offer the stability of the structure as a whole. Particularly, the horizontal axis wind turbines (HAWT) have wider use than vertical axis wind turbines (VAWT) mainly due to their higher efficiency and design issues. Generally, the maximum efficiency of a large modern HAWT achieved so far has does not exceed even 84% of the Betz's limit, while the VAWT have lower efficiency and does not exceed 40% (Kishore *et al.*, 2018).

In addition, wind turbines can be divided also by means of the orientation of the rotor relative to the wind direction as upwind, where the rotor faces the wind, and downwind where the rotor is positioned on the backside of the tower. Also, wind turbines can be build even without the gearbox and such systems known as direct-drive wind turbines.

Horizontal axis wind turbines or lift based devices can be divided into small (10 cm < D ≤ 100 cm) and large sizes (D > 5 m) and they can be upwind or downwind designs (Kishore *et al.*, 2018). On the other hand, vertical axis wind turbines can be divided into

two main types: Darrieus (lift based device) and Savonius (drag based device) (Figure 1.9). Darrieus type is among the most efficient in this group (Paraschivoiu, 2002).

Meanwhile, small scale horizontal axis wind turbines, has almost the same design as large ones but with a few minor exceptions such as they operate closer to the ground, rotate faster, simpler construction, use tail blade instead of active yaw system, etc. (Figure 1.10). Compared to large turbines, these small machines face lower efficiency which rarely exceeds 30% (Gipe, 2004) due to design specifics, proximity to the ground surface, the flow regime in which they operate, et cetera (Kishore *et al.*, 2018).

Figure 1.10. Small wind turbine model (Wood, 2011)

Despite the same structural form compared to large size wind turbines, they are more dedicated to operating at lower Reynolds numbers (below half a million). But working conditions in this flow field, especially below $2 \cdot 10^5$, is considered a very sensitive (viscous) zone that is characterized by laminar separation bubbles and can directly influence the turbine aerodynamic performance (Giguère and Selig, 1997).

In this study, small size horizontal axis wind turbines blades will be the subject of treatment.

1.3 Aerodynamics Of Wind Turbines

The design of a wind turbine consists of finding the appropriate shape of the rotor blade profile that for certain site conditions will perform best while withstanding structural loads. Also, the aerodynamic characteristics of the rotor blades are crucial elements since they affect directly the overall efficiency of the wind turbines.

1.3.1 Airfoil characteristics

When designing a wind turbine blade, great attention must be paid to the shape of the blade profile. If a blade profile required to be specially designed, it is necessary to consider the wind speed data of the candidate site. Nowadays, there are many types of special airfoils dedicated to wind turbine applications. Generally, the geometric shape of an airfoil is characterized by a rounded leading edge, the upper surface (suction side), a lower surface (pressure side), trailing edge, chord line, thickness, camber line, aerodynamic center (0.25c), pressure center. An illustration of an airfoil geometry is depicted in Figure 1.11.

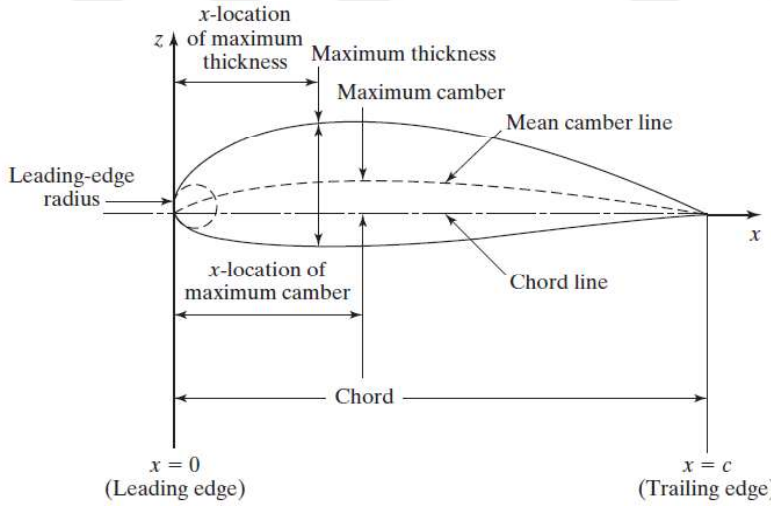

Figure 1.11. Airfoil geometry features (Bertin and Cummings, 2013)

1.3.2 Dimensionless coefficients

There are several dimensionless parameters that characterize the rotor performance and fluid flow conditions. In the following, some of the most important ones will be presented.

1.3.2.1 Power, torque, and thrust coefficients

The power coefficient is the most important aerodynamic parameter in wind turbine aerodynamics as this determines the effectiveness of the machine (Hau, 2013). The maximum theoretical power coefficient is known as the Betz's limit in honor of physicist Albert Betz.

Power coefficient is expressed as the power generated from the wind turbine divided by the power available in the wind (Manwell *et al.*, 2010):

$$C_P = \frac{P_{out}}{\frac{1}{2} \cdot \rho \cdot A_R \cdot V^3} = \frac{Q \cdot \omega}{\frac{1}{2} \cdot \rho \cdot A_R \cdot V^3} \tag{1.9}$$

Where; C_P - rotor power coefficient, A_R - swept area of the rotor (m^2), V – freestream velocity (m/s), ρ - air density (kg/m^3), P_{out} - power output (W), Q – tangetial force (N), ω – angular speed (rad/s).

Another important coefficient in the aerodynamic aspect of wind turbines is the torque coefficient (Eq. 1.10). This coefficient is related to power coefficient, tip speed ratio (λ), rotor solidity, and lift to drag ratio. The smaller the torque the greater the rotational speed of the rotor shaft, and the greater the rotational speed the smaller the solidity.

Typically, a torque coefficient value of around 0.3 can be achieved from the commercial wind turbines, but this value can descend to zero in the case of a large tip speed ratio (Twidell and Weir, 2006). Moreover, according to the author, low solidity wind turbines are characterized by a high tip speed ratio, but unfortunately, they suffer from low starting torque in contrast to large solidity ones. However, low solidity machines, typically three bladed, are used for electricity generation since the generator needs a high shaft speed of approximately 1000 to 3000 rpm (Hansen, 2015).

Torque coefficient is expressed as (Manwell *et al.*, 2010):

$$C_Q = \frac{Q}{\frac{1}{2} \cdot \rho \cdot A_R \cdot V^2} \tag{1.10}$$

Where; Q - tangential force which contribute to lift force, A_R - swept area of the rotor (m^2), V – freestream velocity (m/s), ρ - air density (kg/m^3).

The relation between power and torque coefficients is given by (Manwell *et al.*, 2010):

$$C_p = \lambda \cdot C_Q \tag{1.11}$$

The third important coefficient is the axial force or thrust coefficient and is expressed as (Manwell *et al.*, 2010):

$$C_T = \frac{T}{\frac{1}{2} \cdot \rho \cdot A_R \cdot V^2} \tag{1.12}$$

Where; T - axial force or thrust force in the wind direction, A_R - swept area of the rotor (m^2), V – freestream velocity (m/s), ρ - air density (kg/m^3).

The maximum value of the thrust coefficient is about $8/9$, which corresponds to the maximum theoretical efficiency of Betz (Gasch and Twele, 2012).

1.3.2.2 Lift, drag, and moment coefficients

These aerodynamic coefficients depend on the Reynolds number, Mach number, and angle of attack. Since the wind turbines operate in an incompressible flow regime, the Mach number (Mach < 0.3) is typically neglected (Amano and Sundén, 2014).

Lift and drag coefficients represent the main aerodynamic parameters of an airfoil as the ratio of these two quantities determines the overall aerodynamic performance level of the wind machine.

In Figure 1.12, the aerodynamic coefficients of an airfoil are illustrated.

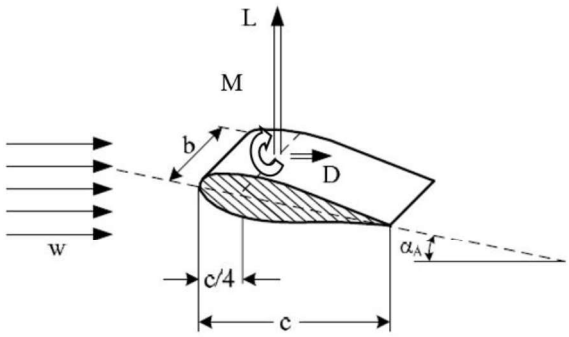

Figure 1.12. Airfoil aerodynamic coefficients (adapted from Gasch and Twele, 2012)

The lift coefficient is expressed as (Manwell *et al.*, 2010):

$$C_L = \frac{L_F}{1/2 \cdot \rho \cdot A_R \cdot V^2} \tag{1.13}$$

The drag coefficient is defined as (Manwell *et al.*, 2010):

$$C_D = \frac{D_F}{1/2 \cdot \rho \cdot A_R \cdot V^2} \tag{1.14}$$

The pitching moment coefficient is defined as (Manwell *et al.*, 2010):

$$C_M = \frac{M_F}{1/2 \cdot \rho \cdot A_R \cdot V^2 \cdot c} \tag{1.15}$$

Where; L_F - lift force, D_F - drag force, M_F - moment force acting on one-fourth the chord length, c - chord length, A_R - airfoil planform area (not projected area), V – freestream velocity (m/s), ρ - air density (kg/m^3).

1.3.2.3 Reynolds number (Re)

This non-dimensional coefficient is the main factor that characterizes the flow pattern whether is laminar or turbulent and is defined as the ratio between fluid inertial force and viscous force (Manwell *et al.*, 2010). Furthermore, aerodynamic coefficients are close related with this dimensionless number. According to Corda (2017) (Figure 1.13), the

wind turbines typically lie in the range of Reynolds numbers between 10^5 and 10^6 that is considered as a transitional flow whereas the region under $5 \cdot 10^5$ is introduced as the low Reynolds number flow regime where the small wind turbines typically operate (Giguère and Selig, 1997).

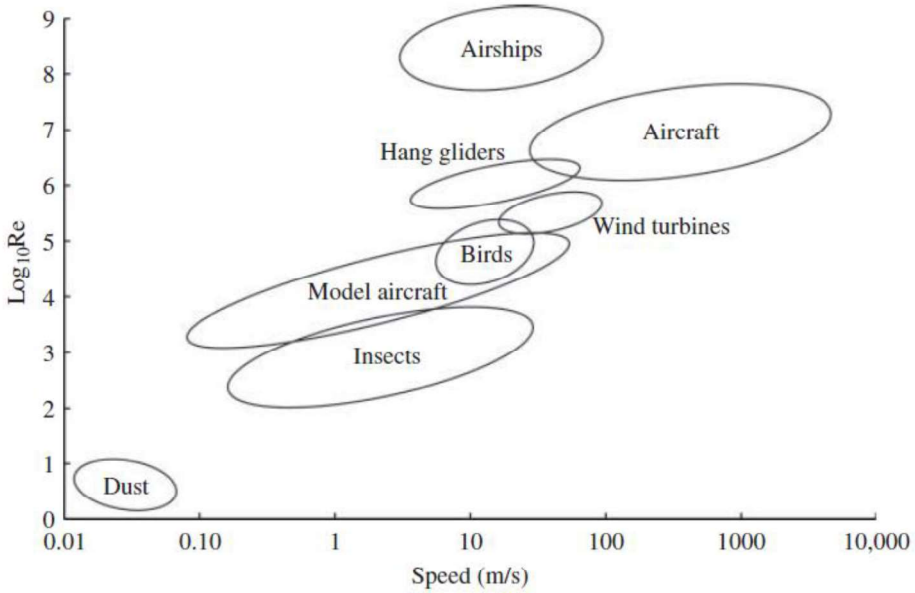

Figure 1.13. The range of typical application of Reynolds numbers (Corda, 2017)

The Reynolds number is expresses as (Manwell *et al.*, 2010):

$$Re = \frac{V_{rel} \cdot c}{\nu} = \frac{V_{rel} \cdot c}{\mu} \cdot \rho \tag{1.16}$$

Where; V – freestream velocity (m/s), V_{rel} – relative velocity of the fluid (m/s), c – chord length (m), ν – air kinematic viscosity (m^2/s), μ – air dynamic viscosity (Pa·s, $N \cdot s/m^2$, kg/m·s), ρ – air density (kg/m^3), R – rotor radius (m), ω – angular speed (rad/s).

The relative velocity on the airfoil section is given by:

$$V_{rel} = \sqrt{V^2 + {V_R}^2} \tag{1.17}$$

Where; V – freestream velocity (m/s), $V_R = R \cdot \omega$ – blade tip speed (m/s), R – rotor radius (m), ω – angular speed (rad/s).

1.3.2.4 Tip speed ratio (λ) and solidity (σ)

The tip speed ratio and solidity are the two components that determines the power performance of the rotor. Based on Betz's theory, which emphasizes the fact that no wind machine can extract more than 59.3% of the wind kinetic energy, there is an optimal value of the ratio between blade tip speed and wind speed which will provide maximum power output. Typically, for three-bladed wind turbines the optimal tip speed ratio is in the range of 3 to 10 (Sawhney, 2012; Kishore *et al.*, 2018). In this context, the rotor should not rotate so fast as to block totally the flow of air nor allow its entire mass to pass without being utilized. The higher the tip speed the more the noise level emission.

Tip speed ratio is expressed as:

$$\lambda = \frac{R \cdot \omega}{V} = \frac{R \cdot 2 \cdot \pi \cdot n}{60 \cdot V} \tag{1.18}$$

Where; R - rotor radius (m), ω - angular speed (rad/s), V – freestream velocity (m/s), n – number of revolutions per minute (rpm).

On the other hand, solidity determines the presence of the blade planform area into the rotor surface (swept area). This parameter is close related to tip speed ratio, blade numbers, and average blades planform area. With other words, three bladed wind turbines have lower solidity compared to four bladed ones, therefore they should rotate more faster. Hence, low solidity or smaller blade planform area means higher tip speed ratio. Wind turbines typically have a rotor solidity ratio in the range of around 5% up to 50% (Schmitz, 2020; Hau, 2013; Gasch and Twele, 2012; Kishore *et al.*, 2018; Anant Kishore and Priya, 2013).

Solidity ratio is expressed in two forms, local solidity which changes from root to tip of the blade due to the tapered planform area (Eq. 1.18), and rotor solidity which represents the overall solidity of the rotor (Eq. 1.19) (Ingram, 2011; Hau, 2013):

$$\sigma_i = \frac{B \cdot c_i}{2 \cdot \pi \cdot r_i} \tag{1.19}$$

$$\sigma_R = \frac{B \cdot A_{blade}}{\pi \cdot R^2} \tag{1.20}$$

Where; B – number of blades, c_i – local chord length (m), r_i – local chord radius (m), A_{blade} – planform area of the blade (m^2), R – rotor radius.

1.3.3 Blade design and performance analysis

The blade design is a very challenging and complex task as it is almost impossible to find the optimal solution with just a single effort. Usually, the design process commence with the estimation of the Reynolds number in which the rotor blades will operate, than based on this fact the most dedicated airfoil type to construct the blade is chosen. Often, Reynolds number is calculated for the tip of the rotor blades because its values vary from hub to tip. Then, the process continues with the definition of the blade's geometry (twist and chord distributions) taking into consideration the rotor diameter, airfoil type, tip speed ratio, solidity, and other design inputs. In fact, there are several approaches to design an optimal ideal blade geometry according to Betz, Schmitz (Galuert), Lissaman-Wilson, Burton, Hansen, Manwell, Schafarzyck, Hau, Eggleston, and many other formulations by several authors, or by using BEM theories, vortex wake theories, or CFD codes.

The airfoil data as a function of Reynolds number and angle of attack is readily available in the literature, and it can be obtained through software or directly can be measured in the wind tunnel.

In the presented study, Schmitz's equations presented in the following section were employed to design the blade shape.

1.3.3.1 Blade element momentum method (BEM)

This method as a starting point has the partitioning of the blade into several equal blade elements to be analyzed each independently (Figure 1.14). But initially, the blade

geometry (chord and twist distributions) must be defined in order to estimate the blade performance. It is an iterative procedure for determining the interference factors, axial and tangential induction factors. In the following, this iterative procedure is described in details according to Bakırcı and Yılmaz (2018).

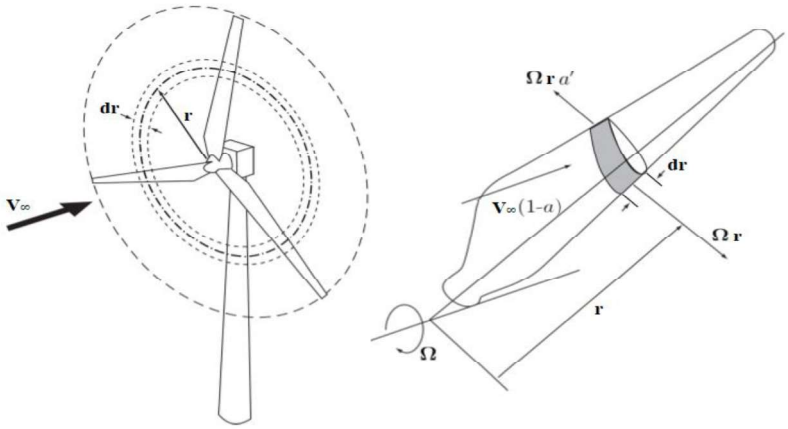

Figure 1.14. Discretization of the rotor blade according to BEM theory (Burton *et al.*, 2011)

Procedure steps;

1. Partitioning the blade into equal elements, N = 10;

2. Determination of the blade element width;

$$d_r = \frac{R - r_{root}}{N} \text{ (m)} \tag{1.21}$$

$$r_{root} = 0.2 \cdot R \text{ (m)} \tag{1.22}$$

According to Korakianitis *et al.* (2015), the root area is considered the region between 0R to 0.25R, while up to 0.95R is the midspan area, and up to 1R the tip area.

3. Calculation of local tip speed ratio;

$$\lambda_i = \lambda_d \cdot \left(\frac{r_i}{R}\right) \tag{1.23}$$

4. Calculation of local optimum relative inflow angle according to Schmitz (degrees);

$$\varphi_i = \left(\frac{2}{3}\right) \cdot atan\left(\frac{1}{\lambda_i}\right) \tag{1.24}$$

5. Calculation of local optimum chord length according to Schmitz (m);

$$c_i = \frac{16 \cdot \pi \cdot r_i}{B \cdot (C_L)_{design}} \cdot sin\left(\frac{1}{3} \cdot arctan\left(\frac{1}{\lambda_i}\right)\right)^2 \tag{1.25}$$

6. Calculation of local optimum twist angle (degrees);

$$\beta_i = \varphi_i - \alpha_{design} \tag{1.26}$$

Now, the iterative procedure is applied for each blade elements separately until the convergence is achieved. Twist angle β_i is already determined in step 6. Typically, the induction factors are set to zero for the first iteration cycle, a = a′ = 0;

7. Calculation of the local inflow angle (degrees);

$$\varphi_i = atan\left(\frac{(1-a)}{(1+a') \cdot \lambda_i}\right) \tag{1.27}$$

8. Calculation of the local angle of attack (degrees);

$$\alpha_i = \varphi_i - \beta_i \tag{1.28}$$

After calculation of the local angle of attack, corresponding C_L and C_D values for the AOA obtained are ready to be applied in steps 9 and 10.

9. Calculation of local axial force coefficient (project lift and drag coefficients normal to the rotor plane);

$$C_{n,i} = C_L \cdot \cos\varphi_{r,i} + C_D \cdot \sin\varphi_i \tag{1.29}$$

10. Calculation local tangential force coefficient;

$$C_{t,i} = C_L \cdot \sin\varphi_i - C_D \cdot \cos\varphi_i \tag{1.30}$$

11. Calculation of local Prandtl's tip-hub loss correction factor;

$$F_{tip,i} = \frac{2}{\pi} \cdot \operatorname{acos}\left(e^{\left(\frac{-B\cdot[R-r_i]}{2\cdot r_i\cdot\sin\varphi_i}\right)}\right) \tag{1.31}$$

$$F_{hub,i} = \frac{2}{\pi} \cdot \operatorname{acos}\left(e^{\left(\frac{-B\cdot[r_i-R_{hub}]}{2\cdot r_i\cdot\sin\varphi_i}\right)}\right) \tag{1.32}$$

$$F_i = F_{tip,i} \cdot F_{hub,i} \tag{1.33}$$

Where r_{hub} is the distance betwen the rotor axis and the first blade-element root.

12. Calculation of local solidity factor;

$$\sigma_i = \frac{B \cdot c_i}{2 \cdot \pi \cdot r_i} \tag{1.34}$$

13. Calculation of local axial induction factor;

$$a_i = \frac{1}{1 + \frac{4 \cdot F_i \cdot \sin(\varphi_i)^2}{\sigma_i \cdot C_{n,i}}} \tag{1.35}$$

14. Recalculation of local thrust coefficient for a ≥ 0.4 up to 1 (or for $C_T \geq 0.96$);

$$C_{T,i} = \frac{8}{9} + \left(4 \cdot F - \frac{40}{9}\right) \cdot a + \left(\frac{50}{9} - 4 \cdot F\right) \cdot a^2 \tag{1.36}$$

15. Recalculation of the local axial induction factor;

$$a_i = \frac{18 \cdot F - 20 - 3\sqrt{C_{T,i}(50 - 36 \cdot F) + 12 \cdot F(3 \cdot F - 4)}}{36 \cdot F - 50} \tag{1.37}$$

16. Calculation of the local tangential induction factor;

$$a_i^{'} = \frac{1}{\frac{4 \cdot F_{tip,i} \cdot F_{hub,i} \cdot \sin(\varphi_i) \cdot \cos(\varphi_i)}{\sigma_i \cdot C_{t,i}} - 1} \tag{1.38}$$

17. Check for convergence;

$$|a_{new} - a_{old}| \leq 0.001 \tag{1.39}$$

$$|a'_{new} - a'_{old}| \leq 0.001 \tag{1.40}$$

If the convergence is achieved, calculate relative wind speed, otherwise repeat iteration steps from step 7 to 17 until the convergence is achieved;

18. Calculation of local relative wind speed;

$$V_{rel,i} = \sqrt{[(1 - a) \cdot V]^2 + [(1 + a') \cdot r_i \cdot \omega]^2} \text{ (m/s)} \tag{1.41}$$

19. Calculation of local chord Reynolds number;

$$Re_i = \frac{\rho \cdot c_i \cdot V_{rel,i}}{\mu} \tag{1.42}$$

20. Calculation of local axial force (thrust force);

$$F_{n,i} = \left(\frac{1}{2} \cdot \rho \cdot {V_{rel,i}}^2 \cdot c_i \cdot \Delta r\right) \cdot C_{n,i} \text{ (N)} \tag{1.43}$$

21. Calculation of local tangential force;

$$F_{t,i} = \left(\frac{1}{2} \cdot \rho \cdot {V_{rel,i}}^2 \cdot c_i \cdot \Delta r\right) \cdot C_{t,i} \text{ (N)} \quad (1.44)$$

22. Calculation of local torque;

$$Q_i = r_i \cdot F_{t,i} \text{ (Nm)} \quad (1.45)$$

23. Calculation of the power of the blade element;

$$P_i = \omega \cdot T_i \text{ (W)} \quad (1.46)$$

By considering the blade number B = 3, calculate overall axial and tangential forces, torque and power;

24. Calculation of total axial force (thrust force) on the rotor blades;

$$F_n = B \sum_{i=1}^{N} \left(F_{n,i}\right) \text{ (N)} \quad (1.47)$$

25. Calculation of total tangential force on the rotor blades;

$$F_t = B \sum_{i=1}^{N} \left(F_{t,i}\right) \text{ (N)} \quad (1.48)$$

26. Calculation of total torque of the rotor on the rotor blades;

$$Q_n = B \sum_{i=1}^{N} \left(Q_i\right) \text{ (N)} \quad (1.49)$$

27. Calculation of total power of the rotor;

$$P_n = B \sum_{i=1}^{N} (P_i) \ \text{(W)} \tag{1.50}$$

28. Estimation of the power coefficient of the rotor;

$$C_p = \frac{P_{out}}{\frac{1}{2} \cdot \rho \cdot A_R \cdot V^3} \tag{1.51}$$

1.4 Flow Control Techniques

During the initial phase of conceiving the plan to carry out the reasearch work, the idea of reaching the aerodynamic effect of a wind turbine blade prevailed through redesigning of its certain profile segments to ensure proper interaction with the flow field. However, it was decided to be more obvious to consider the approaches from different authors from the literature who successfully implemented passive flow control methods around airfoil under different Reynolds number regimes and certain operational conditions.

As this study is focused to develop a blade profile for small wind turbine blade applications, then their operation zone associates with small Reynolds numbers which, according to Giguère and Selig (1997), is considered to be when when $Re \leq 5 \cdot 10^5$. This flow regime, in which the viscous forces within the fluid are predominant over the inertial ones, especially for $Re \leq 2 \cdot 10^5$ according to the aforementioned authors, is sensitive enough as the drag force increases significantly whereas the lift drops essentially from the presence or bursting of the laminar separation bubbles formed on the upper surface of the airfoil as a result of the reattachment of the separated flow under certain flow conditions.

A typical example of formation of a laminar separation bubble from the leading edge to the upper surface of an airfoil at low Reynolds numbers is illustrated in Figure 1.15. As seen in figure, the flow approaching the nose of the airfoil forms a laminar boundary layer which can easily be affected by the change in pressure along the suction side and separate

from the surface leading to a turbulent flow state due to the formation of the separation bubble.

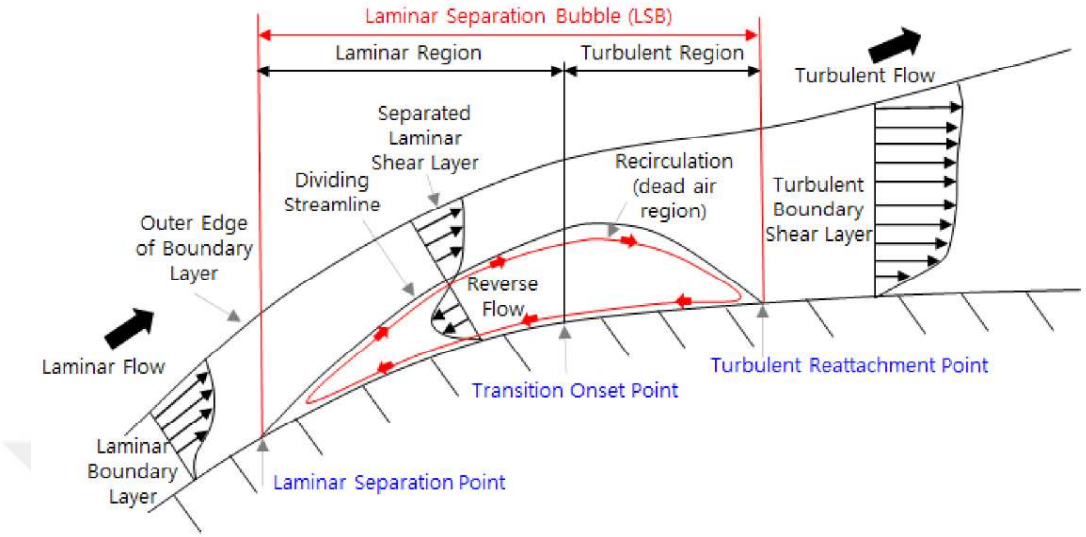

Figure 1.15. Laminar separation bubble formation (adapted from Mo and Rho, 2020)

Therefore, in such conditions of operation of small wind turbines, the prevention of negative effects from this flow phenomenon which affects the aerodynamic performance of the rotor blades is needed.

In fact, there are two main flow control techniques known as passive and active techniques that could be used to improve the flow field over a body to achieve an even higher level of performance of a rotor. In this context, by preventing the early flow separation and also stall phenomenon it is possible to increase the maximum lift coefficient, lift to drag ratio, and also to improve other aerodynamic and operational characteristics (Serdar Genç *et al.*, 2020; Wang and Feng, 2018; Pechlivanoglou, 2012; Rehman *et al.*, 2018).

In the frame of passive flow control methods, according to above mentioned authors, there are several techniques such as: vortex generators, gurney flaps, leading edge tubercles, stepped induced vortex (cavity), rib-lets, trailing edge serrations, slotted airfoils, flow vanes, roughness surface, et cetera, which can be applied on the rotor blades body by modifying the baseline geometry or by attaching devices along their surfaces. On the other hand, active techniques are a group of techniques that require additional

energy and systems to be put into operation. Several active flow control techniques are presented by Wang and Feng (2018), such as: plasma actuator, flow perturbation, jet, suction, oscillation, et cetera.

Since active flow control techniques are not in our scope of the study, therefore they will not be considered.

In the following, two passive flow control techniques will be presented.

1.4.1 Leading edge tubercles technique

Our world is surrounded by natural phenomena which can be useful even in the technologies that humanity makes to meet their needs more efficiently. A typical example is the aerodynamic shape of the whale's flippers that have some geometrical similarities with the wind turbine blades. As can be seen from the Figure 1.16, its tapered and twisted flippers are characterized by sinusoidal shape due to some bumps distributed along the leading edge.

Figure 1.16. The wavy shape of the humpback whale flippers (URL-1)

It is precisely the wavy shape of the flipper that enables the formation of vortices with opposite rotations along the troughs which affect flow separation delay by minimizing large separation bubbles and thus helping flow to rejoin at high angles of attack, and also improving the e post-stall characteristics under different flow conditions (Hansen *et al.,* 2011; Adachi *et al.*, 2016; Wang and Feng, 2018) (Figure 1.17).

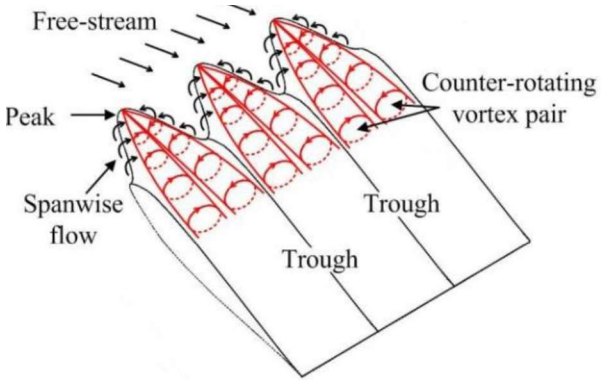

Figure 1.17. The wave shape airfoil characteristics (Wei *et al.*, 2015)

Regardless of the different mediums in which they work, the way in which the whale swims and performs spectacular maneuvers so efficiently underwater can be adopted as a useful mechanism for application in wind turbine blade technology (Hansen,) (Figure 1.18).

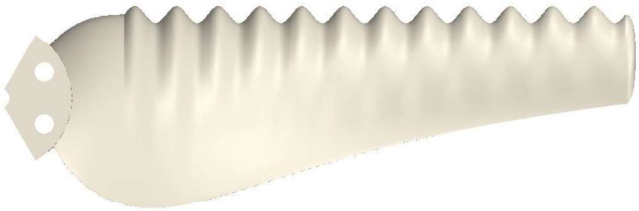

Figure 1.18. The leading edge tubercles technique modele implemented on the blade (present study)

The leading edge modification technique is a concept developed based on the example of humpback whale flippers. The wavy shape of the leading edge resembles the hump of whale's flippers which is characterized by amplitude and wavelength (Figure 1.19).

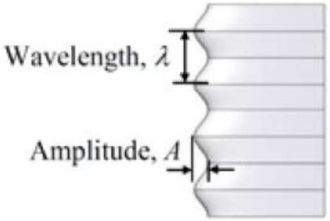

Figure 1.19. The wave shape airfoil characteristics (Hansen *et al.*, 2009)

The sinusoidal shape of the leading edge according to Hansen *et al.* (2009) can be described as:

$$y = \frac{A_m}{2} \cdot sin\left(\frac{2 \cdot \pi \cdot x}{\lambda_m}\right) \tag{1.52}$$

Where; A_m – amplitude of the wave, λ_m – wave length, x – coordinate of the first bump from the center of the rotor.

1.4.2 Vortex cavity – backward-facing step technique

An old method for controlling the vortex flow applied in aircraft and vehicles technologies with the aim of preventing the flow phenomena which lead to onset of flow separation or stalling at high angles of attack according to (IMechE, 2014; Olsman and Colonius, 2011), can be a reasonable solution even in wind turbine technology. Since the turbines have small dimensions but high solidity, they rotates fast and operate at low Reynolds number regimes which is characterized by flow instabilities which affect significantly the aerodynamic performace of the airfoil. Therefore, the addition of a cavity with the aim of generating a suitable (negative) pressure field to prevent flow separation at high angles of attack would be beneficial to wind turbine blade aerodynamics. This technique can applied on the suction side or the pressure side of the airfoil from root to tip of the blade by opening channels as shown in Figure 1.20 (Finaish and Witherspoon, 1998).

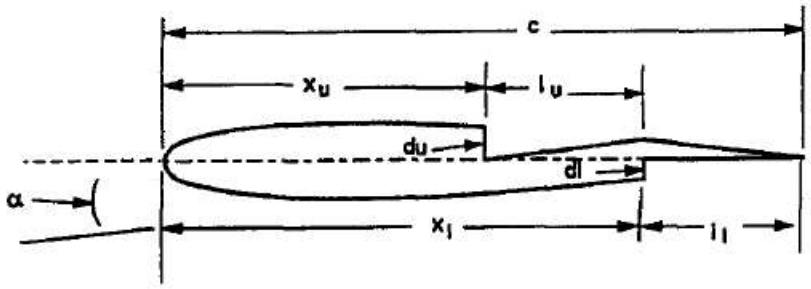

Figure 1.20. Backward-facing step airfoil geometric parameters: c - chord length, x_u - step location, d_u - step depth, and l_u - step length (Finaish and Witherspoon, 1998)

Also, authors just aforementioned argued that this method has been shown to be very effective in neutralizing large scale vortices thanks to its blocking mechanism which by interacting with the fluid flow creates suitable conditions to prevent flow separation or stalling phenomena.

Figure 1.21. The vortex cavity implemented on the upper surface of the blade (present study)

By applying this technique on the upper surface of the blade as depicted in Figure 1.21, the cavity is constructed according to Finaish and Witherspoon (1998) and Witherspoon and Finaish (1996) approaches and can be described as:

$$X_u = \%c, L_u = \%c, D_u = \%t \tag{1.53}$$

Where; X_u (mm) – step location from leading edge, $\%c$ – percentage of the chord length, L_u (mm) – length of the step, D_u – step depth, $\%t$ – percentage of the airfoil thickness at specific location.

CHAPTER II

LITERATURE REVIEW

2.1 Review of published studies relating to airfoil aerodynamics

Many authors are engaged in the studying of aerodynamic characteristics of airfoils, some of which are presented in the following;

Having to relate with the nature of operation of wind turbines, where the relative wind speed varies as per the rotor radius, then the geometric form of the rotor blades will change from hub to tip. As closer to the rotor centre, the blade dimensions or its sections usually become more and more large due to structural aspects but in the meantime, they shall also fulfil the aerodynamic criteria. In this context, the proper selection of geometric dimensions of blade sections, its shape, material, as well as the quality of the surface is essential for the normal and optimal functioning of such wind converting systems.

Giguère and Selig (1997) in their experimental work have made a database with aerodynamic characteristics of airfoils for application in the small wind turbines with a horizontal axis. In addition, some instructions are provided on how to select the appropriate profile of blades flow regimes. A year later (1998), the same authors published another science project where they designed and investigated experimentally the performance of couple of airfoils destined specifically for small wind turbines, which operate in a variable speed, and in low Reynolds numbers flow regime. Singh *et al.* (2012) on the other hand in their study have modelled a profile of airfoils destined exclusively for small wind turbines with special emphasis on the functioning with small wind speeds and to solve the self-initiating problem. The model is investigated also experimentally in the wind tunnel for several Reynolds numbers. Shah *et al.* (2012) presented a method to design airfoils for application on small turbines with a horizontal axis. The authors used one of two methods to design the airfoils, the direct design method and reached high values of aerodynamic efficiency per low Reynolds numbers values. Wata *et al.*, (2011) in their study developed a new design for an airfoil for application on small turbines for which after testing in the wind tunnel, the result was better performance for various numbers of Low Reynolds and for various angles of attack. Fuglsang and Bak (2004)

have developed several families of airfoils from the RISØ family (Danish Technical University) for application in wind turbines for different power capacities and other specifications of wind turbines. The authors Akour *et al.*, (2018) in their work have designed a type of small wind turbine for application mainly in one part of the middle east region for specific wind speed. Blade element momentum theory was used as a method for optimism construction of profile blade geometry. The study was accomplished as theoretically and also experimentally which resulted a more effective product. Various valuable instructions related to airfoils aerodynamic specifically for application on wind turbines, their selection as well as for their characteristics depending on flow field regime where they operate are provided by authors Timmer and Bak (2013). Eppler (1990) on the other hand in his work presented a volume with aerodynamic airfoils data for various applications and for various regime flows. Timmer and Van Rooij (2003) have summarized and analysed experimentally the aerodynamic performance of some types of dedicated airfoils for wind turbines from DU Family (Delf University). Bjorck (1990) on the other hand in his review has designed and tested in the wind tunnel several families of airfoils (FFA Airfoils) for specific applications in horizontal axis wind turbines. Abbott and Von Doenhoff (1959) in their book have summarized a wealth of data on the geometric characteristics of profiles and their results from experimental tests of NACA family airfoils which are best known for application mainly in aviation.

Mathew and Geeta Susan (2011) in their book have also addressed the issue of self-starting in horizontally axis small wind machines and the importance of blade geometry in this issue and have suggested that in the rotor hub area depending on whether the blade pitch is controlled or not (fixed) to select sections with maximum or minimum values of the maximum lift coefficient. Katz (1995) in his book has reflected the importance of geometrical characteristics of airfoils and their specific role in improving aerodynamic performance by increasing the quality of the flow field around its body. The author highlights the aerodynamic benefits which can be achieved by manipulating geometric parameters such as camber, thickness, leading edge radius, and trailing edge. Philip Barnes (1996) has presented in his work couple of methods for the geometrical description of airfoils geometry through mathematical equations and has suggested new profiles for application in aeronautics. Tangler and Somers (1995) in their work have designed various profiles of blades of the NREL Airfoils Family specifically for small wind turbines with various thicknesses and for a certain radial position across the blade

span. Bertagnolio and Sorensen (2001) in their work have applied the code EllipSys2D on validating results of couple of airfoils destined for wind turbines acquired by Xfoil code and experimental testing. Selig and Guglielmot (1997) have developed a new approach to design airfoils for high lift which resulted better for a certain number of Reynolds. Also, the authors have experimented with two passive techniques with very much success by impacting further increase of the maximum profile lift. Lissaman (1983) also analyzed the importance of airfoil selection depending on the size of the facility and its area of operation in flow regimes. In addition, the author describes flow phenomena faced by objects in motion in fluid especially when dealing with low Reynolds numbers.

A study done by Winslow *et al.* (2018) regarding the effects of section geometry features for low Reynolds numbers has shed light on the dependence of aerodynamic coefficients especially in this area where flow is characterized by increased impact of viscous forces. Liebeck (1990) in his work has presented two main methods which are used to design airfoil profiles: the direct method which consists in modifying a known geometry until the desired solution is achieved and the method indirect which starts from the 'opposite' side of the problem by manipulating the flow velocity of the fluid along the contour of the profile to achieve the appropriate change in pressure propagation that as a result would give the desired performance. Also, the author gives explanations for the flow phenomena which are usually encountered in subsonic flow regimes. Anderson (2011) in his book among other has analysed the role of Reynolds number and its effects in the aerodynamic performance of immersed in fluid (air) objects. In this sense, the aerodynamic coefficients of airfoils mainly depend from Reynolds number and also from Mach number and angle of incidence. Furthermore, the author has presented a graph with experimental data which reflects the drag effect decrease of circular cylinder with Reynolds number increase and vice versa.

According to Bertin and Cummings (2013), the aerodynamic characteristics of airfoils depend on several parameters such as its geometric shape, its dimensions, angle of incidence, wind quality, surface roughness, surface temperature, Reynolds number, and Mach number. The author has also analyzed the effects of geometric parameters of airfoils such as the effects of leading edge shape, camber to chord ratio, thickness to chord ratio, and trailing edge angle in the subsonic flow regime. In addition, it is emphasized that the sections which operate in this flow mode are arched with radius up to one percent of the

chord length due to their role in preventing flow instabilities, have curved shapes to provide lift force even for very small angles of attack, also affecting the increase of the maximum lift coefficient. According to the author, the velocity of air flow along the surface of the profile can be changed by changing the length of the contour of the section which increases with increasing its thickness. Meanwhile, depending on the distribution of thickness in chord wise direction it can be predicted from which side the stall phenomenon may begin to appear initially. The author has also addressed the role of surface quality and temperature as important contributors to the prevention of flow transition. On the other hand, Gudmundsson (2013) in his book, among others, has treated and reflected details of the methods for designing airfoils, the behavior of each of the characteristics of the geometry of airfoils in relation to flow regimes and has also described the positive effect of surface roughness in preventing flow separation especially for low Reynolds number regime. Miley (1982) in his catalogue of air foils has presented data regarding the airfoils for using in wind turbines which operate in Low Reynolds numbers. The author has dealt in detail the geometrical characteristics of a cross section of the blades, aerodynamic forces which characterize them, flow field behaviour, their experimental investigation manner as well a database with specific air foils.

According to Burton *et al.*, (2011) wind turbines are mainly designed to operate in conditions of incompressible flow (Mach number < 0.3), but when dealing with small turbines care must be taken as their speed type blades rotate much faster to hold the system within optimal efficiency values and can change the nature of the flow. In this sense, working at high blade operating speeds in viscous flow areas requires a more specific profile with less thickness, insensitive to roughness, certain camber distribution, appropriate leading edge radius and trailing edge angle. Also, this phenomenon is manifested by noise emission when the maximum speed of the blade's tip exceeds the limit of 70 m/s (Wood, 2011). Meanwhile, the operation of wind machines at low or high atmospheric temperatures can negatively affect the physical properties of the blades by deforming them (Al-Bahadly, 2011). Rosato (2018) in his book has presented a table of preferred profiles of various families of sections tailored for using in small wind machines. It also gives suggestions on how to select the right rotor blades for certain operations conditions. Meanwhile, the author points out fixed pitch rotors are more common in small wind turbines. Osei *et al.* (2020), in their research article they have developed some air foils with small thickness for specific use in small wind turbines. The

authors used the Xfoil and Blade Element Momentum Method program to design and analyse the aerodynamic specifications of profiles and reached optimal results in the aerodynamic rotor performance.

2.2 Review of published studies relating to passive flow control techniques

Several authors addresses the effects of passive flow control techniques and some of them are presented below;

Fertis (1994) investigated new airfoil design concept using vortex cavity on the suction side of NACA 23012 section experimentally for several of angles of attack and wind speeds to obtain better results regarding to aerodynamic coefficients. Different step distributions were examined to define their aerodynamic effects. According to the results, the new section shape concept has gained advanced stall properties and enhanced aerodynamics characteristics. Finaish and Witherspoon (1998) investigated the flow around the NACA 0012 profile with the use of the passive flow devices. They examined different step distributions to define their aerodynamic effects. Results suggests that enhanced lift values were gained when the step expanded from 50% to 75% of the chord length rather than from 50% of the chord length to the trailing edge for incidence angles under 20^0. For about 20^0 to 30^0 the greater benefits in lift coefficients came from a step expanded from 50% of the chord length to the trailing edge. The author, also, suggests that inclusion of cavity on the pressure side 50% of the chord length up to the trailing edge with 50% depth may conduct to considerable improvements in aerodynamic characteristics. At incidence angle of around 10^0 the suction side step with 50%c, 12.5%c, and 19%t provided higher L/D ratio than clean shape. Boroomand and Hosseinverdi (2009) investigated numerically a stepped airfoil (NACA 2412) at Re = $5.7 \cdot 10^6$ to investigate its aerodynamic behavior. Steps were positioned on both airfoil sides at various locations. Based on the results, all the studied cases eperienced higher drag compared to baseline model section. They suggest that the cavity on the pressure side that extended back to section edge can provide more improvement of aerodynamic characteristics for several incidence angles, while the rear cavity positions on the suction side was not found to have aerodynamic benefits. Gregorio and Fraioli (2008) investigate experimentally the effects of the vortex cavity technique on a thicked airfoil in the wind

tunnel at angles of attack between 5.66º to 12.66º and at free stream of 15 m/s to 30 m/s. For the conditions set, this technique has not shown effectiveness in controlling the flow separation.

Donelli *et al.* (2010) studied the effects of trapped vortex cavity as passive and active flow (steady suction inside the cavity) control technique in controlling the flow separation. They mentioned that when the facility has to operate at high wind velocities such as aircrafts, the thickness of their wings plays a crucial role. Therefore, for such conditions streamlined and thin wings are the key to success. However, the need for larger flying machines raised the interest to researchers to improve the aerodynamics of thick wings because of the poor aerodynamic efficiency they possess at high Reynolds numbers. For this reason, the authors appeared interest to study the effects of passive flow control means on thick profiles to improve their aerodynamic characteristics for such flow confitions. After comparing the results obtained, they observed that steady suction inside the cavity is more efficient than without it.

Shi *et al.* (2014) studied experimentally the effects of the vortex cavity technique on NACA 0020 airfoil at several incidence angle from 0º to 20º and at Reynolds number of 5000. They found that this technique has not proved effective in preventing early flow separation compared to the unmodified model. Olsman and Colonius (2011) presented a study of the effects of the vortex cavity added over the suction side of the NACA 0018 using 2D Direct Numerical Simulation. They found that at chord Reynolds number of $2 \cdot 10^4$ and at high positive incidence angles this technique showed good interaction with the flow separation thus neutralizing it better than the clean model. Iollo and Zannetti (2000) studied the effects of the vortex cavity method with the aim of increasing the aerodynamic behaviors of Joukowski section. Witherspoon and Finaish (1996) investigated the effects of the vortex cavity on both section sides of NACA 0012 profile at several incidence angles from 0º to 20º and at Reynolds number of $1.6 \cdot 10^5$, and $5 \cdot 10^5$ respectively. They analysed several configurations by changing the step length from 12.5%c to 50%c, step depth from 19%t to 50%t whereas the step location is kept fixed from leading edge at distance 50%c. Based on the computational and experimental results, they found that this technique has shown good effectiveness for certain configurations and cases. They also observed that the drag was proportional to the step depth.

Hansen *et al.* (2011), investigated experimentally the effects of modification to the leading edge geometry of NACA 65-021 and NACA 0021 airfoils by adding rounded tubercles. From the results, they concluded that both modified and cleaned sections are more useful for NACA 65-021 than NACA 0021. Also, the reshaped NACA 65-021 section outperforms cleaned model for majority incidence angles for smaller values of amplitude. Abate *et al.* (2019), investigates the effect of different tubercle cases: λ_m = 0.016 to 0.075 and A_m = 0.01 to 0.05, at four free stream speed conditions: 5, 10, 15 and 20 m/s. They manipulated with amplitude and wavelength values then imitated virtually through a CFD program. Based on the results, they noticed a benefitial effect of tubercless at free stream speed of 20 m/s but the effect is inconsiderable for all variants at free stream speed of 5 m/s. Improvement can be noticed at the models with high amplitude and low wavelength values. Ng *et al.* (2017) investigated the role of tubercles on turbine performance. They accommodated tubercles in different places and as a consequence they achieved lower aerodynamic characteristics. In terms of tubercle locations, closer to the blade's tip and root region yields improvement performance regarding stall conditions. Also, from the experiments they revealed that the effect of small wavelength is more beneficial for low free stream speeds whereas high wavelength is more suitable for high free stream speeds. Ni *et al.*, (2018), have investigated virtually through CFD the efficiency of a proposed wavyshaped twisted model at Reynolds number of $1.2 \cdot 10^5$. They suggest that this technique has benefit on flow control on stall behavior especially at high angles of attack. Leading edge tubercles with large amplitude has shown good results on stall and post stall behavior.

Lohry *et al.*, (2012), have studied virtually leading edge tubercles technology added to NACA0020 airfoil at several incidence angles and various Reynolds numbers between $6.25 \cdot 10^4$ to $5 \cdot 10^5$. They observed that this technology is beneficial for specific span locations, but not for low Reynolds numbers flow regimes. Wei *et al.* (2015), have studied experimentally the effects of tubercles on hydrofoils at Re = $1.4 \cdot 10^4$. They observed that in this flow regime larger amplitude and smaller wavelength were beneficial in control of flow separation. Bolzon *et al.* (2014), studied the effects of tubercles technique on an aircraft's wing at low angle of incidence 1º to 8º and at Re = $2.2 \cdot 10^5$. They found that this passive mechanism reduced the aerodynamics coefficients but increased the lift to drag ratio. Bolzon *et al.* (2016), in their work have studied the tubercles technique and their applications on various types of foil's leading edge. They showed that this technology

has shown many benefitions in the sense of aerodynamic performance of foils; improve pre and post stall behavior as well as the maximum lift coefficient. This can be useful in wind turbines blades of which are twisted at high angles of incidence and also might reduce the noise created at the tip of the blades.

Watts and Fish (2001), in their numerical research work have presented the leading edge tubercles technique advantages versus the model without it at a angle of incidence of 10º. They demonstrated that this technique may be useful adaptation given the fact that whales have extraordinary maneuverability thanks to this natural gift possessed by their humpback flippers which provide lift while reduce the drag.

Aftab and Ahmad (2017), investigated through CFD and in a wind tunnel the effects of leading edge sinusoidal and spherical forms at Re = $1.2 \cdot 10^5$. NACA 4415 airfoil was selected to perform this study. They implemented several configurations by taking three different amplitudes 2.5%c, 5%c, and 7.5%c, while keeping constant wavelength at 25%c. They observed that for the two cases the smaller the amplitude the better the results. Pechlivanoglou (2012) and Wang and Feng (2018) provided useful information about the passive and active flow control techniques.

2.3 Review of published studies relating to aerodynamics of wind turbines

In the following, scientific works by various authors who have dealt with the design and analysis of aerodynamic performance of turbine rotors under different operating conditions are presented;

Burton *et al.* (2011); Manwell *et al.* (2010); Gasch and Twele (2012); Hau (2013); Hansen (2015); Letcher (2017); Mathew and Geeta Susan (2011); Wood (2011); Gipe (2004); Jamieson (2011); Jain (2010); Corke (2018); Branlard (2017); Kishore *et al.* (2018); Spera (2009); Nelson (2013); Jha (2010); Wizelius (2015); Le Gourieres (2014); Rosato (2018); Schaffarczyk (2014); Rao (2019); Twidell and Weir (2006); Van Treuren (2016) in their scientific works have provided abundant information in terms of wind energy and wind turbine technology covering significantly various aspescts relating to aerodynamic design of wind turbine rotors.

Schubel and Crossley, (2014) in their work have elaborated the principles of wind turbine blade design and also the advantages of modern over 'traditional' wind machines. Also, the authors dealt with structural analysis of wind turbines blades. Ragheb and M. (2011) presented the Betz criterion for wind machines and the laws deriving from this approach for determining their optimal design parameters. They decomposed in details the concept of Betz's law and yield the equations from this theory for ideal conditions. Ingram (2011) presented the Blade Element Momentum Method for designing and analysing rotor aerodynamic performance. Bakırcı and Yılmaz (2018) investigated the speed ratio parameter of turbine using the Blade Elemenet Momentum Theory and a CFD code to evaluate its efficiency and optimal tip speed ratio for different types of airfoil profiles. They found that power coefficient calculated using CFD code was lower compared to BEM method. Dehouck *et al.* (2018) applied Blade Element Momentum Theory to design and optimize the small rotor's blade geometry. In this case, turbine diameter, number of blades, curvature, speed ratio, and free stream speed were taken as initial design parameters. Also, a detailed explanation of implementation of the design and optimization process is presented. Kulunk and Yilmaz (2009) presented an approach based on BEMT to design and optimize a 100 kW wind turbines blade's geometry. Liu and Janajreh (2012) used an improved BEMT code by including corrections such as tip loss, et cetera. They compared the results obtained form the code with those from the NREL measured data of the two bladed wind turbine which revealed improvements.

Khaled et al. (2017) applied Blade Element Momentum code written in Fortran program and a CFD code to design and optimize the small horizontal axis wind rotor blades at several pitch angles. This approach consists of optimizing chord and twist magnitudes along the blade span. They found that blade angle is in proportional relationship to the power generated and wind speed. Chaudhary and Roy (2015) utilized BEM method to design and optimize the aerodynamics of a 2 meters rotor's diameter with a capacity of 400 W. They used SG 6043 airfoil type to analyse the design parameters such as maximum power coefficient, tip speed ratio, twist angle, chord length, solidity from 2% to 30%, and for number of blades 3, 5, 7, 12, and 15. Results drawn by Matlab and QBlade codes revealed that power coefficient reaches highest values for solidity between 2% to 12% as the number of blades ranges from 3 to 7.

Muhsen *et al.* (2019) conducted a study on small turbine blades with the aim of increasing the efficiency at low free stream speed. BEM, QBlade, and Matlab were employed in the process of designing and optimization of the blade's geometry. S1210 and S1223 section types were used in the optimization process to obtain the final section profile. Their results indicated an improvement of power coefficient by 0.445 at free stream speed of 5.5 m/s and $\lambda = 6.5$ producing 650 W while at a free stream speed of 7 m/s turbine is capable of producing 1.18 kW of power which correspond to power coefficient of 0.40.

Tahir *et al.* (2019) used the BEMT and Viterna-Corrigan model included along with a Matlab/Simulink tool in the design and optimization process to maximize the rotor efficiency. NACA 0012, NACA 0018, S809, and NACA 63-412 were employed in this process to optimize their geometric parameters in terms of chord and twist deployment. The optimization data obtained through BEM theory were used to exhibit torque in the genereator shaft of the wind turbine. They found that the optimized model showed better performance compared to an existing unoptimized wind turbine blades' system. Karthikeyan and Suthakar (2016) in their study performed geometry optimization on several airfoils using BEMT and Matlab tool for small turbine applications. MID321a, MID321d, SG6040, SG6041, SG6042, and SG6043 airfoil types were employed in the optimization process where the free stream speed of 3 to 14 m/s, Reynolds numbers between $5 \cdot 10^4$ to $2 \cdot 10^5$, chord length between 0.25 m to 0.35 m, fluid kinematic viscosity of $16.5 \cdot 10^{-6}$ m^2/s, were taken as input parameters. From the optimization results they founded that MID321a and MID321d airfoil types showed better aerodynamic performance compared to others. The rotor blade's geometry constructed using MID321a airfoil type selected for Reynolds number of $8 \cdot 10^4$ reached a power coefficient of 0.40.

Wang *et al.* (2012) presented a practical approach of designing an optimal fixed-pitch and fixed-flow-speed for small rotor's blades. The authors used aerodynamic characteristics of airfoil's, annual mean wind speed, and tip speed ratio as the design parameters. Several different design cases that generated were are compared to verify which design yielded maximum performance. Pierce and Migliore (2000) investigated experimentally a fixed-pitch stall-regulated variable-flow-speed turbine. The test results obtained for wind turbine operated at variable free stream speed and variable rotational speed were compared with the tests results obtained for fixed-speed. Based on results obtained, active control method for regulating the rotor speed demonstrated excellent capability in

tracking the optimum tip speed ratio for peak power coefficient. However, for variable speed operation at maximum power coefficient the tower fatigue loading were increased compared to the constant speed operation wind turbine. Hsiao *et al.* (2013) studied numerically using BEMT and experimentally small turbine blade's shapes using NACA4418 at free stream speed of 10 m/s, $\lambda = 5$, and Reynolds number of $1 \cdot 10^5$. Three blade design scenarios were generated with the same airfoil. One is an optimum blade shape; unlike the first model the second is un-tapered and optimal twist with constant chord lengths along the blade span, while the third model is un-tapered and un-twisted blade model. They observed that the first model reached power coefficient of 0.428 at tip speed ratio of 4.92, interestingly however the second case reached a power coefficient of 0.428 at tip speed ratio of 4.32. Meanwhile, the last model reached the maximum power coefficient of 0.210 at tip speed ratio of 3.86. Hirahara *et al.* (2005) have developed a very small four bladed wind turbine with a rotor diameter of 0.5 m and high solidity of 0.36. NACA 2404 airfoil type were used to build the blade shape. They took care of noise emission so that they limited the tip speed ratio from 2 to 4 in contrast to unusual turbine ranging from 8 to 10. The authors justify the advantages of a small sized wind turbine model for the fact that the shorter dhe blade length the smaller bending and tensile stresses. Due to the size of the model, they used an untapered fan type blade model to enhance the power coefficient for lower rotational speed. Experimentals results revealed that this configuration showed good aerodynamic performance in the wind speeds between 8 to 10 m/s reaching a power coefficient of 0.36. On the other hand, the maximum power coefficient of 0.40 is obtained at tip speed ratio of 2.7. Kishore *et al.* (2013) designed and tested experimentally in the wind tunnel a small wind turbine aimed to work at free stream speed under 5 m/s. Based on the experimental data, they found that maximum power coefficient of 0.14 is achieved at $\lambda = 2.9$ producing mechanical power of 1.25 Watts and 0.83 Watts electrical power. To enhance the efficiency they added a difusser structure around its diameter. They found that with the help of this structure added, the wind turbine were able to yield 140% to 160% times higher power.

Duquette *et al.* (2003) studied the influence of solidity and number of blades on a fixed-pitch wind machine named Rutland 500. After comparing the wind tunnel data with theoretical ones they concluded that with the increase of these two design parameters the generator would produce higher power coefficient. Also, it is observed that the optimum tip speed ratio is inversely proportional to pitch angle significantly at higher angle values.

In the case of constant solidity of 10% while changing the blade number from 3 to 12, they found poorer outcomes.

Kumar Gupta *et al.* (2017) presented a procedure to design and optimization small size wind machines consisted of mixed airfoils along the blade length. Initially, two rotors were developed comprised of different airfoils types but from the same family. The wind machines were analysed for free stream speeds between 4 to 7 m/s, at different tip speed ratios, and at Reynolds number of $1 \cdot 10^5$. Airfoil types such as SG6050, SG6043, E555, and E216 were selected to build the blade structure. BEMT is employed for aerodynamic design and analysis of the wind rotor, while validation is done using Ansys software. They came into conclusion that the rotor blades composed of SG6050 and SG6043 found to be more suitable combination for the given design conditions. The maximum theoretical torque values derived from the BEM was 7.52003 Nm and power coefficient of 0.445 at tip speed ratio of 7 and wind speed of 6 m/s, whereas from CFD analysis for the same conditions the torque was 6.028 Nm and power coefficient 0.35687.

Maalawi and Badr (2003) presented a method for choosing the design parameters of a wind turbine for optimum operational condition through examples. They singled out six parameters such as chord and twist layouts, number of blades, blade section profile, hub radius, and tip speed ratio as the key design parameters. Also, this approach takes into consideration both wind shear and tower shadow. Clausen and Wood (1999) highlight issues for small wind machines whose power limit is taken as 50 kW. In their study, they consider major issues of rotor's blades aerodynamics, its starting behavior, materials, and production methods. They mentioned that the major problem for micro turbines and mid-range is their starting torque while for mini turbines much less. Also, they described the small dependence of the chord Reynolds number on rotor radius at especially during starting.

2.4 Review of published studies relating to wind tunnel testing

Numerous authors have studied and analyzed the influence of the wind tunnel on the quality of the experimental results by proposing wind tunnel calibration techniques, model preparation for testing, force measuring techniques, scaling laws, and data correction methods. Some of them are presented below;

Barlow et al. (1999); Fischer (2018); Tropea *et al.* (2007); Discetti and Ianiro (2017); in their scientific works have provided abundant information in terms of wind tunnel testing and experimental facilities. Van Treuren (2015) in his work provided valuable information regarding wind tunnel testing of small scale wind turbines under low Reynolds number conditions. The author addresses the importance of tunnel testing of airfoils and wind turbines as a whole as well as the steps that need to be taken to ensure the quality of the experimental work. As it is impossible to provide specific space and test facility for all kinds of airfoils and wind turbines, then various mathematical models have been developed to ensure acceptable geometric, kinematic, and dynamic scaling similarities suitable for tunnel testing associated with the data correction methods. The author emphasizes the necessity of Reynolds number matching in the wind tunnel especially when this value is below $5 \cdot 10^5$. While, if the frontal area of a model occupies less than 10% of the cross-sectional area of the test section, it is considered a low level of blockage and the corrections are not necessarily applicable. The author included correction methods for both airfoil and wind turbine tunnel testing. Meanwhile, if a wind turbine will operate below low Reynolds number conditions below $1 \cdot 10^5$, the author suggests considering active or passive flow control technologies.

Manwell *et al.* (2010) in his book gave some scaling relations mainly for changing the geometric size of wind turbines without Reynolds number matching due to some assumptions. Considering unchanged tip speed ratio, blade section profile, number of blades, material constant, and maintaining geometric similarity. Gasch and Twele (2012) in his book included mathematical scaling models for horizontal axis wind turbines and they suggest considering when the Reynolds number is below $2 \cdot 10^5$. Brusca *et al.* (2014) in their jounal paper applied the flow similitude laws coupled with the BEMT code to analyse the performance of various wind turbines. Burdet and Treuren (2012) in their study discussed the influence of aerodynamic coefficients, tip speed ratio, and Reynolds number for turbine size scaling. Authors, presented similarity laws showing us the necessity of Reynolds number matching when scaling a wind machine for tunnel testing. Gao and Hu (2009) investigated numerically the impact of Reynolds number on the performance of a scaled down model wind machine with the aid of the software FLUENT. Also, they suggest an average Reynolds number relationship to predict the appropriate Reynolds number corresponding to the maximum power coefficient at different rotational speeds.

Ananda *et al.* (2017) in their work discussed the development of a wind tunnel test capabilities to provide aerodynamic performance of a coned scaled rotor. They had many challenges with testing of small scales numbers because of the force generated, Reynolds number, and high rotational rates. The results obtained from testing emphasize the fact that Reynolds number effect is the main issue with testing scaled blade. Especially, at low Reynolds numbers below $5 \cdot 10^5$, where viscous effects related to the laminar separation bubble begin to influence the performance of the blade itself.

Qu *et al.* (2009) studied the influence of Reynolds number on the performance of a blade section profile. They concluded that while the Reynolds number varies from $1.5 \cdot 10^4$ to $2 \cdot 10^5$, both the drag and lift coefficients have great changes. But, when Reynolds number varies from $2 \cdot 10^5$ to $5 \cdot 10^6$, both the drag and lift coefficients have small changes and become smoother. Katz (2016) in his book among others, described the effects of the solid surfaces around a model that can change the flow field. The author highlights that if an object is placed within two walls, the streamlines are influenced by the walls and that will cause the flow to move faster in the gap. He cited some authors regarding solid blockage correction usage when the ratio between the frontal areal of model test and wind tunnel test section exceeds 7.5% and 10%.

Kang *et al.* (2013) proposed a new blockage correction approach for flows around 2D blade's section profile for closed test section tunnel type. After they performed testing at incidence angles ranges from 0 to 180 degrees at flow velocity of 15 m/s ($Re = 2.3 \cdot 10^5$), a correction for separated flows was provided. Although for small turbine designs the classical method is not difficult to implement at moderate incidence angles and the correction is not needed as well. However, when the flow gets separated from the body's surface, the correction is a necessity based on empirical relationships according to the experimental outcome of bluff bodies. They made this technique will stay away from exactly of the restrictions of the traditional system through measurement of the pressure along the test area limit on make those fundamendal revision. Thus, it can be implement to any model configuration but is more costly due to the cost of the equipment as well as other accompanying specifications.

Intaratep *et al.* (2019) investigated the aerodynamics of wind turbine blades for extreme events. The tests were made on airfoils with chord lengths of 46 cm, 80 cm, and 90 cm in

360 degree in a wind tunnel with nozzle exit 1.85 m x 1.85 m at Reynolds numbers of $1.5 \cdot 10^6$. It was found that the blockage effects generated by these 3 models are not symmetric with respect to ±90 degrees. The differences in the lift and drag in this range of incidence angles highlight the impact of the asymmetry on the blockage effects. They used most common method based on Maskell's work (1963) which utilized the frontal area of the model without the asymmetry of its mounting with respect to the wind tunnel centerline. Moreover, they regenerated a Maskell's version to account for the aerodynamic asymmetries up to 360°. This new approach was found to yeild corrected data in a good agreement for all design models. Selig *et al.* (2011) pesented the main tunnel corrections for lateral boundaries in 2D testing context such as: longitudinal buoyancy, solid and wake blockage, and streamline curvature.

Mueller and Jansen (1982) investigated the wind tunnel techniques developed for high Reynolds numbers but utilized to measurement of aerodynamic force coefficients of sections at low Reynolds numbers. The experiments were conducted for NACA 66_3018 and EPPLER 61 airfoils at Reynolds numbers between $4 \cdot 10^4$ to $4 \cdot 10^5$. According to the authors, many significant aerodynamic problems appear to occur under chord Reynolds number $2 \cdot 10^5$, where the low Reynolds regime is considered the zone under $5 \cdot 10^5$. They included techniques developed for high Reynolds number testing for measuring the force coefficients of sections at low Reynolds numbers. Also, an important attention they paid for the interference effects between two dimensional sections and side plates (0.51 mm) in this experimental test and reduced the minimum drag coefficient by 16%.

Pelletier and Mueller (2001) investigated the endplates on two dimensional airfoil testing at low Reynolds number wind tunnel. They found that endplates are responsible for the low performance of sections. The lift and drag force coefficients were affected due to the interaction of the airfoil boundary layer with the side plate boundary layer. They suggest some other authors work regarding the size between the airfoil and the endplates. According to them, the gap size in the range between 0.1 and 1.4 mm is considered as an acceptable limit. Also, a relation 0.005 · wing span is suggested. Vaidyanathan *et al.* (2014) investigated the influence of the gap between side plates and wing section on aerodynamic forces. The aim of the study was to determine the appropriate gap size at which flow can still be considered two dimensional, and the tip effects might be neglected. The NACA 0012 wind section with endplates was used in the experiment. A

nondimensional distance is defined as the ratio of gap size to laminar boundary layer thickness over the endplate. The value of this distance varied for desired values of 0.5, 0.75, 1.0, 2.0, 3.0 4.0 and data is taken at two different Reynolds numbers, Re = $5 \cdot 10^4$ and $1 \cdot 10^5$ for angles of attack of -10 to +10 degrees. It is found that for Re = $5 \cdot 10^4$ the critical gap size is in the range of 1.0±0.1 for a given section. The wing placed at a distance beyond this critical value produces higher drag and does not experience 2D flow.

CHAPTER III

SCOPE OF THE STUDY

The objective of this thesis is to develop a new wind turbine blade profile using two passive flow control methods on an existing airfoil type capable of operating more efficiently under low Reynolds number regime and off-design conditions.

The blade development process is devided into two stages. The first stage begins with the selection of the best airfoil profile among four models to be tested in the wind tunnel under two Reynolds numbers: $5 \cdot 10^4$ and $1 \cdot 10^5$ respectively. The airfoil which performs best in this stage will be subject to the geometry modification procedure in order to improve the aerodynamic behavior of the blade profile and consequently the rotor in general.

Meanwhile, in the next stage, eleven homogeneous blade structure with 0.14 m in length using the selected airfoil will be generated with acceptable solidity. The idea is to develop a wind turbine rotor blade model that will operate efficiently under low Reynolds number regime and off-design conditions.

The wind turbine rotors will be tested in an open-circuit wind tunnel with closed test-section. By adopting the two passive flow control techniques ten different rotor configurations will be generated by manipulating the design parameters based on the literature and will be manufactured using a 3D printer. Using leading edge tubercles technique, five configurations will be generated by changing the amplitude and wave length, meanwhile, four other configurations using the vortex cavity will be generated by changing the cavity location, its size and depth. Also, one model will be generated by combining the two techniques with parameters that have shown beter results for certain conditions based on literature.

The experimental results obtained will be analyzed and compared with each other to investigate their aerodynamic performance.

With this approach, it is intended to develop e new blade profile design which will provide high efficiency, good starting behavior characteristics, smooth operation, and also to operate under off-design conditions.

Thesis outline

This thesis consists of seven chapters as follow;

Chapter 1: Introduction
This chapter describes the mathematical formulations used to analyze and evaluate aerodynamic parameters of airfoils and wind turbines, to implement passive flow control methods on the wind turbine rotor blades as well as to estimate available power potention in the wind. This chapter continues describing the classification of wind turbines and their advantages.

Chapter 2: Literature review
In this chapter a literature review of several research works from many authors has been conducted on the aerodynamic characteristics of airfoils, passive flow control techniques, design and analysis of aerodynamic performance of wind turbine rotors, and on the effects of wind tunnel on the quality of the experimental results.

Chapter 3: Scope of the study
In this chapter the scope of the study and the thesis structure are introduced.

Chapter 4: Methodology and experimental setup
This chapter describes in detail the methodology and facilities empoyed to realize the objectives of the thesis.

Chapter 5: Experimental results for airfoil testing and comments
In this chapter the wind tunnel experimental results of all selected airfoil models were introduced. In addition, comments and comparative analysis of the airfoil models in terms of advantages and disadvantages were made.

Chapter 6: Experimental results for wind turbine testing and comments

In this chapter the wind tunnel experimental results of wind turbine rotors were introduced. This chaper includes comments and comparative analysis of the wind turbine rotor configurations regarding their efficiencies and advantages between them.

Chapter 7: Conclusions

In this chapter the conclusions were summarized.

CHAPTER IV

METHODOLOGY AND EXPERIMENTAL SETUP

This section describes all steps taken to carry out this experimental study in the wind tunnel. Data collecting and recording from the experimental measurements that was done through various devices are presented in this section.

Initially, this research work started with the selection of airfoil models from two well-known families of airfoils (NREL and NACA). The selected models are produced in 3D printer with from ABS material and then they are processed and dyed to get a smoother surface. Two circular plates were attached on both sides of the airfoil edges to eliminate the 3D efects of the free stream. The profiles were tested in the wind tunnel for aerodynamic performance for two different Reynolds number regimes $5 \cdot 10^4$ and $1 \cdot 10^5$. The model with the best performance shown for the given conditions is used as the basic geometry to then generate different configurations of the rotor blades by applying passive flow control methods.

The geometric shape of the blades is calculated based on the mathematical models presented by Schmitz for certain operating conditions and low Reynolds number regime, whereas three-dimensional geometry of the blade is constructed with the help of a CAD software. By applying passive flow control techniques to profile geometry, several configurations are generated by manipulating its geometrical parameters according to literature. A total of eleven models were produced where only one of them is clean as a base model, the others were modified. The present rotor blades with diameter of 0.28 m were scaled down from the original scale rotor blade with diameter of 0.6 m that is designed to operate at Reynolds number of $1 \cdot 10^5$. These blade models were processed to obtain a smoother surface but were not dyed. The turbine test models were then tested in the wind tunnel under chord-based Reynolds number of $4.7 \cdot 10^4$ for different free stream conditions to estimate the power performance of each wind turbine. The obtained experimental results of airfoils and turbines were corrected for tunnel blockage.

4.1 Wind Tunnel Description

In this study, a low-speed open-circuit wind tunnel (Figure 4.1) with closed test-section with a velocity range up to 30 m/s were used. This facility is installed in the Laboratory of Aerdoynamics in Niğde Ömer Halisdemir University. The cross section area of the test section is squared with dimensions of 0.57 m x 0.57 m at the inlet but its side walls take a slope of 0.3 degrees towards the exit to obtain a constant static pressure throughout the test section. The test section is made of plexiglass material and has a length of 1.0 m. The tunnel turbulence intensity is smaller than 1% for free stream velocity range of 3 m/s to 20 m/s.

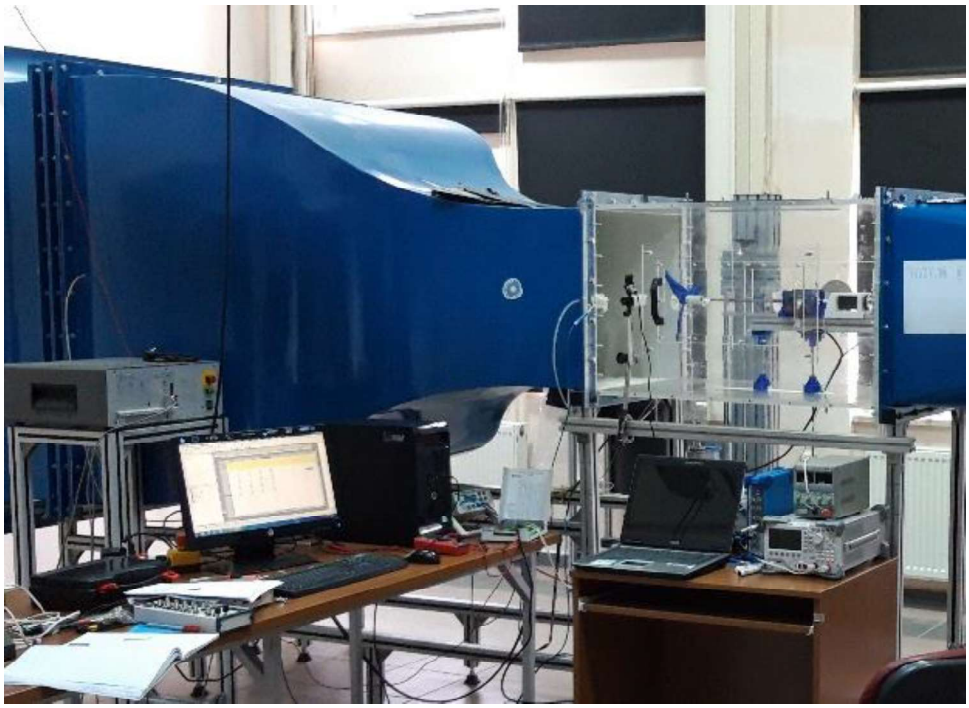

Figure 4.1. Niğde Ömer Halisdemir University open-circuit wind tunnel with closed test section

The wind tunnel is calibrated before starting the test measurements to determine the correlation factor that relates the dynamic pressure at the model mount location in test section with the dynamic pressure at the inlet of test section for empty test section condition. Also, interference objects were taken into consideration.

4.2 Aerodynamic Testing Of Airfoils

Before experimental testing takes place, a series of steps are taken to prepare the models for tunnel testing which are introduced in the following.

4.2.1 Airfoil manufacturing

Airfoil profiles were modeled in Solidworks with chord length of 150 mm and a span of 450 mm and printed in a 3D Printer with acrylonitrile butadiene styrene (ABS) plastic material as shown in Figure 4.2. Then, the surfaces of the models are further processed and dyed in order to have a more clean, smooth and homogeneous final surfaces (Figure 4.3).

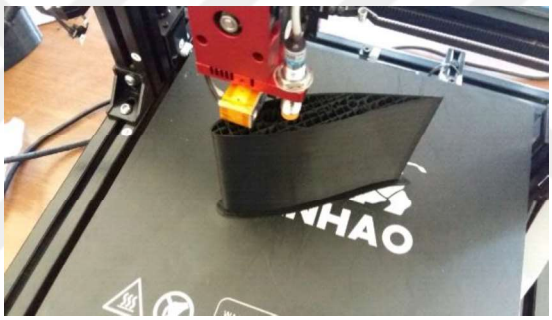

Figure 4.2. Airfoil profile in the process of printing

Figure 4.3. Final state of an airfoil profile

4.2.2 Airfoil experimental setup

The airfoil is mounted into the test section at a distance of 0.255 m from the nozzle until the leading edge. In Figure 4.4 experimental setup of airfoil wind tunnel testing is illustrated schematically which will be explain in the following paragraphs.

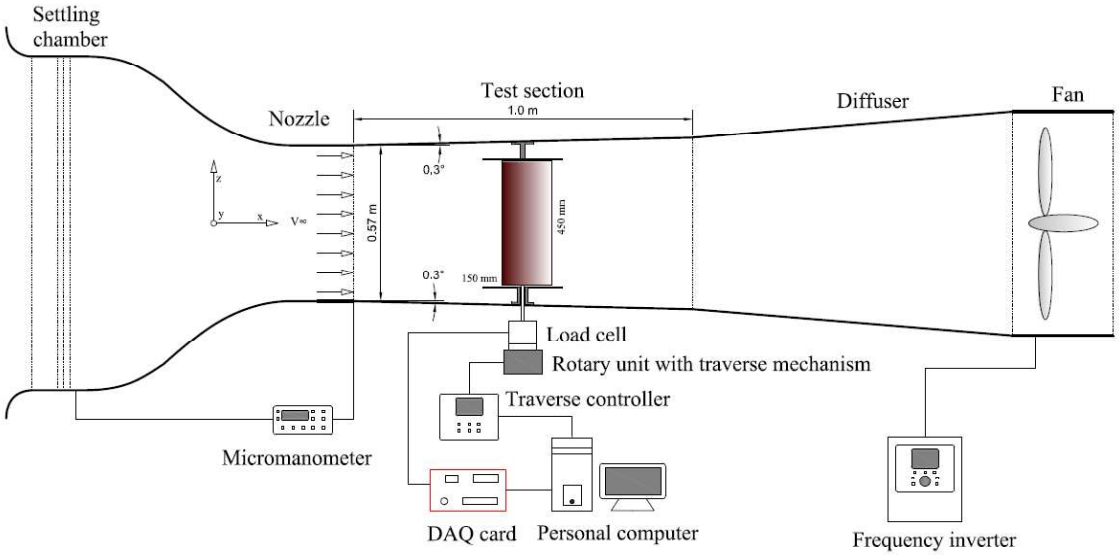

Figure 4.4. 2D schematic view of wind tunnel experimental setup

At the beginning of the experimental work, four selected airfoil models from NREL and NACA airfoil families will be introduced (Figure 4.5).

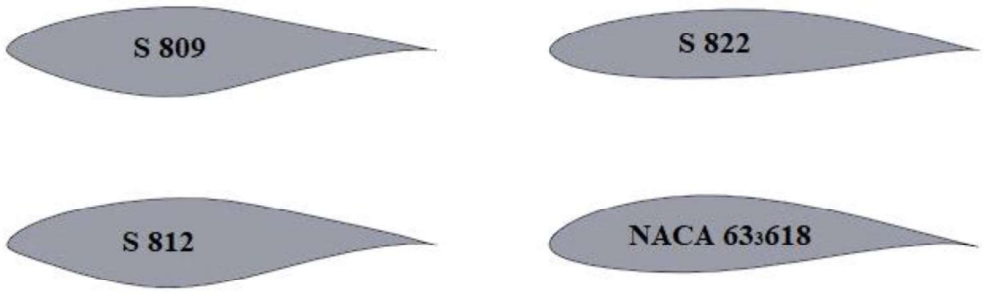

Figure 4.5. Selected airfoil section models for experimental investigation

In Table 4.1, the geometric characteristics of the selected airfoil models are presented.

Table 4.1. Geometric characteristics of the airfoil models

Airfoil name	Thickness (t/c), %	Camber (f/c), %
NREL S809	21% at 39.5%c	1% at 82.3%c
NREL S812	21% at 39.6%c	1.6% at 77%c
NREL S822	16% at 39.2%c	1.8% at 59.5%c
NACA $63_3$618	18% at 34.7%c	3.3% at 50%c

The next step is preparing the model to be mounted inside the test section for experimental investigations. Two thin endplates with diameter 0.28 m and 3 mm thick were attached at the edges of the models as shown in Figure 4.6.

Figure 4.6. Airfoil model with endplates

The airfoil model is mounted vertically inside the test section in the load cell that is connected to the rotary unit (Isel ZD 30) able to rotate about the vertical axis (Figure 4.7). Both load cell and rotary unit systems are assembled in 1-axis traverse mechanism able to adjust the aifoil in vertical direction. On the other hand, rotary unit is connected to a

machine controller (Isel C142-4) to be controlled by a computer, while the load cell is connected to the DAQ card inserted in the computer. A pitot-static tube for wind speed measurement connected to a micromanometer (ManoAir 500) were used to measure the free stream speed at the inlet of test section (Figure 4.8). Also, atmospheric pressure and temperature in the test section is measured with ManoAir500 device to obtain the density of airflow. To control the wind tunnel axial fan of 4 kW power at desired rotational speed, Schneider Altivar 71 model frequency inverter in the range of 0 to 50 Hz is utilized with an increment of 0.1 Hz.

Meanwhile, the aerodynamic forces, lift and drag forces, on airfoil models were measured with the help of a 6-Axis ATI Gamma DAQ F/T load cell. This device is capable of measuring a force magnitude up to ±32 N in the *x-axis* (F_x) and *y-axis* (F_y) and up to ±100 N in the z-axis (F_z) and torques (T_x, T_y, T_z) up to ±2.5 Nm about them and is mounted above the rotary unit that is connected to the 1-axis traverse mechanism.

All experimental data were collected at a sample rate of 500 Hz in a period of 22 seconds in a personal computer through a data acquisition system NI PCIe-6323 DAQ card which has 32 single ended analog to digital converter channel with a maximum sampling frequency 250 kHz. This resulted in a total number of 11000 recordings for a single measurement at each angle of attack.

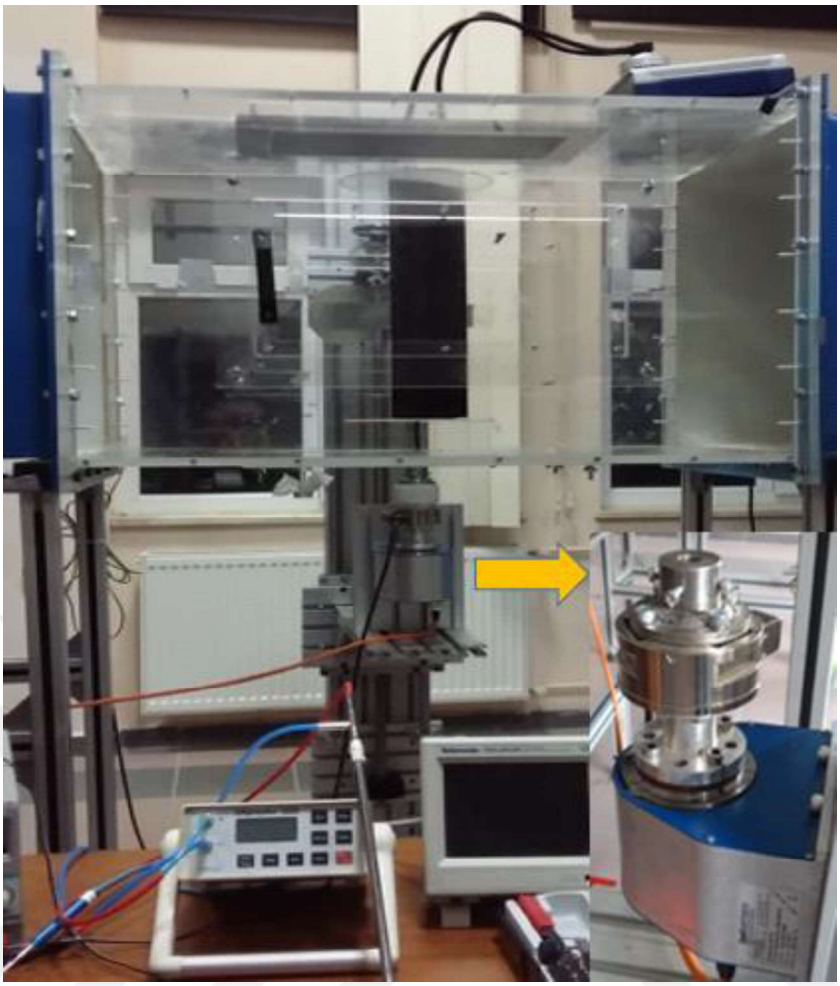

Figure 4.7. The airfoil profile mounted inside test section and in the load cell-rotary unit

Figure 4.8. Micromanometer device type ManoAir 500

4.2.3 Airfoil testing procedure and data recording

After setting up the system, the experiment started by operating the wind tunnel at different flow conditions. The experimental measurements were performed at two

Reynolds numbers: $Re = 5 \cdot 10^4$ corresponding to free stream speed $V = 6.4$ m/s (18.3 Hz) and $Re = 1 \cdot 10^5$ corresponding to free stream velocity of $V = 12.7$ m/s (33.9 Hz), and at various angles of attack ranging from -20^0 to $+20^0$ with increment of 1° (Figure 4.9). For each load setting the aerodynamic coefficients are measured, and finally the polar curves are plotted. The measurements were repeated two times for each test models: S809, S812, S822, and NACA 63_3618 at given Reynolds angles of attack.

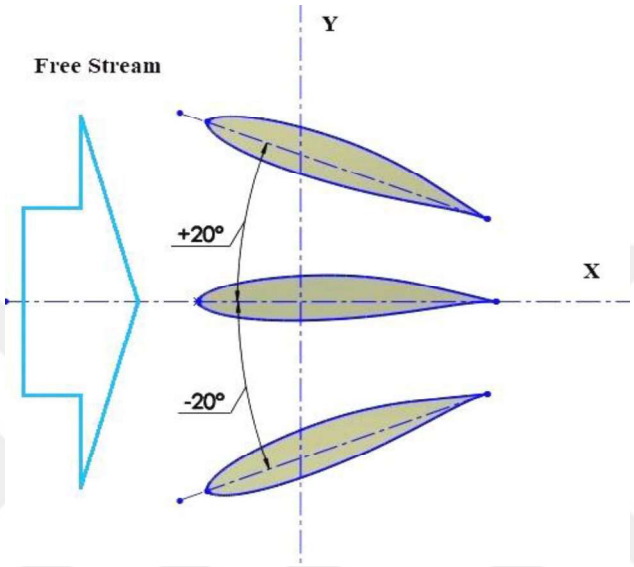

Figure 4.9. Orientation of the positive and negative angles of attack

4.2.4 Blockage correction for airfoil experiments

All airfoil data, lift and drag coefficients, obtained from the experimental testing were corrected according to Van Treuren (2015) approach as follow;

The total correction factor;

$$\varepsilon_T = \varepsilon_{sb} + \varepsilon_{wb} \tag{4.1}$$

The solid blockage correction factor;

$$\varepsilon_{sb} = \frac{K \cdot V_M}{A_{ts}^{3/2}} \tag{4.2}$$

Where; $K = 0.52$ for vertical wing spaning, V_M - model volume (m^3), A_{ts} – tunnel cross-sectional area.

The wake blockage correction factor;

$$\varepsilon_{wb} = \left(\frac{c}{2 \cdot h_{ts}}\right) \cdot C_{Du} \tag{4.3}$$

Where; c – airfoil chord length, C_{Du} – uncorrected drag coefficient, h_{ts} – height of the test section.

The streamline curvature correction factor;

$$\sigma_{sc} = \frac{\pi^2}{48} \cdot \left(\frac{c}{h_{ts}}\right)^2 \tag{4.4}$$

Where; c – airfoil chord length, h_{ts} – height of the test section.

Correction factors applied to aerodynamic coefficients:

$$V_c = V_u \cdot (1 + \varepsilon_T) \tag{4.5}$$

$$q_c = q_u \cdot (1 + 2 \cdot \varepsilon_T) \tag{4.6}$$

$$Re_c = Re_u \cdot (1 + \varepsilon_T) \tag{4.7}$$

$$\alpha_c = \alpha_u + \left(\frac{1}{8 \cdot \pi} \cdot \frac{c^2}{{h_{ts}}^2 + (c/4)^2} + \frac{1}{2 \cdot \pi} \cdot \sigma_{sc}\right) \cdot C_{Lu} \tag{4.8}$$

$$C_{Lc} = C_{Lu} \cdot (1 - \sigma_{sc} - 2 \cdot \varepsilon_T) \cdot \frac{q_u}{q_c} \tag{4.9}$$

$$C_{Dc} = C_{Du} \cdot (1 - 3 \cdot \varepsilon_{sb} - 2 \cdot \varepsilon_{wb}) \cdot \frac{q_u}{q_c} \tag{4.10}$$

Subsriptions u and c denotes uncorrected and corrected values, respectively. Uncorrected values are initially correlated to the dynamic pressure measured at empty test section wind tunnel condition.

4.3 Wind Turbine Rotor Blade Design And Testing

Based on data obtained from the experimental measurements of four proposed airfoils, NREL S822 section has shown the highest level of performance in two Reynolds numbers, therefore this profile was selected as the most dedicated profile.

4.3.1 Design of the wind turbine rotor blade geometry

The original scale rotor blade geometry is designed according to the Schmitz equations described in subchapter 1.3.3.1, steps 1 to 6, based on the following input data:

- Rotor diameter: $D = 0.6$ m
- Wind speed: $V_d = 9$ m/s
- Number of blades: $B = 3$
- Design tip Speed Ratio: $\lambda_d = 3.658$
- Lift coefficient: $C_L = 0.9256$
- Drag coefficient: $C_D = 0.02168$
- Design angle of attack: $\alpha_d = 8.5^0$
- Maximum lift to drag ratio: $C_L / C_D = 42.7$
- Number of blade elements: $N = 10$
- Air density: $\rho = 1.225$ kg/m^3

The above values for aerodynamic characteristics of the airfoil S822 were taken for $Re = 1 \cdot 10^5$ and $Ncri = 9$ from the website www.airfoiltools.com. Instead of experimental data obtained from the airfoils in the wind tunnel, the theoretical results from this website were used in the calculations as they provide full two-dimensional flow conditions and are more accurate especially for drag force values. In Table 4.2, chord and and twist angle distributions of the original scale wind turbine blade are presented.

Table 4.2. Chord and twist distributions of original scale wind turbine blade

Station	r_i (mm)	λ_i	c_i (mm)	β_i (°)	Airfoil
Hub	35	/	/	/	/
1	60	0.73	103.0	27.4	S822
2	84	1.02	98.8	21.0	S822
3	108	1.32	90.2	16.3	S822
4	132	1.61	81.1	12.7	S822
5	156	1.90	72.9	10.0	S822
6	180	2.19	65.7	7.8	S822
7	204	2.49	59.6	6.1	S822
8	228	2.78	54.4	4.7	S822
9	252	3.07	50.0	3.5	S822
10	276	3.37	46.2	2.5	S822
11	300	3.66	42.9	1.7	S822

The original wind turbine blade geometry is scaled down to 0.28 m in diameter by using similarity laws according to Brusca *et al.* (2014) approach. In Table 4.3, chord and twist angle distributions of scaled wind turbine blade geometry are presented.

Table 4.3. Chord length and twist angle distributions of scaled wind turbine blade

Station	r_i (mm)	λ_i	c_i (mm)	β_i (°)	Airfoil
Hub	16.33	/	/	/	/
1	28.00	0.73	48.1	27.4	S822
2	39.20	1.02	46.1	21.0	S822
3	50.40	1.32	42.1	16.3	S822
4	61.60	1.61	37.9	12.7	S822
5	72.80	1.90	34.0	10.0	S822
6	84.00	2.19	30.7	7.8	S822
7	95.20	2.49	27.8	6.1	S822
8	106.40	2.78	25.4	4.7	S822
9	117.60	3.07	23.3	3.5	S822
10	128.80	3.37	21.5	2.5	S822
11	140.00	3.66	20.0	1.7	S822

4.3.2 Generation of wind turbine blade configurations

The original scale model of the rotor with a diameter of 0.6 m is scaled down to a suitable size of 0.28 m in diameter adapting to the laboratory conditions to obtain sufficient torque and then tunnel blockage corrections are made for a blockage ratio of 18.9%.

Several configurations of blades were generated with the help of two passive flow control techniques as depicted in Tables 4.4 through 4.14. In these tables, the generated configurations named according to the prefix M denoting the model associated with the ordinal number from 1 to 11 based on this methodology are presented.

By employing the leading edge turbercles technique according to Hansen *et al.* (2011) and Abate *et al.* (2019) approaches, five configurations were generated (Tables 4.5 through 4.9). The wavy shape of leading edge is calculated using Eq. 1.52, where the amplitude A_m of the wave is calculated by multiplying the average chord length (c_{avg}) of the blade by 0.03, 0.06, 0.09, 0.11, and 0.14. Meanwhile, the wave length λ_m is calculated by multiplying the average chord length (c_{avg}) of the blade by 0.11, 0.14, 0.22, 0.29, and 0.43. The wave starts from x = 60 mm up to 300 mm for full scale wind turbine rotor blades while for scaled down wind turbine rotor blades it starts from x = 28 mm up to 140 mm.

In this study, the average chord length (c_{avg}) of the present wind turbine rotor blades is 32.4 mm (Table 4.3).

On the other hand, by applying vortex cavity or backward-facing step technique on the upper surface of the blade, four blade configurations were generated according to Fertis (1994), Witherspoon and Finaish (1996), and Finaish and Witherspoon (1998) approaches. According to this methodology, the cavity is constructed according to Eq. 1.53 by taking the step distance X_u from leading edge which is determined by multiplying the average chord length (c_{avg}) of the blade by 0.3, 0.4, and 0.5. In the same way, the step size L_u is calculated by multiplying the average chord length (c_{avg}) of the blade by 0.1, 0.2, 0.25, and 0.3. The step depth D_u is calculated by multiplying the airfoil thickness t by 0.19, 0.20, 0.35, and 0.5. In Tables 4.10 through 4.13, all configurations generated

based on this methodology are presented. In the below tables (Tables 4.4 through 4.14), all blade configurations of wind turbine rotors are presented.

Table 4.4. M1 – Base rotor blade model

Description	Designation	3D View
Clean blade model (base model)	M1	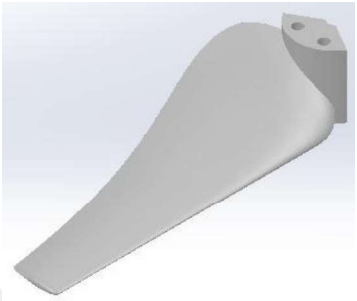

Table 4.5. M2 – Tubercled rotor blade model - A1λ3.5

Flow control technique	Designation	3D View
Leading edge tubercles 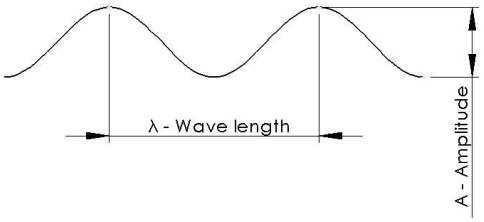	M2	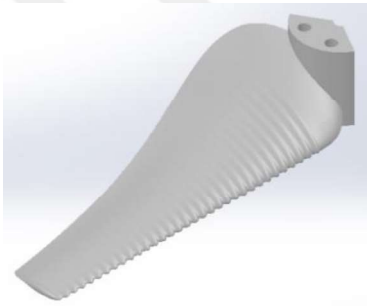
$A_m = 0.03 \cdot c_{avg} \approx 1$ mm $\lambda_m = 0.11 \cdot c_{avg} \approx 3.5$ mm	A1λ3.5	

Table 4.6. M3 – Tubercled rotor blade model – A2λ5

Flow control technique	Description	3D View
Leading edge tubercles 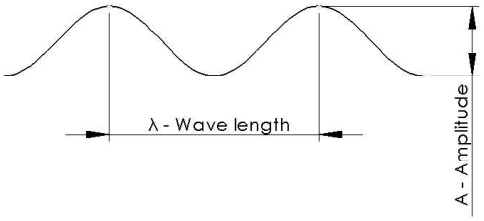	M3	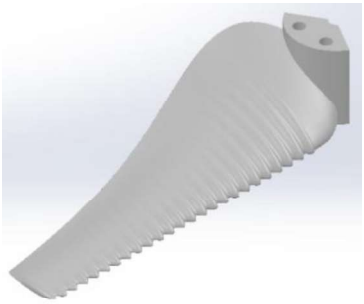
$A_m = 0.06 \cdot c_{avg} \approx 2$ mm $\lambda_m = 0.14 \cdot c_{avg} \approx 5$ mm	A2λ5	

Table 4.7. M4 – Tubercled rotor blade model – A3λ7

Flow control technique	Description	3D View
Leading edge tubercles 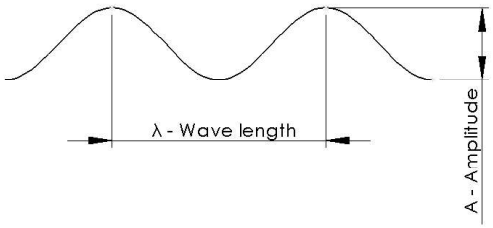	M4	
$A_m = 0.09 \cdot c_{avg} \approx 3$ mm $\lambda_m = 0.22 \cdot c_{avg} \approx 7$ mm	A3λ7	

Table 4.8. M5 – Tubercled rotor blade model – A4λ9

Flow control technique	Description	3D View
Leading edge tubercles 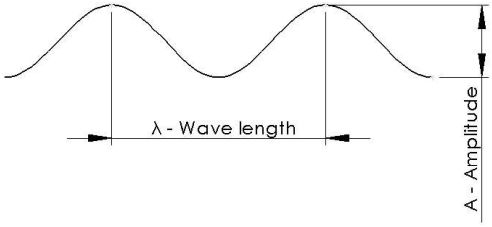	M5	
$A_m = 0.11 \cdot c_{avg} \approx 4$ mm $\lambda_m = 0.29 \cdot c_{avg} \approx 9$ mm	A4λ9	

Table 4.9. M6 – Tubercled rotor blade model – A5λ14

Flow control technique	Description	3D View
Leading edge tubercles 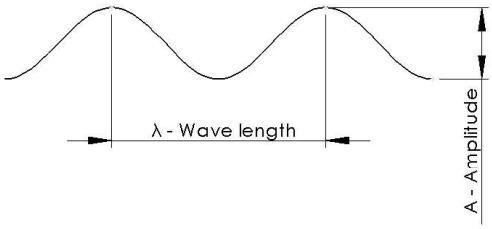	M6	
$A_m = 0.14 \cdot c_{avg} \approx 5$ mm $\lambda_m = 0.43 \cdot c_{avg} \approx 14$ mm	A5λ14	

Table 4.10. M7 – Vortex cavity rotor blade model – X30cL10cD20t

Flow control technique	Description	3D View
Vortex cavity 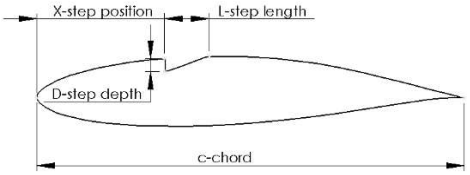	M7	
$X_u = 0.3 \cdot c_{avg} \approx 10$ mm $L_u = 0.1 \cdot c_{avg} \approx 3$ mm $D_u = 0.2 \cdot t \approx 1$ mm	X30cL10cD20t	

Table 4.11. M8 – Vortex cavity rotor blade model – X40cL20cD35t

Flow control technique	Description	3D View
Vortex cavity 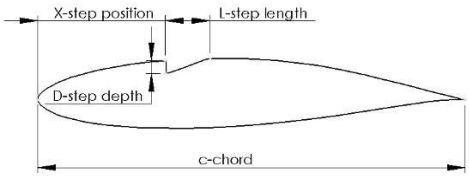	M8	
$X_u = 0.4 \cdot c_{avg} \approx 13$ mm $L_u = 0.2 \cdot c_{avg} \approx 6.5$ mm $D_u = 0.35 \cdot t \approx 2$ mm	X40cL20cD35t	

Table 4.12. M9 – Vortex cavity rotor blade model – X50cL25cD19t

Flow control technique	Description	3D View
Vortex cavity 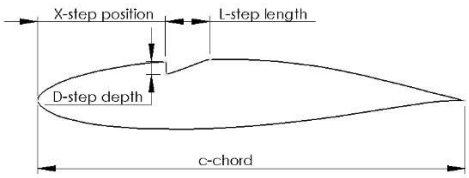	M9	
$X_u = 0.5 \cdot c_{avg} \approx 16$ mm $L_u = 0.25 \cdot c_{avg} \approx 8$ mm $D_u = 0.19 \cdot t \approx 1$ mm	X50cL25cD19t	

Table 4.13. M10 – Vortex cavity rotor blade model – X50cL30cD50t

Flow control technique	Description	3D View
Vortex cavity 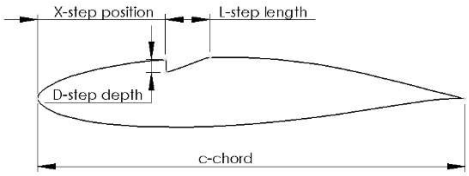	M10	
$X_u = 0.5 \cdot c_{avg} \approx 16$ mm $L_u = 0.3 \cdot c_{avg} \approx 10$ mm $D_u = 0.5 \cdot t \approx 2.5$ mm	X50cL30cD50t	

Table 4.14. M11 – Vortex cavity rotor blade model – Hybrid (M2+M9)

Flow control technique	Description	3D View
Vortex cavity 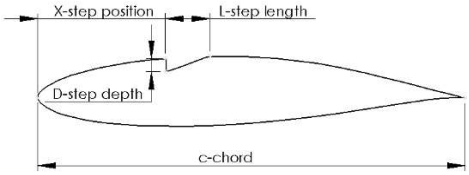	M11	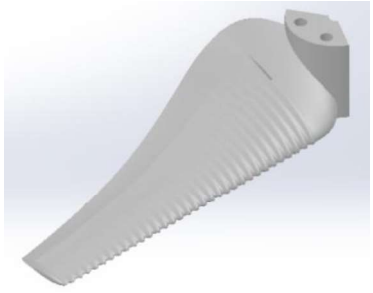
M2 + M9	A1λ3.5 X50cL25cD19t	

4.3.3 Wind turbine experimental set-up

Wind turbine rotors were tested in the wind tunnel laboratory in Niğde Ömer Halisdemir University. In Figure 4.10, an assembled rotor model is presented.

Figure 4.10. Small scaled wind turbine rotor model

The testing procedure began with the placement the rotor model in the center of the cross sectional area of the test section maintaining a distance of 0.28 m from test section inlet to the rotor plane as shown in Figure 4.11.

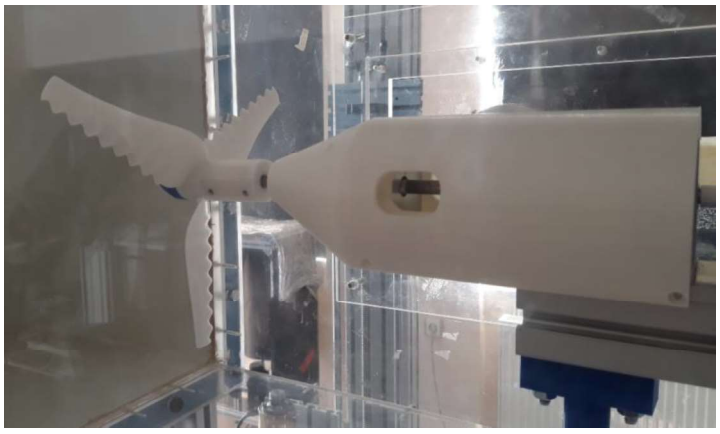

Figure 4.11. Wind turbine placed in the test section

In order to sense the torque and the rpm of the rotor shaft, a digital torque sensor DYN-200 with display resolution of 128x64, rated capacity ±0.5 Nm, DC power input of 24 V, maximum speed of 11000 rpm, accuracy of 1/1000, data filtering level set to its maximum of 100, is used (Figure 4.12). The torque sensor is installed between the rotor shaft and a

DC motor. In this case, the DC motor (Maxon RE50 Ø50 mm) with graphite brushes, nominal voltage of 24 V, capacity of 200 Watts, nomial speed of 5680 rpm, nominal torque of 0.405 Nm, maximum efficiency of 94%, is used as a brake mechanism to maintain rotor shaft at desired rpm despite the flow conditions (Figure 4.13).

Figure 4.12. The digital torque and tachometer sensor DYN-200

Figure 4.13. DC motor graphite brushed Maxon RE50 Ø50 mm

The wind turbine setup with all components assembled is depicted in Figure 4.14. The rotor shaft is supported by two bearings inside the cover to avoid longitudinal force and vibrations.

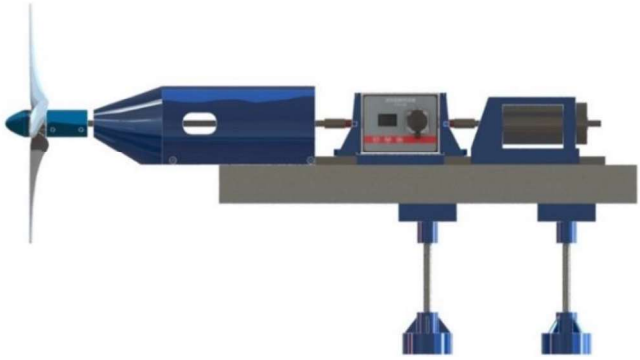

Figure 4.14. Wind turbine experimental setup

4.3.4 Wind turbine testing procedure and data recording

Designing the experimental research for studying and analyzing the wind turbine rotor performance and effectiveness is chosen based on pre-experimental work done on the rotor with clean blades (M1) in the wind tunnel.

4.3.4.1 Method 1: Constant free stream velocity

The rotor was tested under constant free stream speed condition at around 12 m/s where the rotor's rotational speed reached values from nearly 2500 rpm up to almost 4000 rpm for tip speed ratio between 2 and 5. The shaft rotations were controlled through the electronic load unit which exerted braking force through the DC motor. Electronic load of 8.4 Volts up to 14.8 Volts was applied with an increment of 0.4 Volts. Three cycles of measurements were made, where for each applied load three values for rpm and torque values were recorded through a digital camera from the torque sensor indicator screen (Figure 4.15).

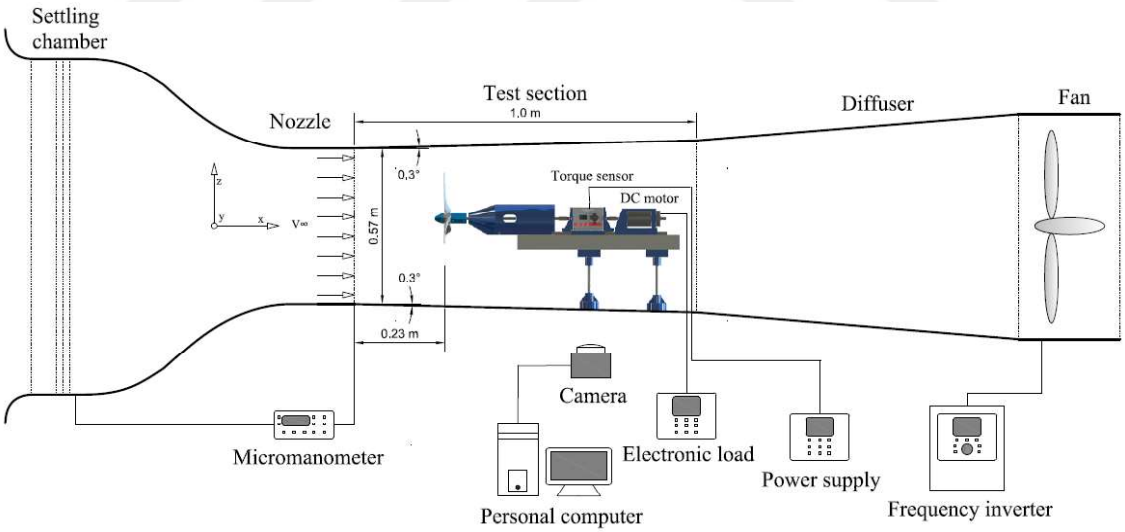

Figure 4.15. Illustration of the wind tunnel setup for wind turbine testing

4.3.4.2 Method 2: Constant angular velocity

This method is based on preserving the rotational speed of the rotor constant whereas varying the free stream speed. In this case, the appropriate number of rotations of the rotor

shaft was selected initially by taking into account the laboratory conditions. Hence, for the same free stream speed (12 m/s) as in the first try, the most convenient situation for the actual tunnel conditions was analyzed and the solution was sought for tip speed ratio of 3.5, 4, and 4.5 respectively. The appropriate number of rotations was found to be for tip speed ratio of 3.5 corresponding to 2866 rpm. Measurements were performed for tip speed ratio between 3 and 5. In this case, the rpm was controlled through the electronic load unit (ranging from 11 Volts up to 9.4 Volts) under different free stream speeds ranging from around 8.5 m/s up to around 14 m/s.

4.3.4.3 Method 3: Constant relative velocity

After analyzing the above two testing methods, it turns out that the relative velocity changes significantly, especially in the first method where this quantity reaches the values from around 40 m/s up to around 60 m/s for tip speed ratio from 3 to 5. Given the fact that the flow structure around any location on the blade profile depend mainly on the Reynolds number. Regarding the specifics of operations of the fixed-pitch rotors at variable wind speed regimes, it was more favorable to continue experimental research under constant tip chord-based Reynolds number at variable free stream velocities. That is, maintaining the relative velocity constant at the tip of the blade under variable tip speed ratios between 2 and 5.

This testing method was made considering the rotor speed of 2866 rpm and corresponding blade tip speed of 42 m/s for the rotor radius of 0.14 m, where the relative velocity of 43.29 m/s at the tip of the blade was selected for tip speed ratio of 4 and free stream speed of 10.5 m/s. This represents an intermediate value between tip speed ratio 3 and 5 and free stream speeds between 8.4 m/s and 14 m/s. Corresponding tip chord-based Reynolds number for this case is calculated according to Eq. 1.16 that is $4.7 \cdot 10^4$ taking into account tip chord length of 20 mm, air density of ~ 1 kg/m^3, relative velocity according to Eq. 1.17 that is 43.29 m/s, and air dynamic viscosity of $18.56 \cdot 10^{-6}$ for atmospheric pressure of 86 kPa and air temperature of 27 °C.

The experimental tests were performed for several free streams ranging from 9 to 15.5 m/s at the inlet of the test section. A DC motor is used as a brake to keep the rotor speed at desired rotations through applying electronic loads (Rigol DL3021 Precision) with

single channel, power up to 200 Watt, and single input/output 150V/40A/15kHz (Figure 4.16).

The rotor shaft torque and rotational speed on the other hand, are obtained from a digital torque sensor which is powered by a DC power supply (TT T-ECHNI-C YH-605D) (Figure 4.17). The wind turbine is fixed horizontally on an aluminium sigma profile connected with two rod supports to the bottom test section wall and the rotor shaft is coupled with the torque meter sensor and the DC motor. Both devices are linked to the control system and data acquisition devices. Each testing were repeated three times, and the curves obtained represent the average of these values of these measurements. Wind tunnel data were collected from a data acquisition system software NI PCIe-6323 DAQ card with 250 kHz maximum sampling frequency integrated into the computer.

Figure 4.16. Electronic load unit (Rigol DL3021 Precision)

Figure 4.17. DC power supply (TT T-ECHNI-C YH-605D)

The free stream, pressure, and temperature in the test section was measured using a pitot-static tube micro-manometer (ManoAir 500). The rotational speed of the rotor shaft was

monitored during the experiments by an optical laser rpm sensor (Monarch Instrument ROS) with OROS OR35 model external data acquisition and analyzer device as shown in Figure 4.18, while the variable free stream velocity in the wind tunnel is provided through a frequency inverter (Schneider electric, Altivar 71, 4 kW) (Figure 4.19).

Figure 4.18. Optical laser rpm sensor (Monarch Instrument ROS)

Figure 4.19. Frequency inverter (Schneider electric, Altivar 71, 4 kW)

For all rotor test cases, it was observed that the rotors did not start to operate for wind speeds lower than about 10 m/s due to the high resistive forces exerted mostly by the

bearings and DC motor. For this reason, a higher wind speed was initially applied to start the rotor and then adjusted to the corresponding speed.

4.3.5 Blockage correction for wind turbine experiments

Wind tunnel data, tip speed ratio and power coefficient, obtained from the experimental testing were corrected according to Van Treuren (2015) approach as follow;

The tunnel blockage factor is;

$$B_F = \frac{V}{V_e} \tag{4.11}$$

Where; V - free stream velocity with turbine installed (m/s), V_e – free stream velocity in empty test section (m/s).

Correction applied to tip speed ratio;

$$\lambda_c = \lambda_{c_u} \cdot B_F \tag{4.12}$$

Where; λ_{c_u} – uncorrected tip speed ratio, B_F – blockage factor.

Correction applied to power coefficient;

$$C_{p_c} = C_{p_u} \cdot {B_F}^3 \tag{4.13}$$

Where; C_{p_u} – uncorrected power coefficient, B_F – blockage factor.

CHAPTER V

EXPERIMENTAL RESULTS FOR AIRFOIL TESTING AND COMMENTS

In this chapter, all experimental results for airfoils and wind turbines obtained in the wind tunnel were presented. Wind tunnel blockage ratio for the case of airfoil testing is around 7.1% taking into account the frontal area of the airfoil created for the maximum angle of attack of ±20°.

5.1 Airfoil Testing Results

The aerodynamic properties of four blade profiles: S809, S812, S822, and NACA 63_3618 for various angles of attack were investigated in the wind tunnel. Experiments were accomplished on blade sections with chord length of 150 mm and span of 450 mm by changing the angle of attack from -20° to +20° with increment of 1° at two Reynolds numbers of $5 \cdot 10^4$ and $1 \cdot 10^5$. The theoretical results were obtained from the Xfoil results for standard turbulence level Ncrit = 9, which means that low disturbance is present in the flow. Otherwise, if this value decreases then much disturbance will be present.

As can be seen from the graphs from Figure 5.1 to 5.24, due to some factors such as the way the blades are manufactured and processed until they got the final shape after being dyed, and some other factors has resulted in discrepancies in the diagrams, especially in terms of drag coefficient.

5.1.1 Experimental results for S809 airfoil

In Figures 5.1, 5.2, and 5.3, lift and drag coefficients and lift to drag ratios against angles of attack are presented for S809 airfoil type. For Reynolds number of $5 \cdot 10^4$, the maximum lift coefficient of 0.86 is achieved at angle of attack of 13°. After that, there is a drop of the lift coefficient up to the angle of attack 15°. When the angle of attack exceeds 15°, the stall phenomenon takes place and it means that the flow separation is fully developed which leads to abrupt drop of the lift while increase of the drag. On the other hand, the maximum lift to drag ratio of 5.4 appears for the angle of attack 12°. From the theoretical

results the maximum lift is 0.88 at angle of attck 13° whereas the lift to drag ratio is 15.5 at the angle of attack 12.25°.

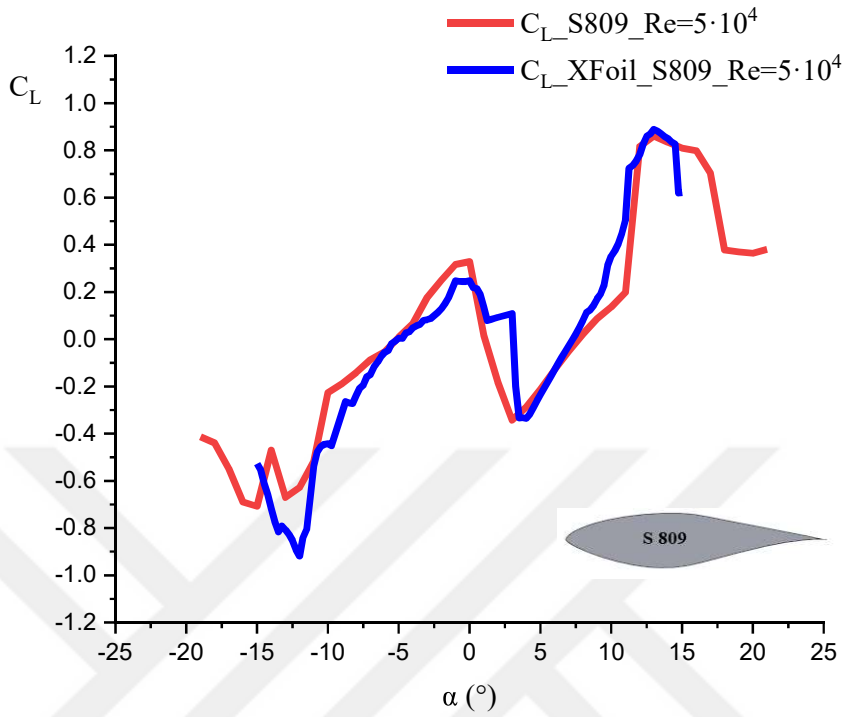

Figure 5.1. Lift curves for S809 at Re = $5 \cdot 10^4$

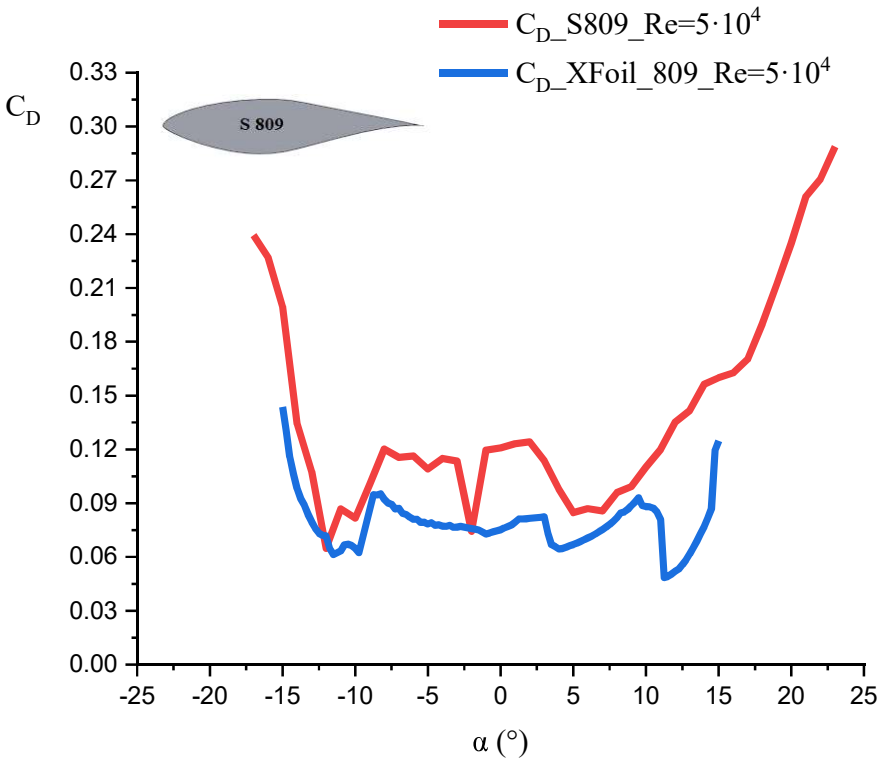

Figure 5.2. Drag curves for S809 at Re = $5 \cdot 10^4$

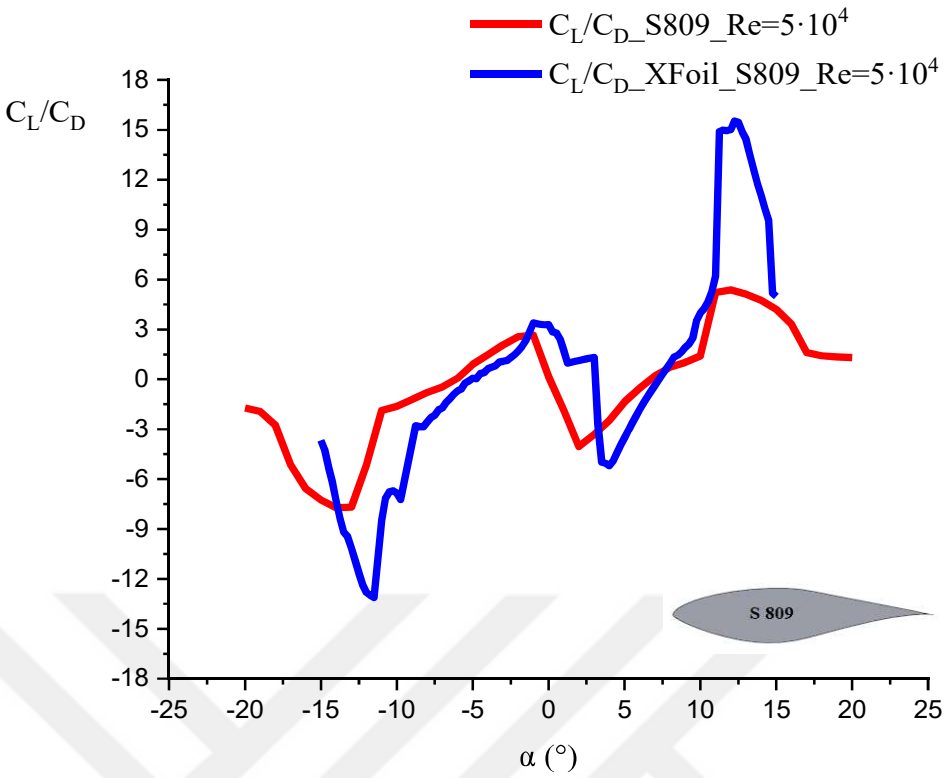

Figure 5.3. Lift to drag ratio curves for S809 at Re = $5 \cdot 10^4$

In Figures 5.4, 5.5, and 5.6, S809 airfoil type for Reynolds number of $1 \cdot 10^5$ reaches its maximum lift coefficient value of 0.84 at angle of attack 12°. The maximum lift to drag ratio of 5.2 occured at angle of attack 11°. From the theoretical results the maximum lift is 1.031 at angle of attack 13° whereas the lift to drag ratio is 23.4 at the angle of attack 10°.

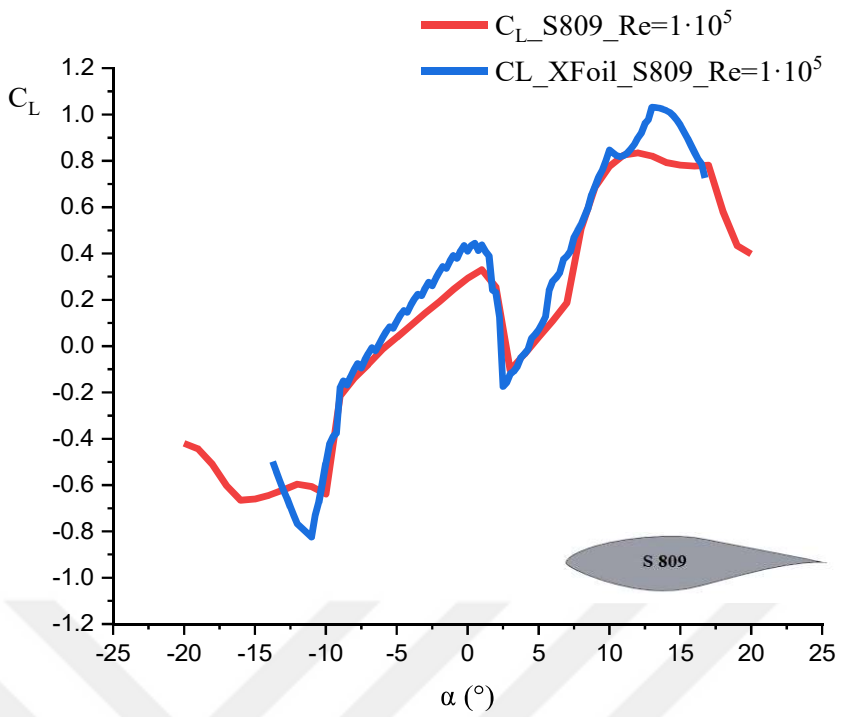

Figure 5.4. Lift curves for S809 at Re = $1 \cdot 10^5$

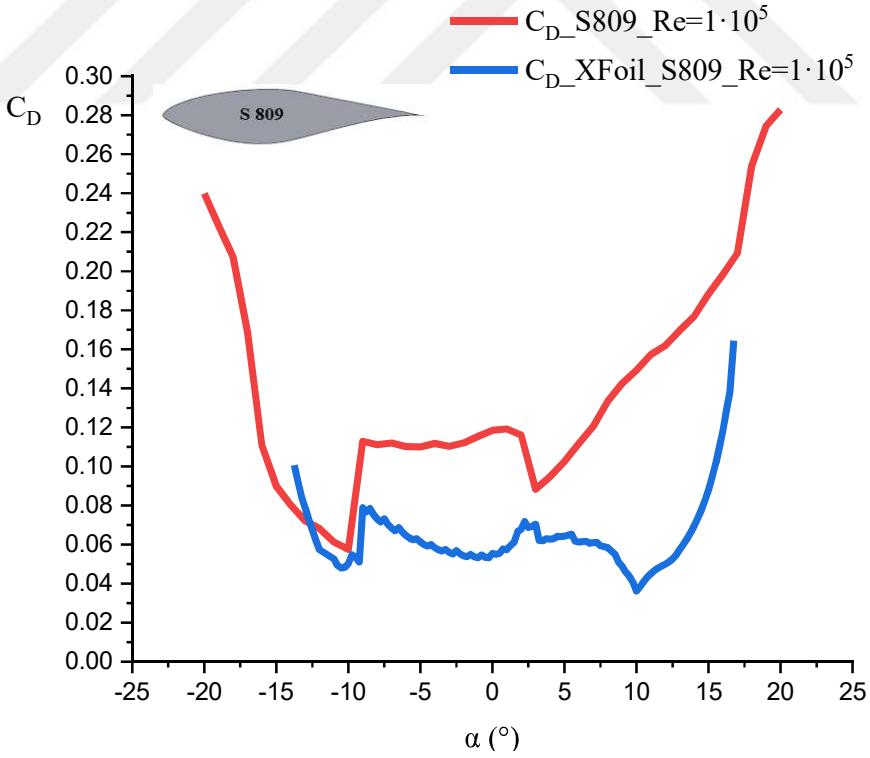

Figure 5.5. Drag curves for S809 at Re = $1 \cdot 10^5$

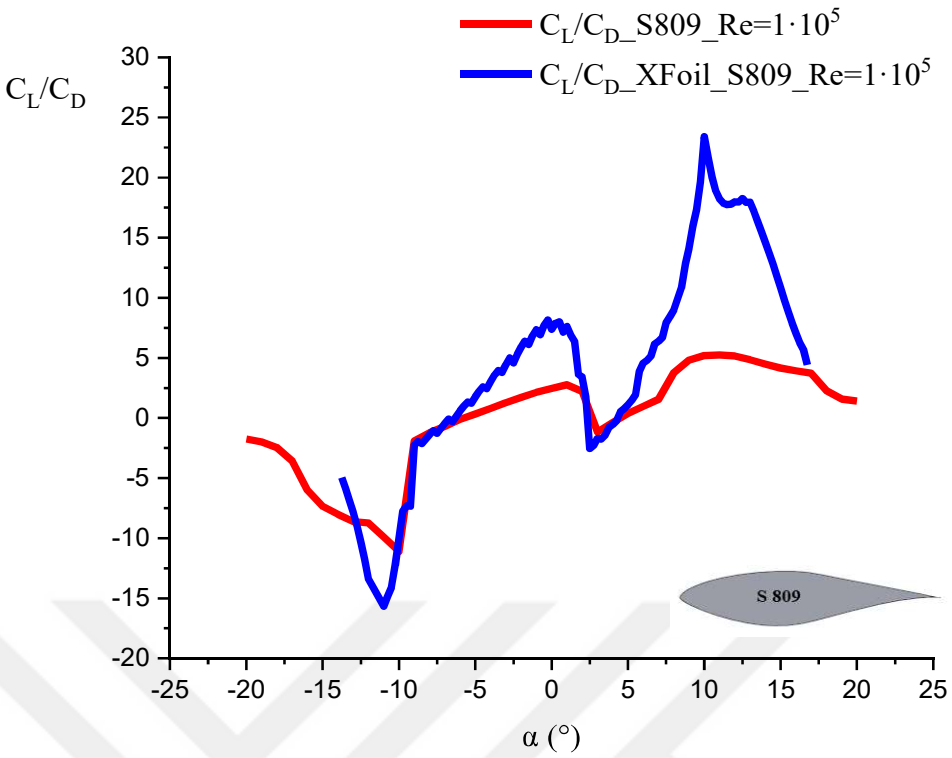

Figure 5.6. Lift to drag curves for S809 at Re = $1 \cdot 10^5$

5.1.2 Experimental results for S812 airfoil

In Figures 5.7, 5.8, and 5.9, S812 airfoil type for Reynolds number of $5 \cdot 10^4$ reaches its maximum lift coefficient value of 1.02 at angle of attack 14°. After that, there is a drop of the lift coefficient and the stall occur. The maximum lift to drag ratio of 11.5 appears for the angle of attack 12°. From the theoretical results the maximum lift is 1.011 at angle of attck 14.5° whereas the lift to drag ratio is 17.4 at the angle of attack 13.25°.

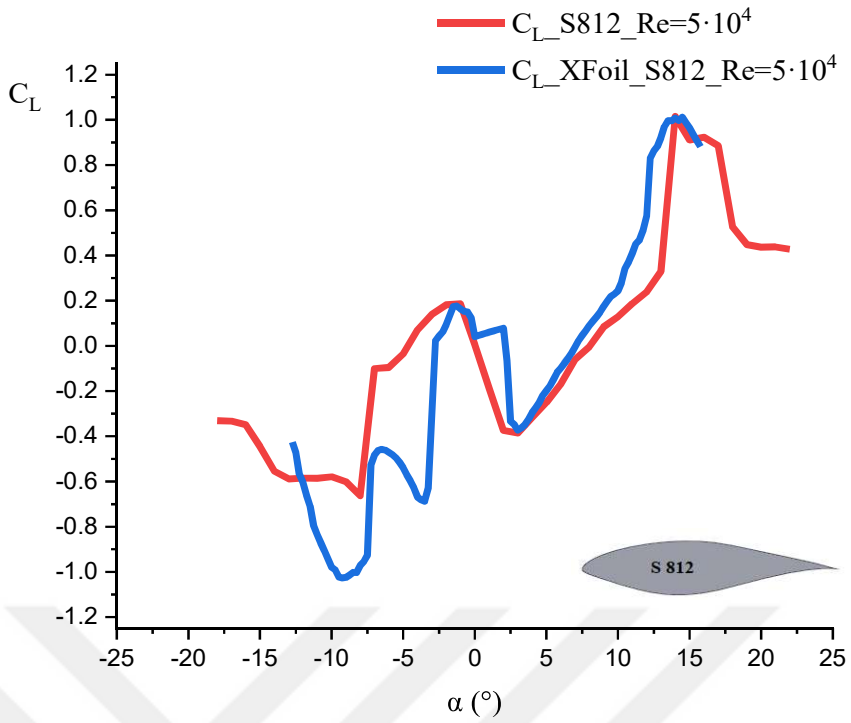

Figure 5.7. Lift curves for S812 at Re = $5 \cdot 10^4$

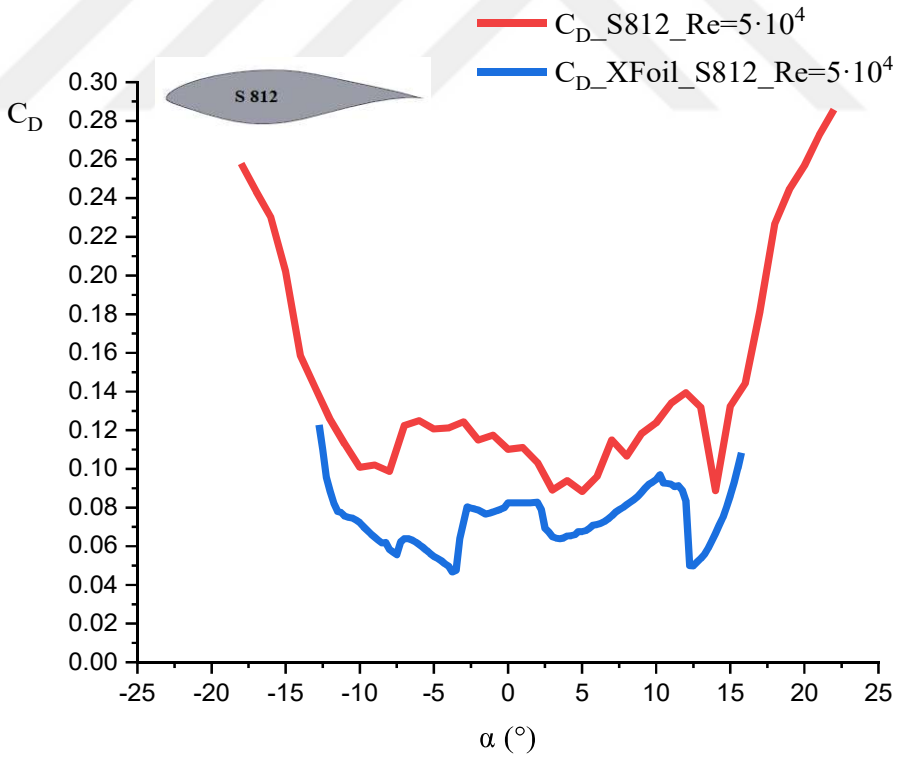

Figure 5.8. Drag curves for S812 at Re = $5 \cdot 10^4$

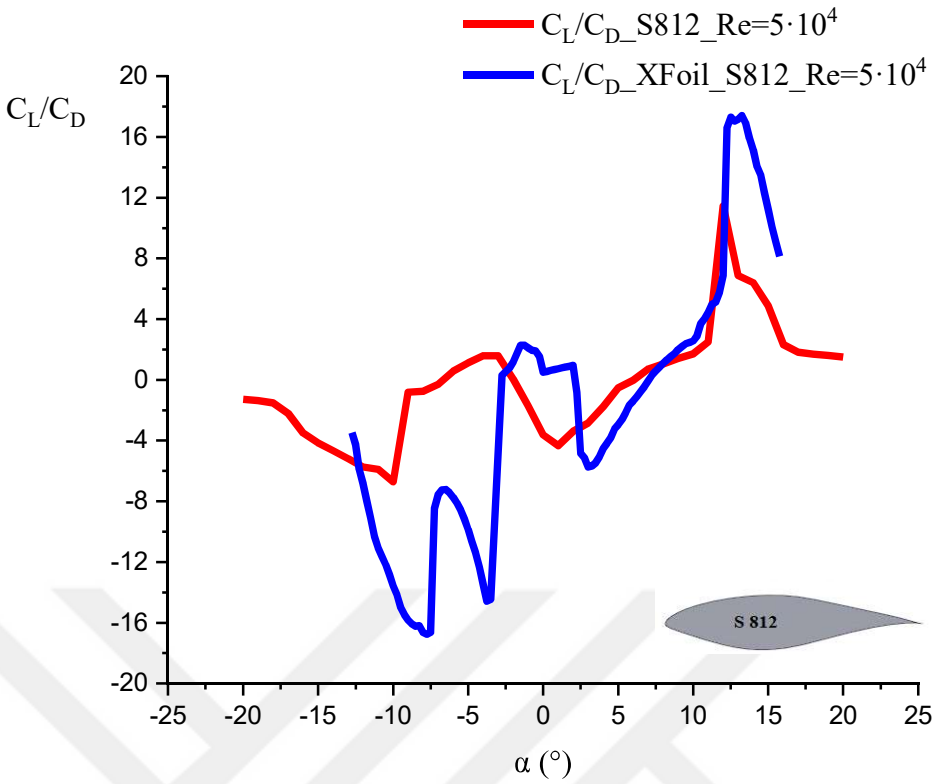

Figure 5.9. Lift to drag curves for S812 at Re = $5 \cdot 10^4$

While in Figures 5.10, 5.11, and 5.12, S812 airfoil type for Reynolds number of $1 \cdot 10^5$ reaches its maximum lift coefficient value of 0.92 at angle of attack 12°. The maximum lift to drag ratio of 6.7 occured at angle of attack 11°. From the theoretical results the maximum lift is 1.104 at angle of attck 15.5° whereas the lift to drag ratio is 23.9 at the angle of attack 11°. The experimental results for lift coefficient has a good agreement with the airfoiltools theoretical results. But, regarding to drag coefficient there are some deviations from the theoretical results. The small aspect ratio of airfoil test model and interference drag between the airfoil and the end plates may affects the two-dimensionality of flow. It is the main reason of differences between the experimental and theoretical drag coefficient results.

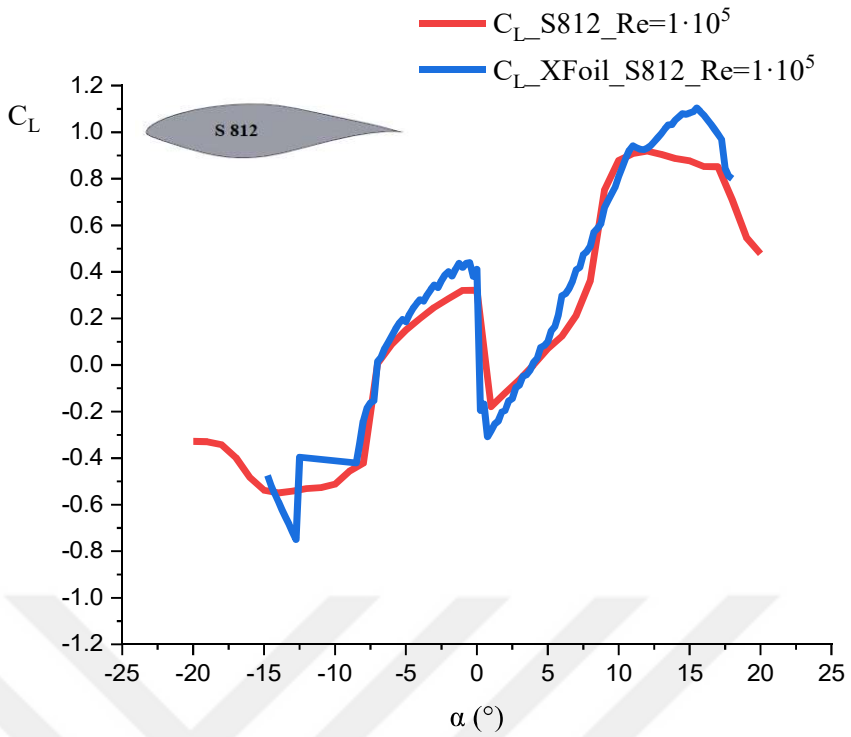

Figure 5.10. Lift curves for S812 at Re = $1 \cdot 10^5$

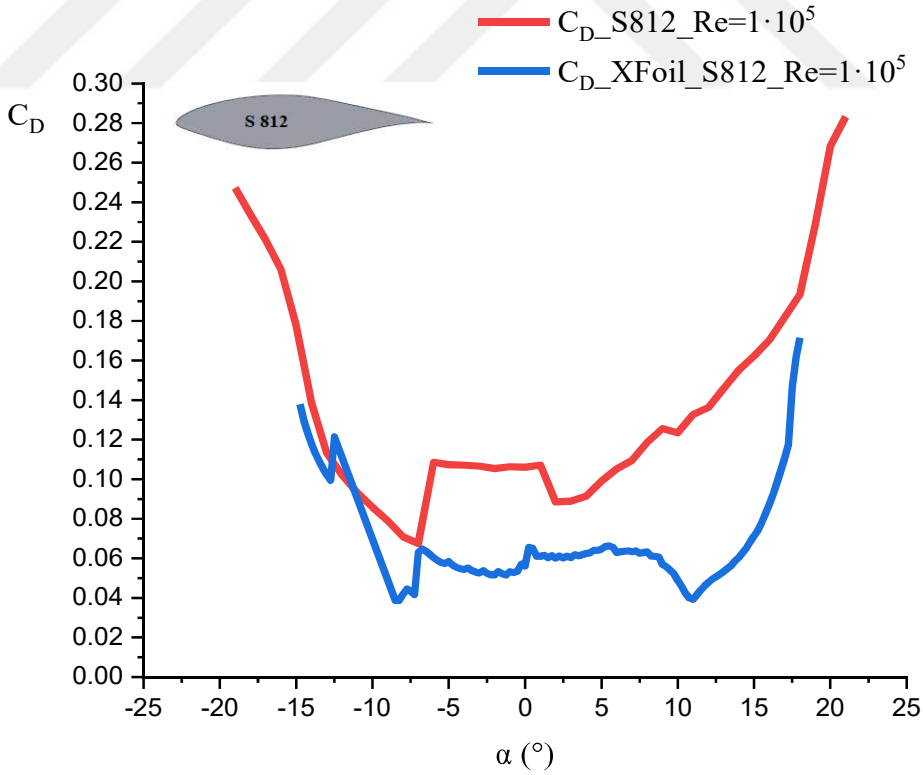

Figure 5.11. Drag curves for S812 at Re = $1 \cdot 10^5$

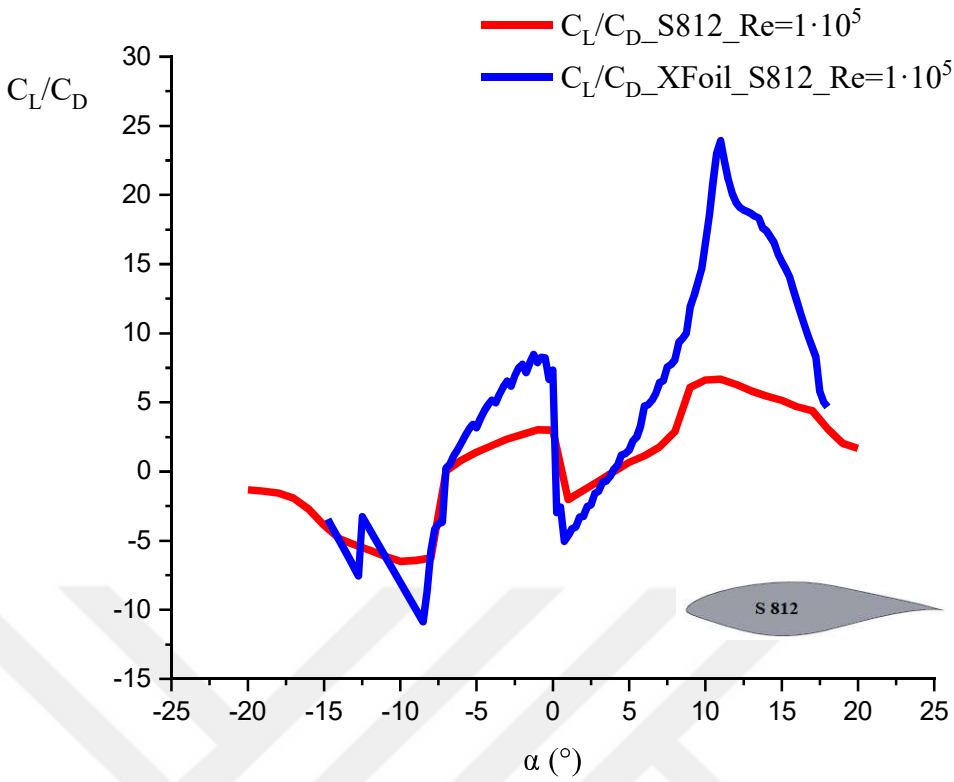

Figure 5.12. Lift to drag curves for S812 at Re = $1 \cdot 10^5$

5.1.3 Experimental results for S822 airfoil

Airfoil type S822 for Reynolds number of $5 \cdot 10^4$ shown in Figures 5.13, 5.14, and 5.15, reaches its maximum lift coefficient of 1.01 at angle of attack 14° and a maximum lift to drag ratio of 15.3 at angle of attack 11°. From the theoretical results the maximum lift is 1.13 at angle of attck 12° whereas the lift to drag ratio is 27.7 at the angle of attack 9.5°. The experimental results for lift coefficient has a good agreement with the airfoiltools theoretical results. But, regarding to drag coefficient there are some deviations from the theoretical results. The small aspect ratio of airfoil test model and interference drag between the airfoil and the end plates may affects the two-dimensionality of flow. It is the main reason of differences between the experimental and theoretical drag coefficient results.

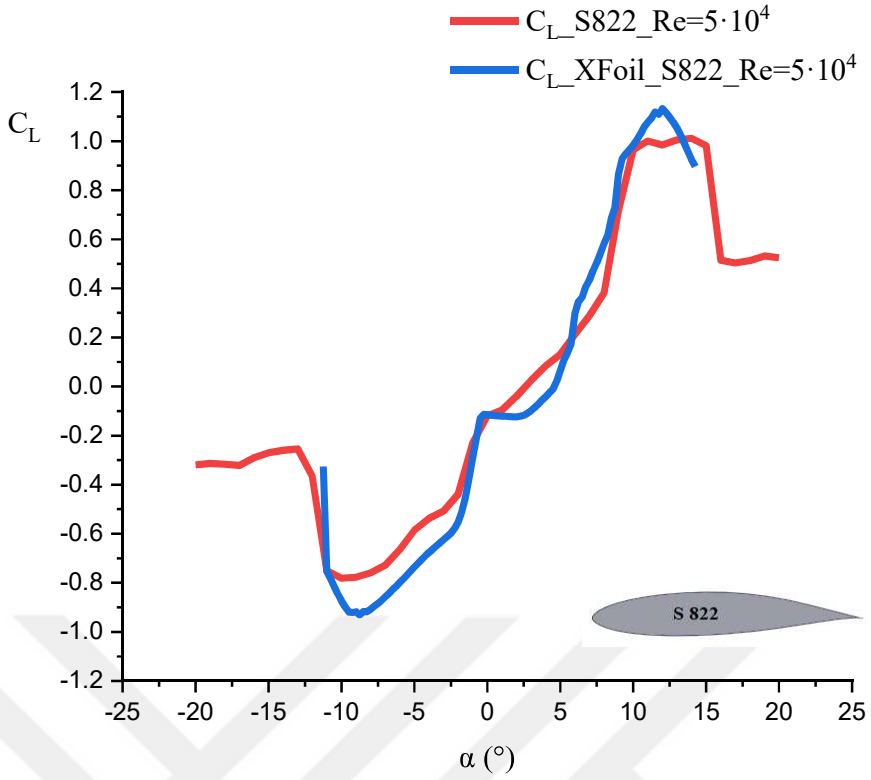

Figure 5.13. Lift curves for S822 at Re = $5 \cdot 10^4$

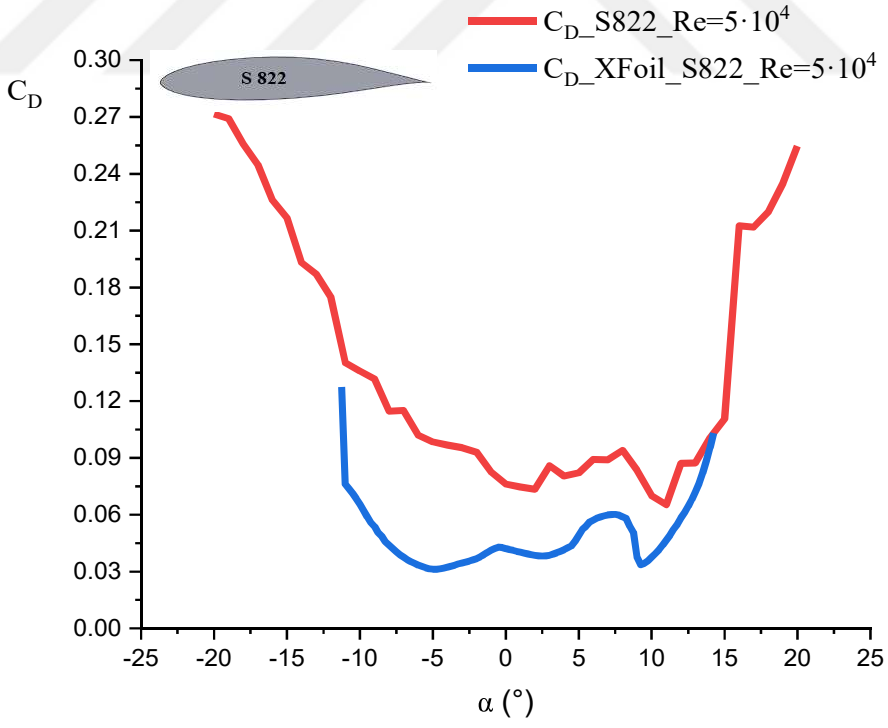

Figure 5.14. Drag curves for S822 at Re = $5 \cdot 10^4$

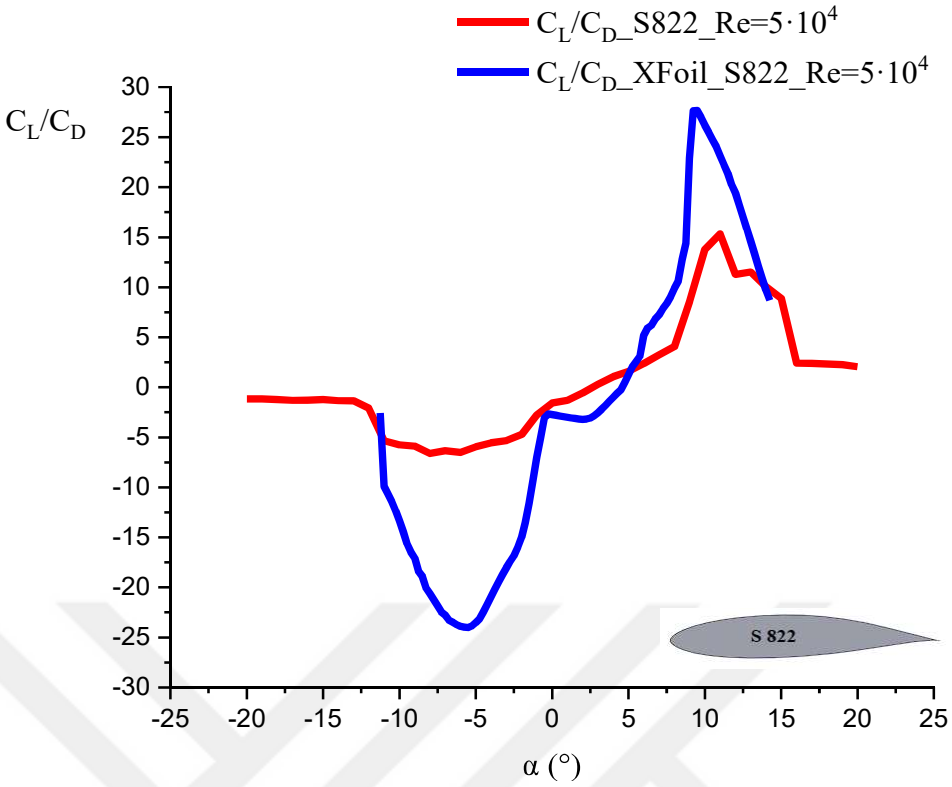

Figure 5.15. Lift to drag ratio curves for S822 at Re = $5 \cdot 10^4$

In Figures 5.16, 5.17, and 5.18, S822 airfoil type for Reynolds number of $1 \cdot 10^5$ reaches its maximum lift coefficient value of 0.99 at angle of attack 15° and has a maximum lift to drag ratio of 20.1 at angle of attack 9°. From the theoretical results the maximum lift is 1.15 at angle of attck 13° whereas the lift to drag ratio is 42.7 at the angle of attack 8.5°. The experimental results for lift coefficient has a good agreement with the airfoiltools theoretical results. But, regarding to drag coefficient there are some deviations from the theoretical results. The small aspect ratio of airfoil test model and interference drag between the airfoil and the end plates may affects the two-dimensionality of flow. It is the main reason of differences between the experimental and theoretical drag coefficient results.

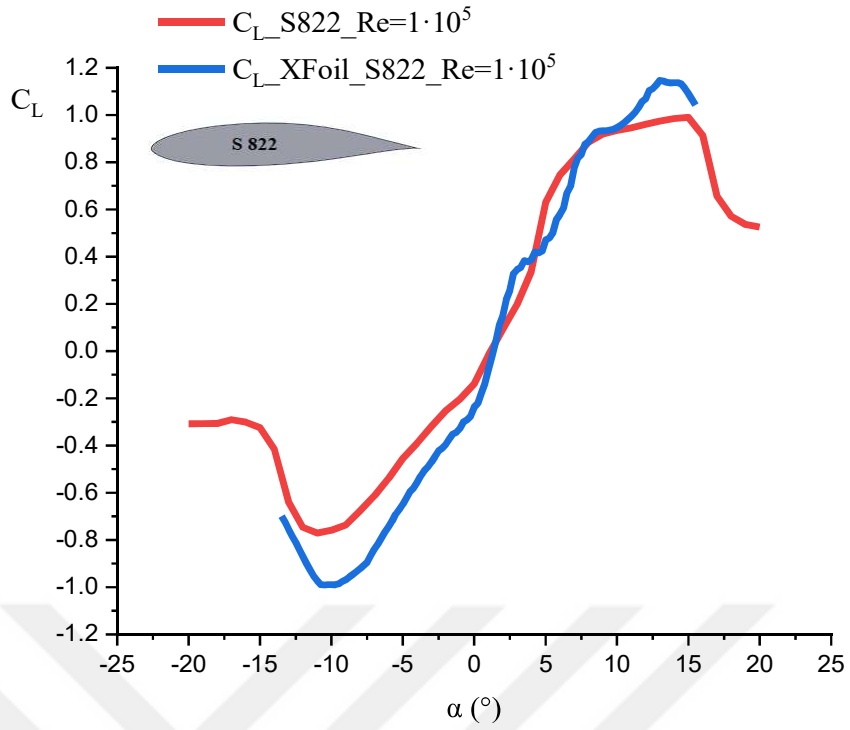

Figure 5.16. Lift curves for S822 at Re = $1 \cdot 10^5$

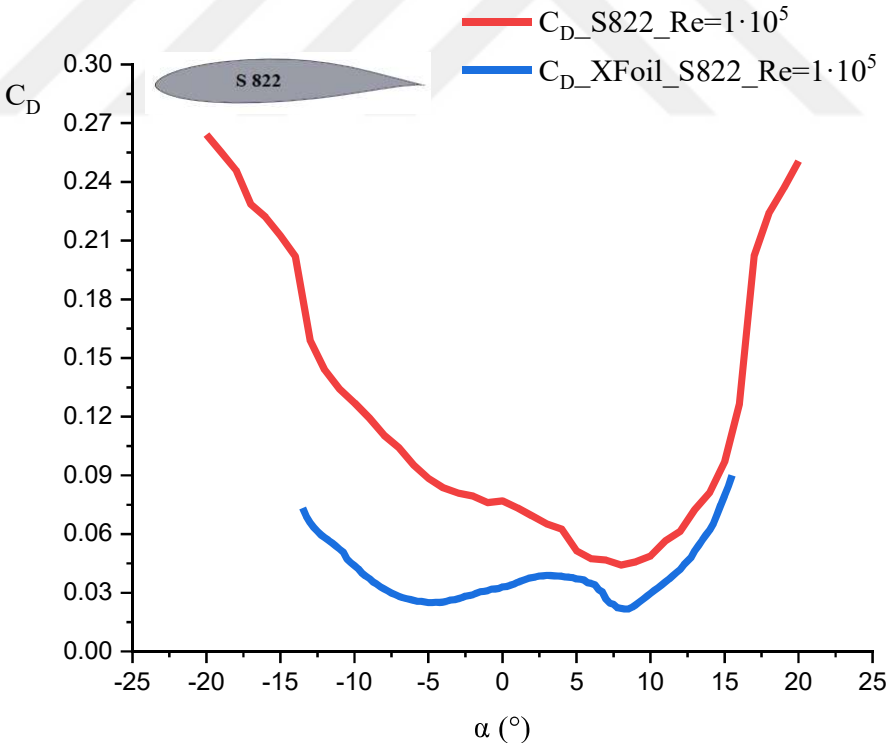

Figure 5.17. Drag curves for S822 at Re = $1 \cdot 10^5$

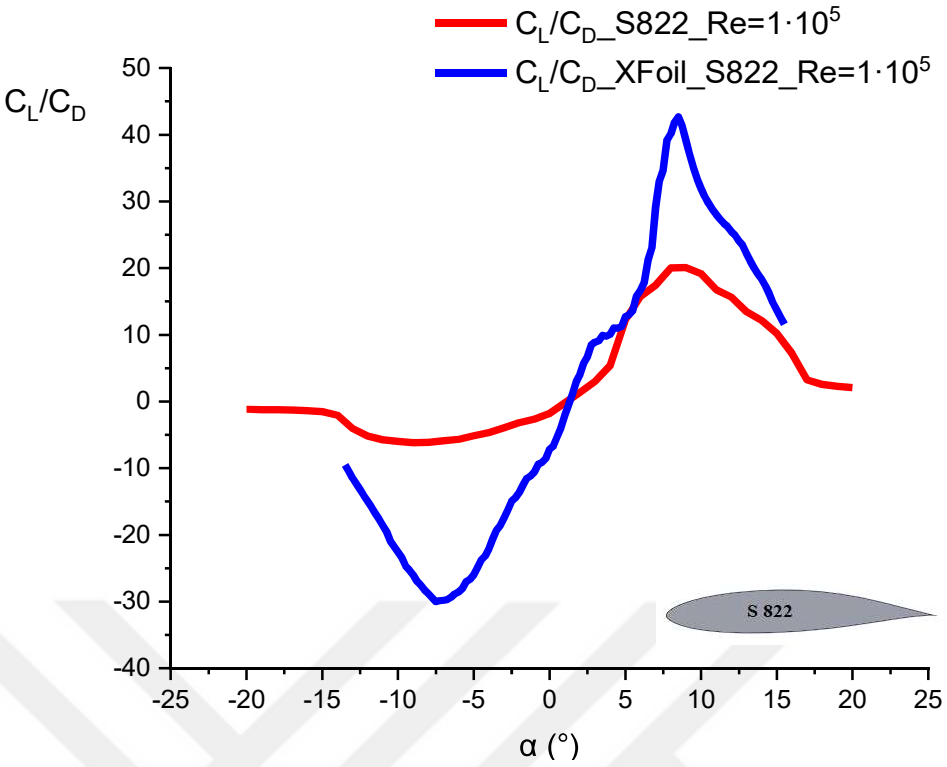

Figure 5.18. Lift to drag ratio curves for S822 at Re = $1 \cdot 10^5$

5.1.4 Experimental results for NACA63$_3$618 airfoil

In Figures 5.19, 5.20, and 5.21, NACA63$_3$618 airfoil type for Reynolds number of $5 \cdot 10^4$ reaches its maximum lift coefficient value of 0.58 at angle of attack 20°. The maximum lift to drag ratio of 2.6 appears for the angle of attack 11°. From the theoretical results the maximum lift is 0.62 at angle of attck 10.25° whereas the lift to drag ratio is 5.1 at the angle of attack 9.75°. The experimental results for lift coefficient has a good agreement with the airfoiltools theoretical results. But, regarding to drag coefficient there are some deviations from the theoretical results. The small aspect ratio of airfoil test model and interference drag between the airfoil and the end plates may affects the two-dimensionality of flow. It is the main reason of differences between the experimental and theoretical drag coefficient results.

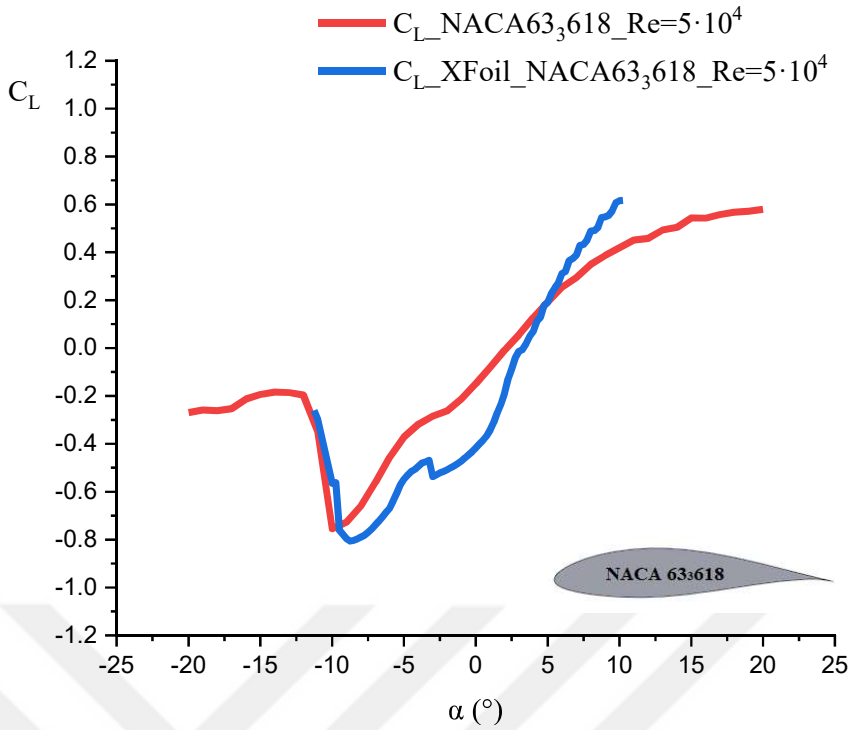

Figure 5.19. Lift curves for NACA 63$_3$618 at Re = 5·10^4

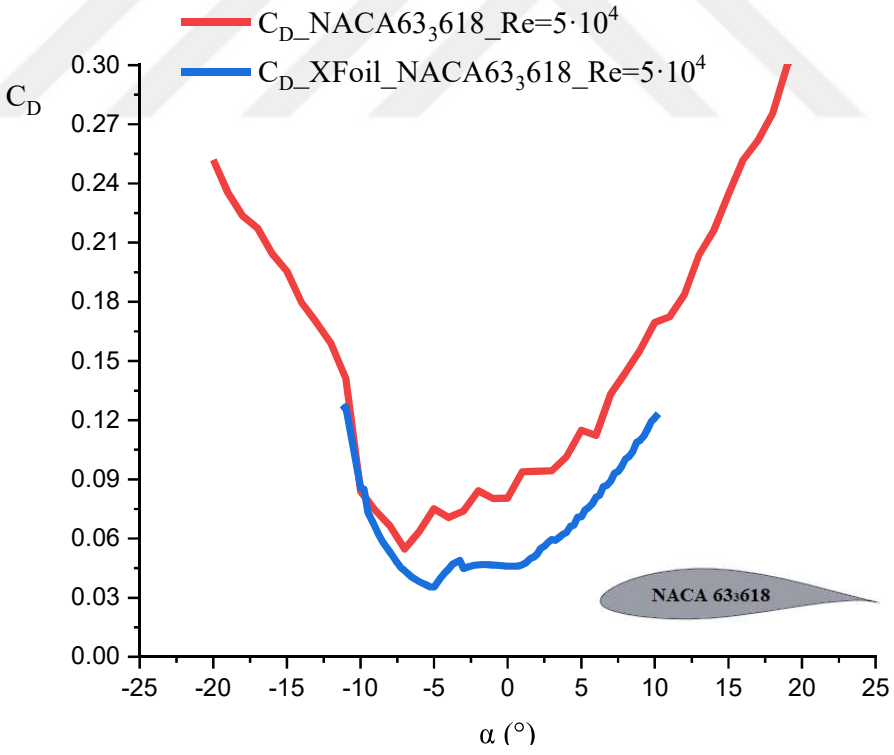

Figure 5.20. Drag curves for NACA 63$_3$618 at Re = 5·10^4

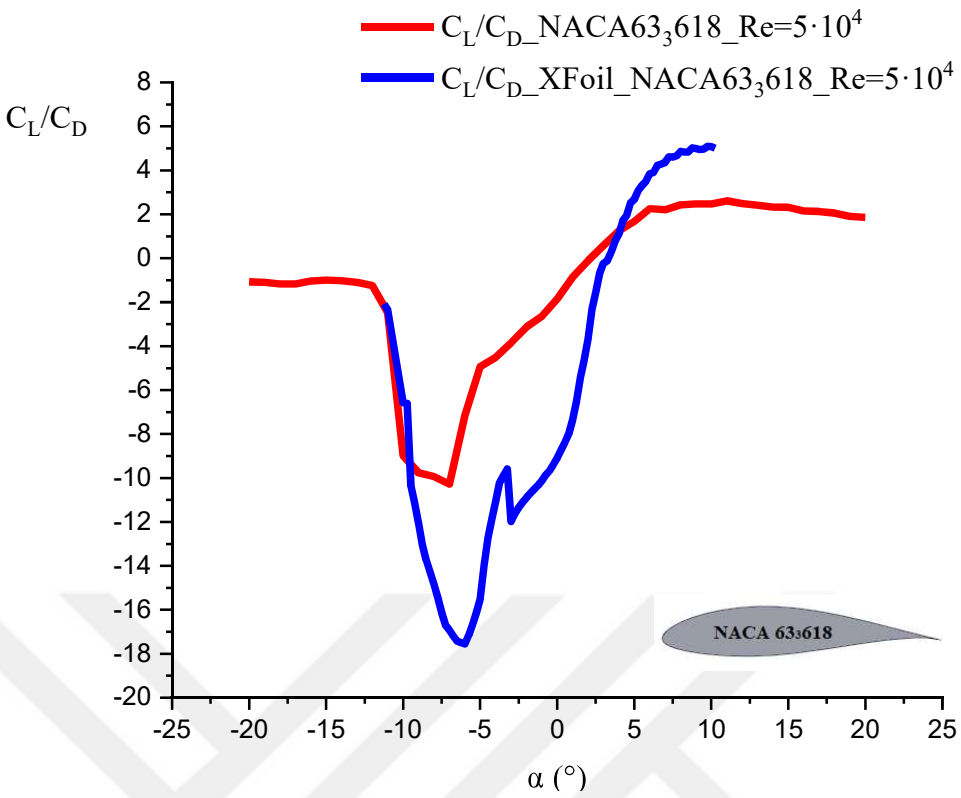

Figure 5.21. Lift to drag ratio curves for NACA 63_3618 at Re = $5 \cdot 10^4$

According to Figures 5.22, 5.23, and 5.24, NACA 63_3618 for Reynolds number of $1 \cdot 10^5$ reaches its maximum lift coefficient value of 1.14 at angle of attack 15°. The maximum lift to drag ratio of 6.7 occured at angle of attack 10°. From the theoretical results the maximum lift is 1.42 at angle of attck 17° whereas the lift to drag ratio is 41.6 at the angle of attack 10°.

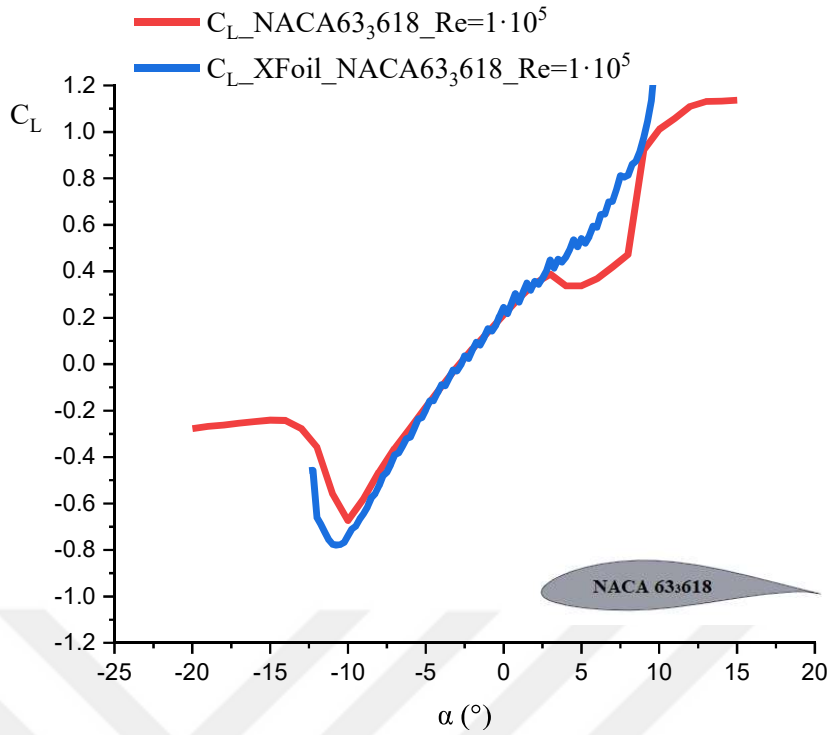

Figure 5.22. Lift curves for NACA 63$_3$618 at Re = 1·10^5

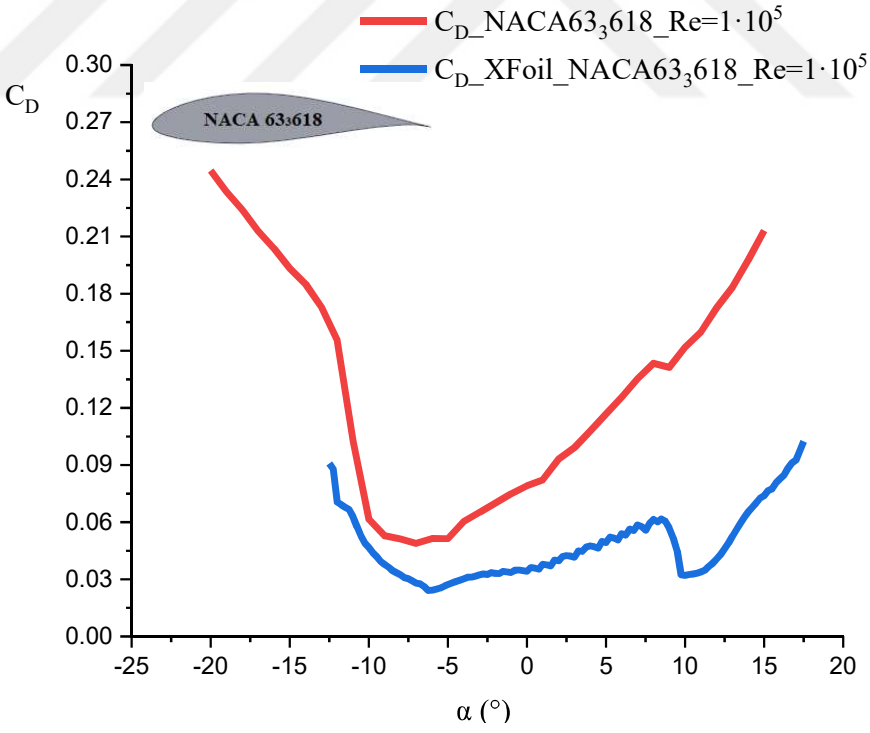

Figure 5.23. Drag curves for NACA 63$_3$618 at Re = 1·10^5

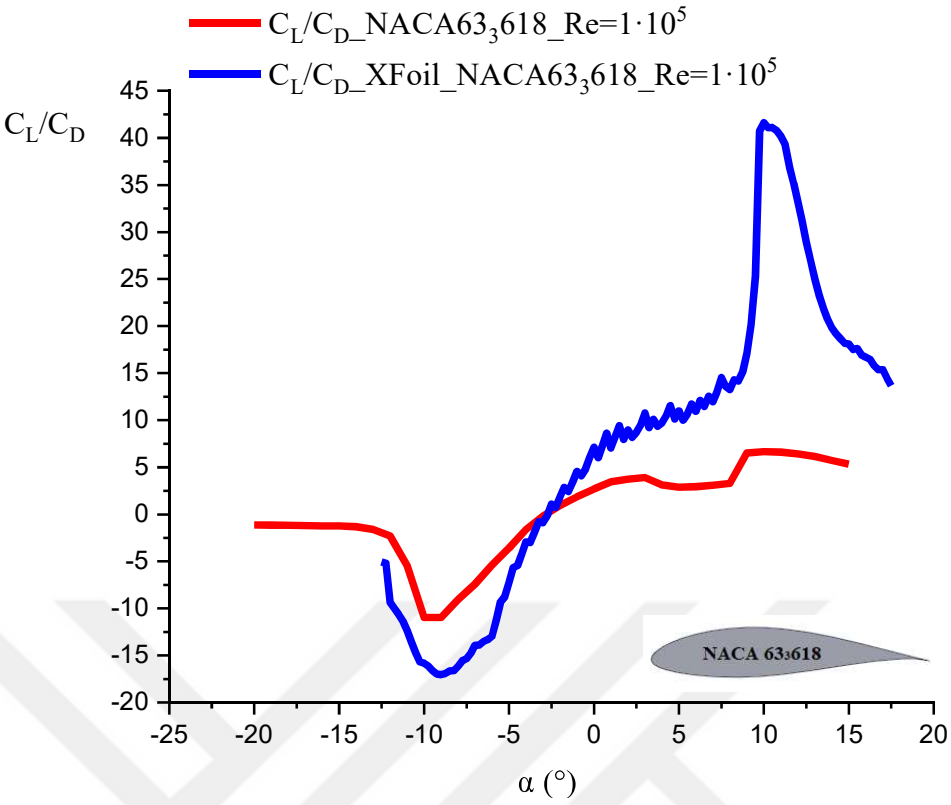

Figure 5.24. Lift to drag ratio curves for NACA 63$_3$618 at Re = 1·10^5

According to the results obtained in the wind tunnel for two Reynolds numbers 5·10^4 and 1·10^5 it is concluded that S822 airfoil model from NREL Airfoil family has shown advantages in both Reynolds numbers compared to other models having the highest lift to drag ratios and maximum lift values for lower angles of attack. Also, as the airfoil model occupies a space in the wind tunnel test section, tunnel data obtained were corrected as described in subchapter 4.2.4.

The experimental results for lift coefficient has a good agreement with the theoretical results. But, regarding to drag coefficient there are some deviations from the theoretical results. The small aspect ratio of airfoil test model and interference drag between the airfoil and the end plates may affects the two-dimensionality of flow. Therefore these are some of the reasons of differences between the experimental and theoretical drag coefficient results.

CHAPTER VI

EXPERIMENTAL RESULTS FOR WIND TURBINE TESTING AND COMMENTS

6.1 Wind Turbine Experimental Test Results

As is described in subchapter 4.3.4, at the beginning of the experimental testing, three pre-experimental methods were made and performed in order to define the system functionality and its best effectiveness under the given flow conditions.

6.1.1 Pre-experimental testing results

6.1.1.1 Determination of average power coefficient curve

The following graphs from Figures 6.1 through 6.3 depicts the averaged power coefficient curves drawn from the values obtained from the three experimental measurement cycles according to the third testing method where the relative velocity is constant while the rpm of the rotor shaft and free stream velocity are variable. As shown in Figure 6.1, the experimental torque and rpm values were recorded three times in each measurement point through a digital camera for each cycle of measurements and an averaged value was obtained.

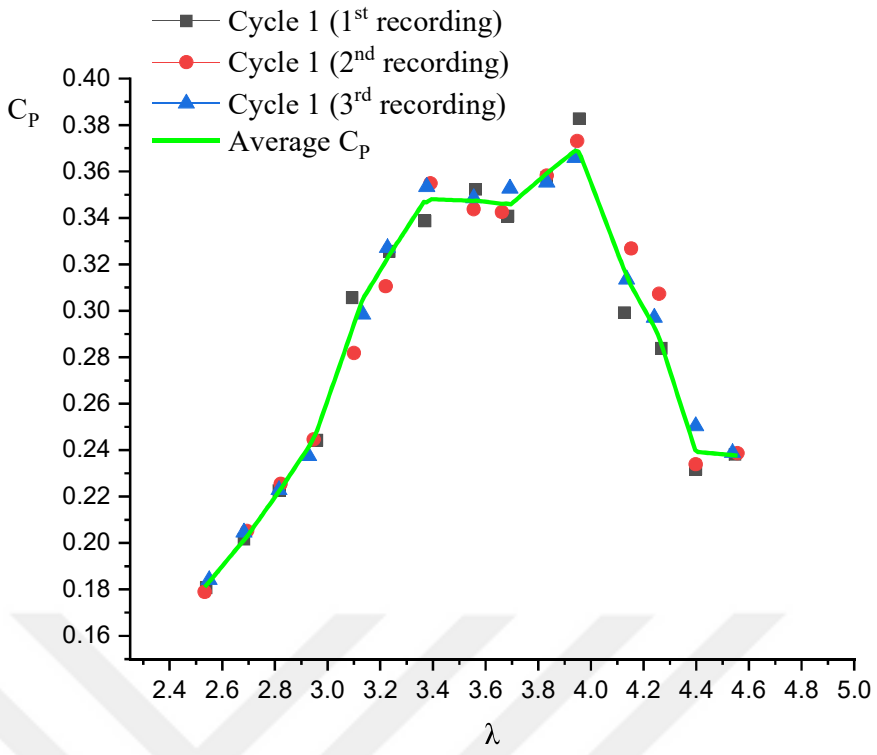

Figure 6.1. Power coefficient curve drawn from the values obtained from the first cycle of experimental measurement

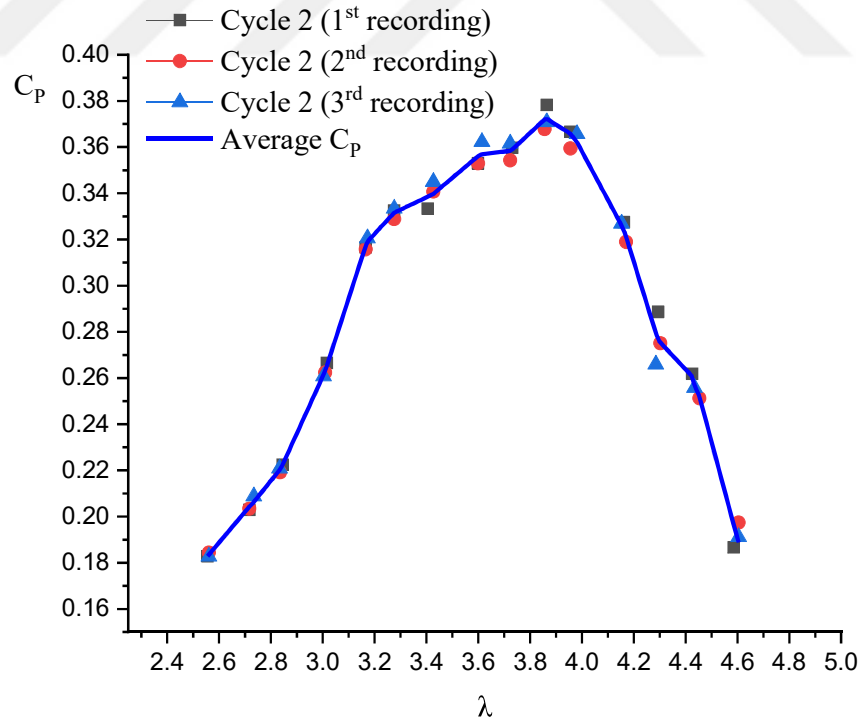

Figure 6.2. Power coefficient curve drawn from the values obtained from the second cycle of experimental measurement

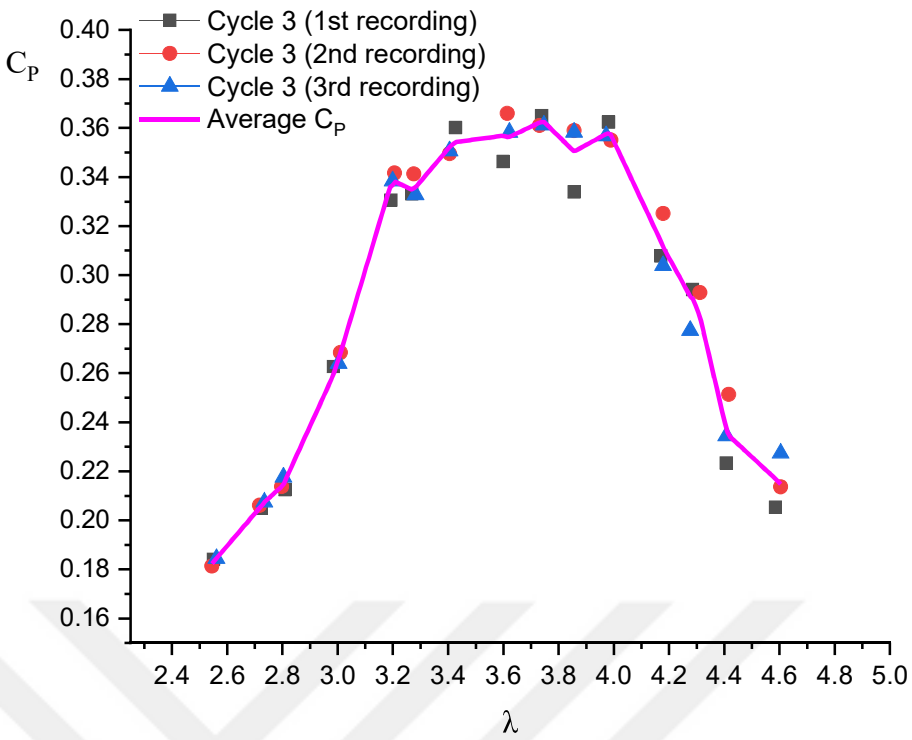

Figure 6.3. Power coefficient curve drawn from the values obtained from the third cycle of experimental measurement

Figure 6.4 shows the averaged power coefficient curves for the three measurement cycles. In this study, the power coefficient curves for each blade models was obtained from the averaged values of the three averaged cycle curves as seen in Figure 6.5. Also, the average power coefficient curve along with the smooth power coefficient curve are presented here.

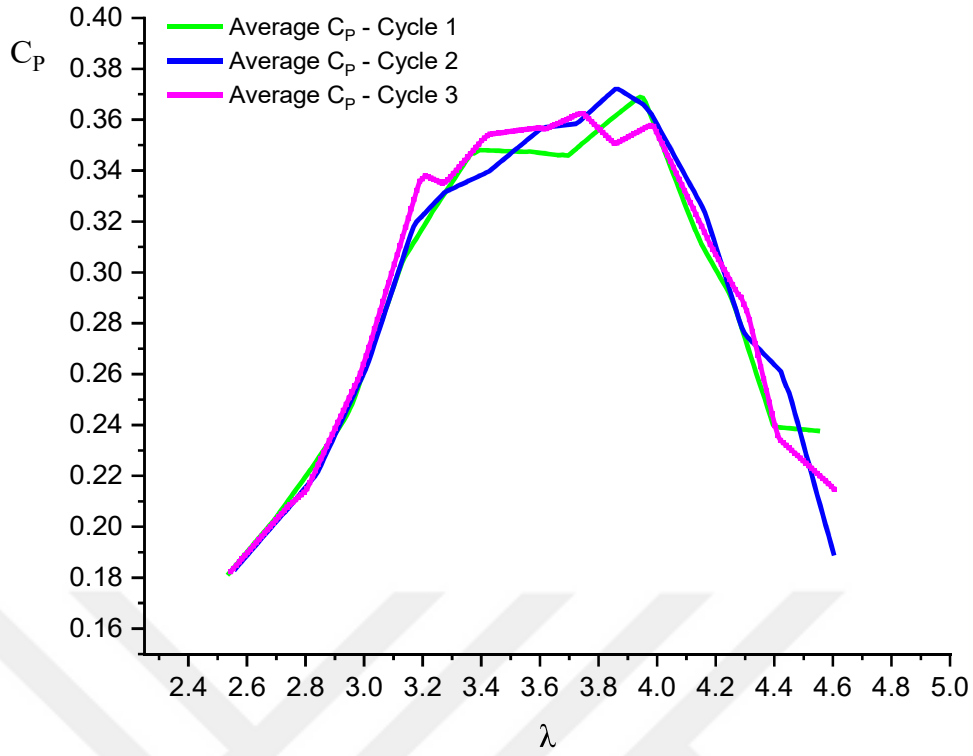

Figure 6.4. Averaged power coefficient curves of the three measurement cycles

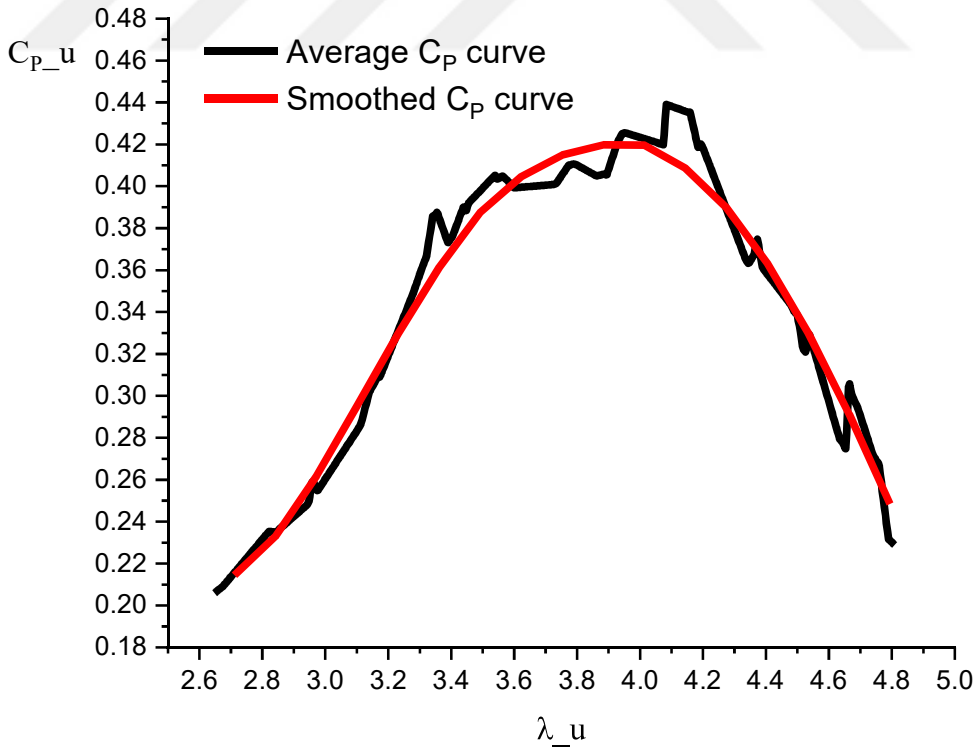

Figure 6.5. Average of the three cycles and smoothed power coefficient curves

The smoothed curve type represented in Figures 6.5 and 6.6 were used as a base model curve to introduce all the graphs drawn for wind turbine rotor configurations. In the below Figure 6.6, the smoothed power curve for the baseline wind turbine is presented along with the all recorded points taken from the experimental testing cycles. As seen in Figure 6.6, the tip speed ratio affects the stability of the rotor blade. In the case of small tip speed ratio values, all nine measurement points were obtained with a small deviation, but with the increase of tip speed ratio, the instability of measured values is also increased.

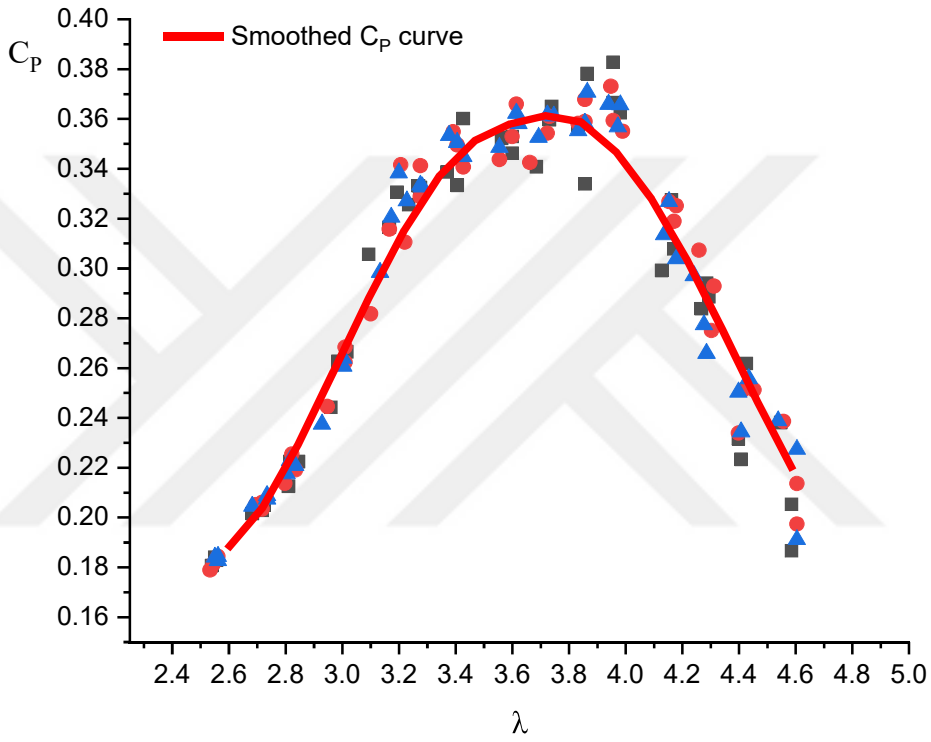

Figure 6.6. Smoothed power coefficient curve with measurement points

The following graph (Figure 6.7) represents the three testing methods performed in the wind tunnel which then were used to adopt the most convenient approach for the aerodynamic analysis of the wind turbine rotors under the given flow conditions.

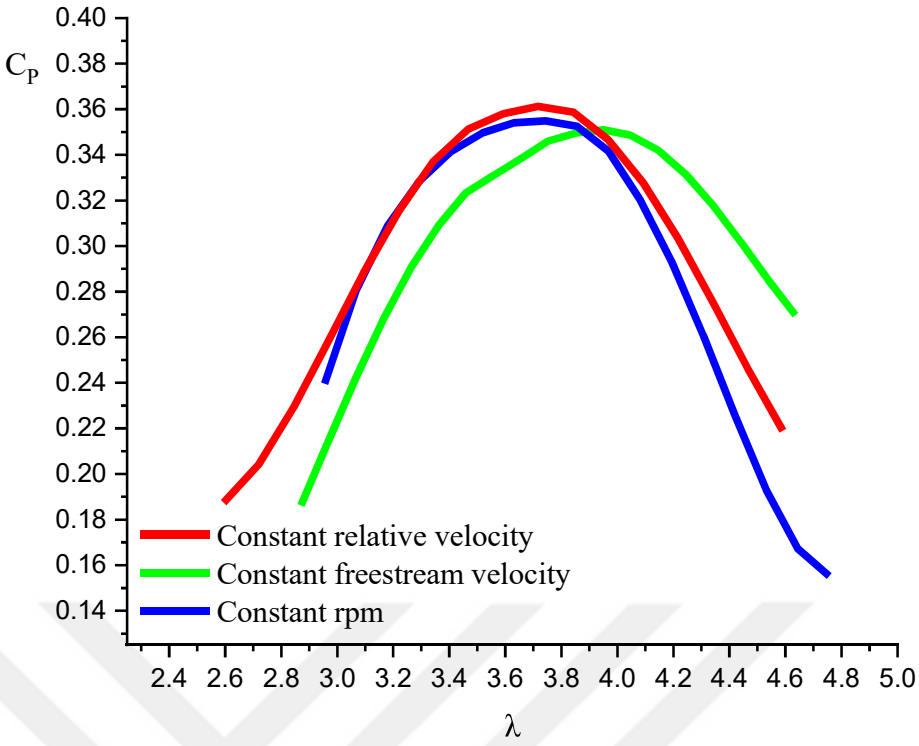

Figure 6.7. Power curves for the three testing methods: constant free stream velocity-variable rpm, constant rpm-variable free stream velocity, and constant relative velocity-variable rpm

In this study, as is described in sub-subchapter 4.3.4, the most convenient approach is selected to conduct the experimental study under constant tip chord-based Reynolds number. This means maintaining the relative velocity constant at the tip of the blade under variable tip speed ratios between 2 and 5. In the case of other two methods, the blade is exposed to variable relative velocities which consequently affect the Reynolds number.

6.1.1.2 Wind tunnel blockage corrections

As the turbine rotor occupies considerable space in the wind tunnel test section, it was necessary to apply blockage corrections due to the influence of the tunnel walls and other interferences in the flow structure. In Figure 6.8, two power coefficient curves for the rotor model M1 are introduced to represent the effect blockage. As seen here, for low tip speed ratios the effect of blockage ratio is minor.

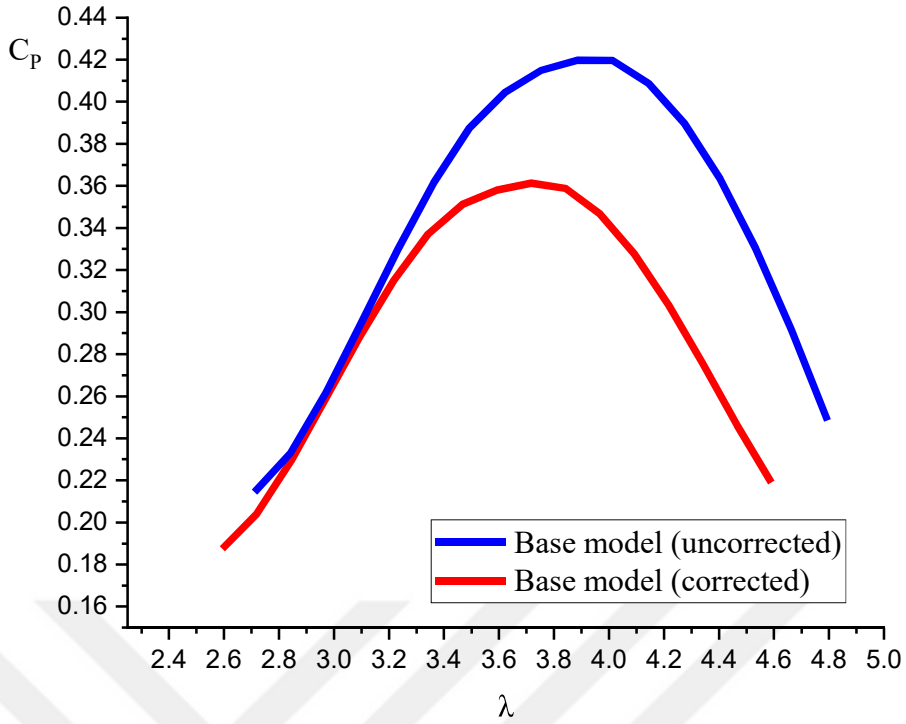

Figure 6.8. Power curves corrected for wind tunnel blockage

Meanwhile, in the following graphs eleven fixed-pitch small scaled rotor models were tested according to the third testing method in an open-circuit wind tunnel with closed test section under constant blade tip relative velocity of 43.29 m/s while varying the free stream velocity from 9 to 15.5 m/s. Ten rotor models have variable amplitude, wavelength, step location, step size, and step depth along the leading edge and upper surface respectively.

6.1.2 M1 rotor model experimental results

In Figure 6.9, the power coefficient of the base model M1 is presented. The shape of the curve of this model indicate an optimum value of the power coefficient between $\lambda = 3.29$ and $\lambda = 3.96$. The maximum power coefficient of 0.361 is at $\lambda = 3.717$.

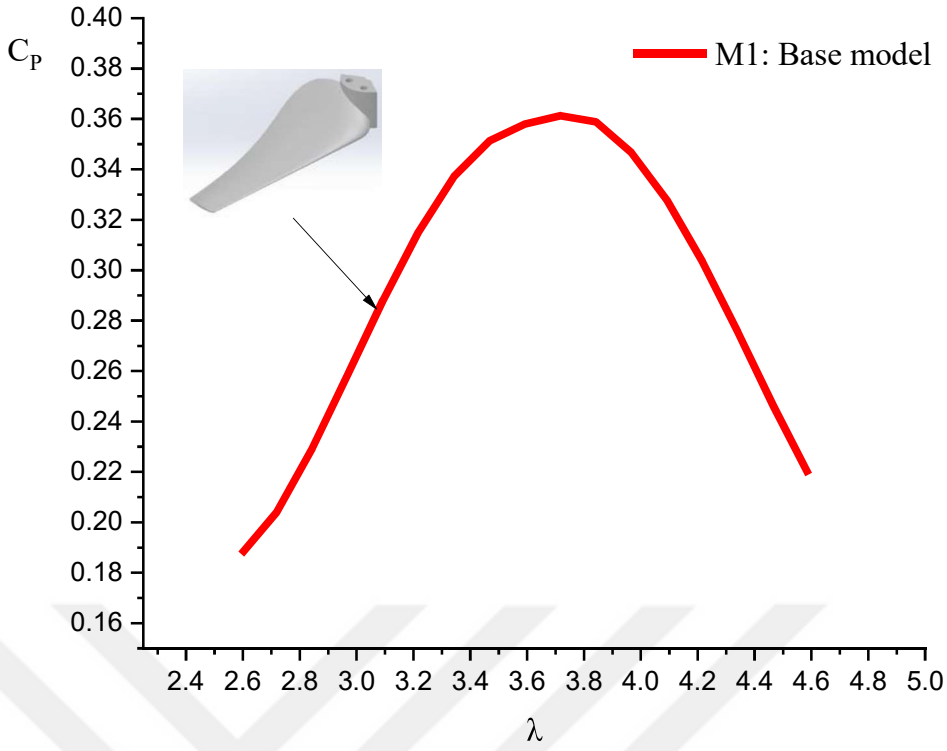

Figure 6.9. Power coefficient versus tip speed ratio for M1 rotor model

6.1.3 M2 rotor model experimental results

In Figure 6.10, the power coefficient curves of M1 and M2 (A1λ3.5) rotor model were depicted. According to the graph, M2 rotor model has the optimum value between $\lambda = 3.5$ and $\lambda = 4$, while the maximum power coefficient of 0.371 at $\lambda = 3.654$. Moreover, this model has a power coefficient of approximately 2.8% higher than the base model and also maintains this advantage over a wider range of tip speed ratios.

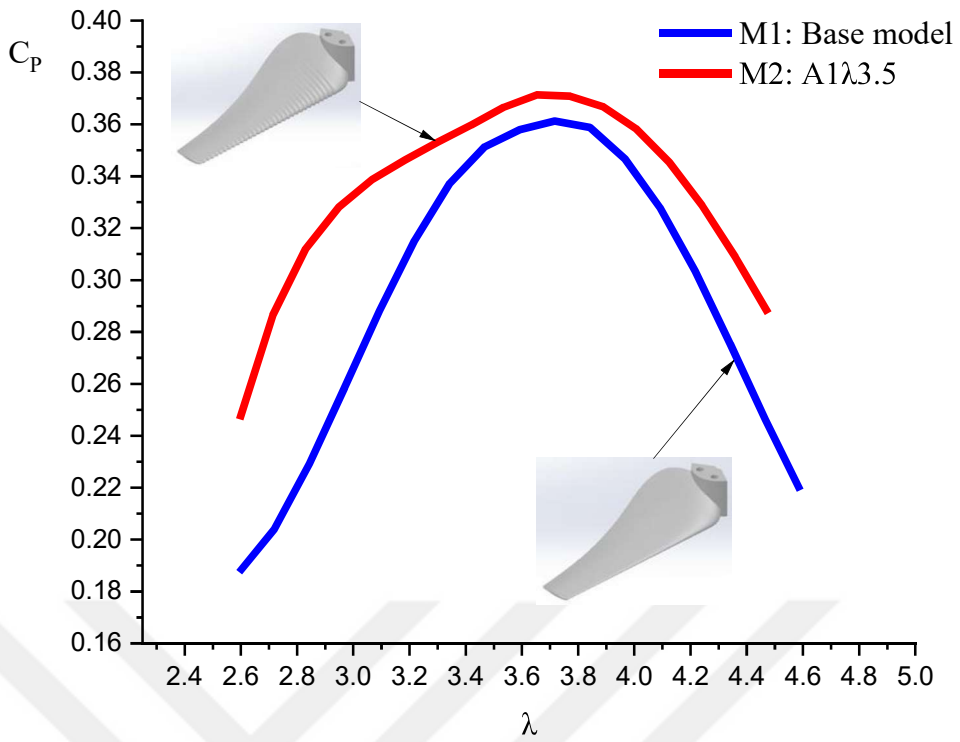

Figure 6.10. Power coefficient versus tip speed ratio for M2 rotor model

6.1.4 M3 rotor model experimental results

Figure 6.11 introduce the power coefficient curves of M1 and M3 (A2λ5) rotor models. The optimum power coefficient for this rotor is found betwen λ = 3.22 and 3.71. The maximum power coefficient of 0.352 is found at λ = 3.46. The graphic below shows that this model has a lower power coefficient compared to the base model and especially in a certain region of tip speed ratios between 3.46 and 4.1.

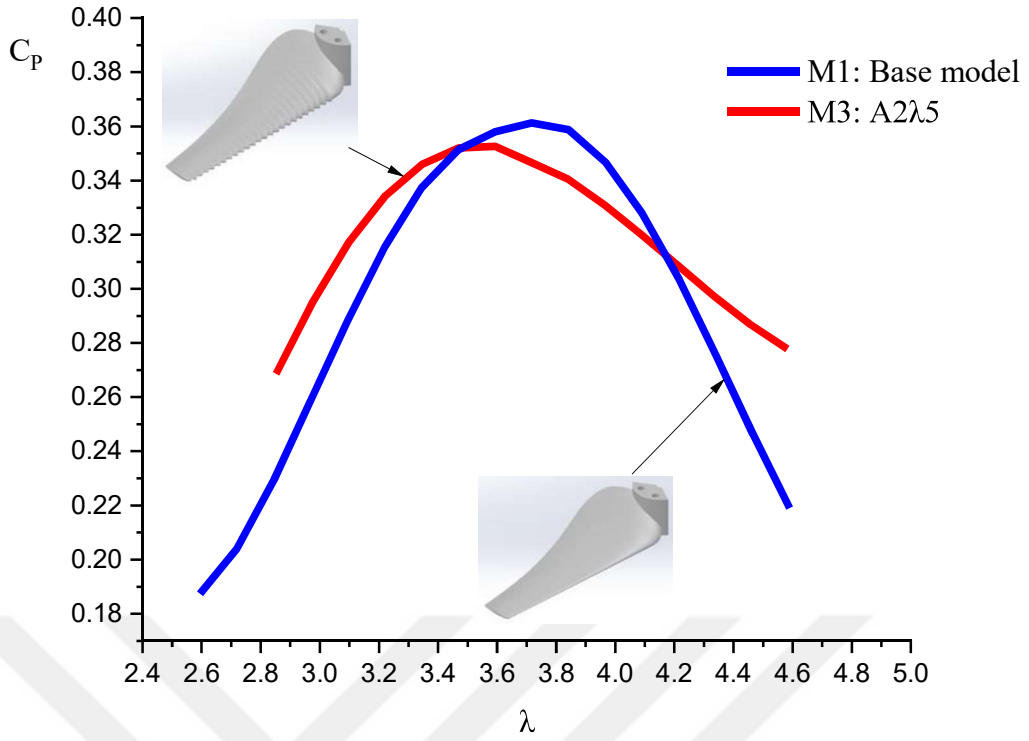

Figure 6.11. Power coefficient versus tip speed ratio for M3 rotor model

6.1.5 M4 rotor model experimental results

The power coefficient curves for the M1 and M4 (A3λ7) rotor model were presented. The shape of M4 and M1 power coefficient curves are almost similar at λ up to 3.15 and with a slight difference beyond 4.21. The optimum power coefficient for M4 lies between λ = 3.22 and λ = 4.06. The maximum power coefficient of 0.331 was obtained for λ = 3.465 (Figure 6.12).

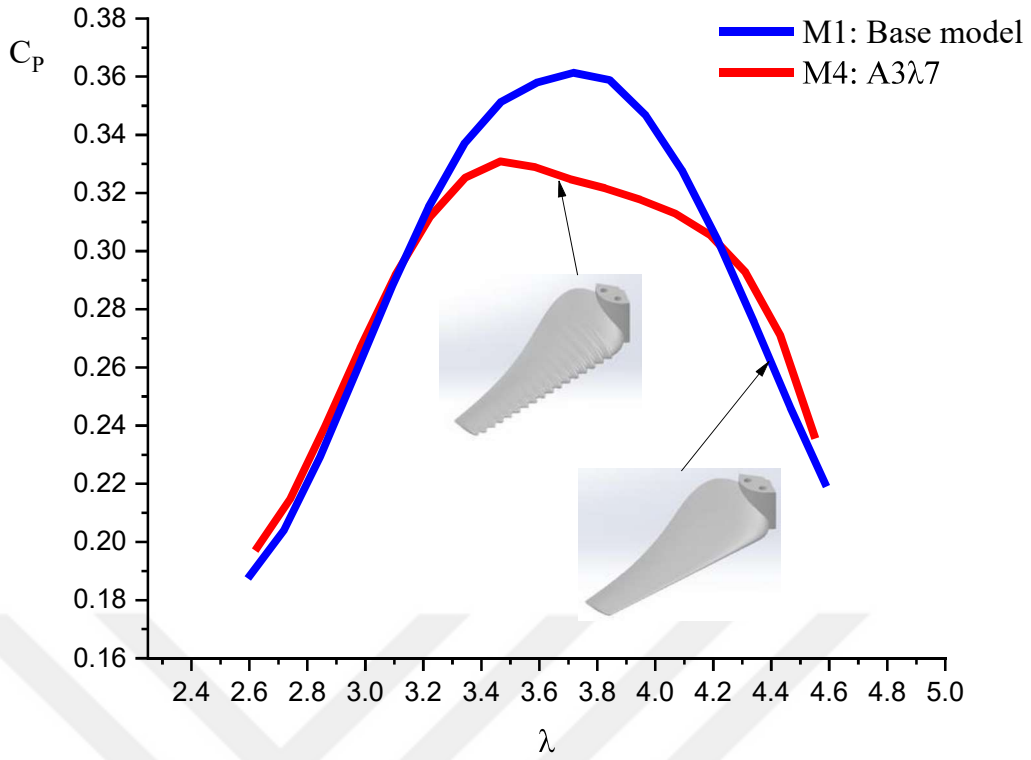

Figure 6.12. Power coefficient versus tip speed ratio for M4 rotor model

6.1.6 M5 rotor model experimental results

In Figure 6.13, the power coefficient for the M5 (A4λ9) and M1 rotor models were presented. The graphic below shows that M5 model has a poor performance compared to the base model up to tip speed ratio of 4.35, but beyond this point a slight increase is noticed.The optimum power coefficient for this rotor is between $\lambda = 3.43$ and $\lambda = 3.92$, whereas the maximum power coefficient of 0.321 was found for $\lambda = 3.679$.

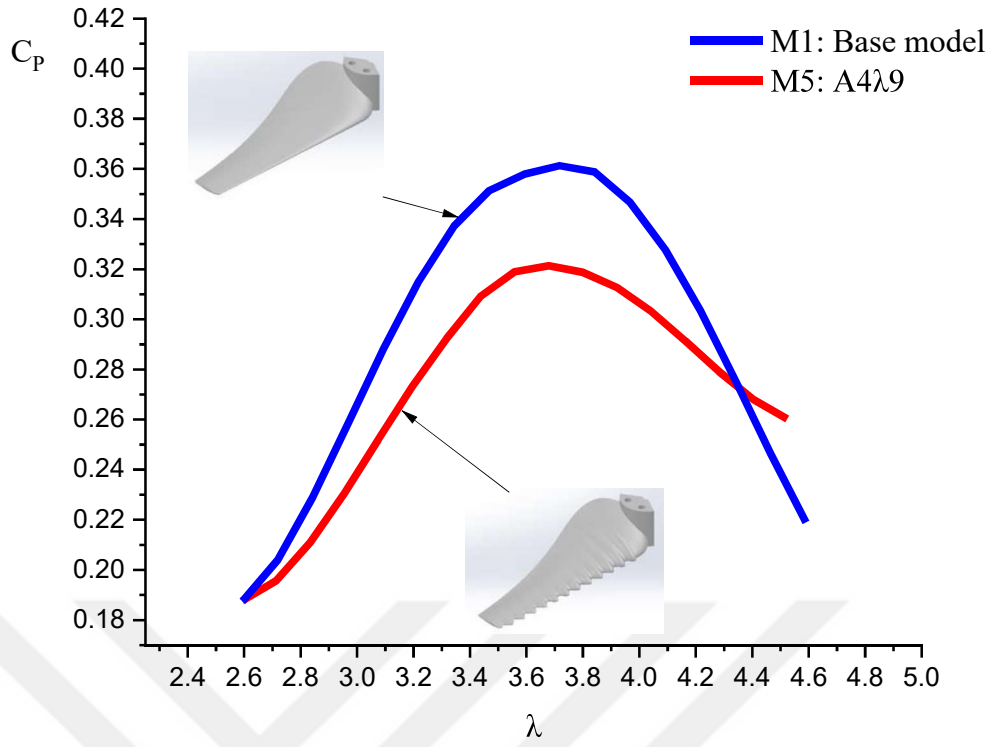

Figure 6.13. Power coefficient versus tip speed ratio for M5 rotor model

6.1.7 M6 rotor model experimental results

As shown in Figure 6.14, M6 (A5λ14) has not indicated any progress throughout the investigated region of tip speed ratios compared to M1 model. The maximum power coefficient for this rotor is around 0.299 at $\lambda = 3.813$.

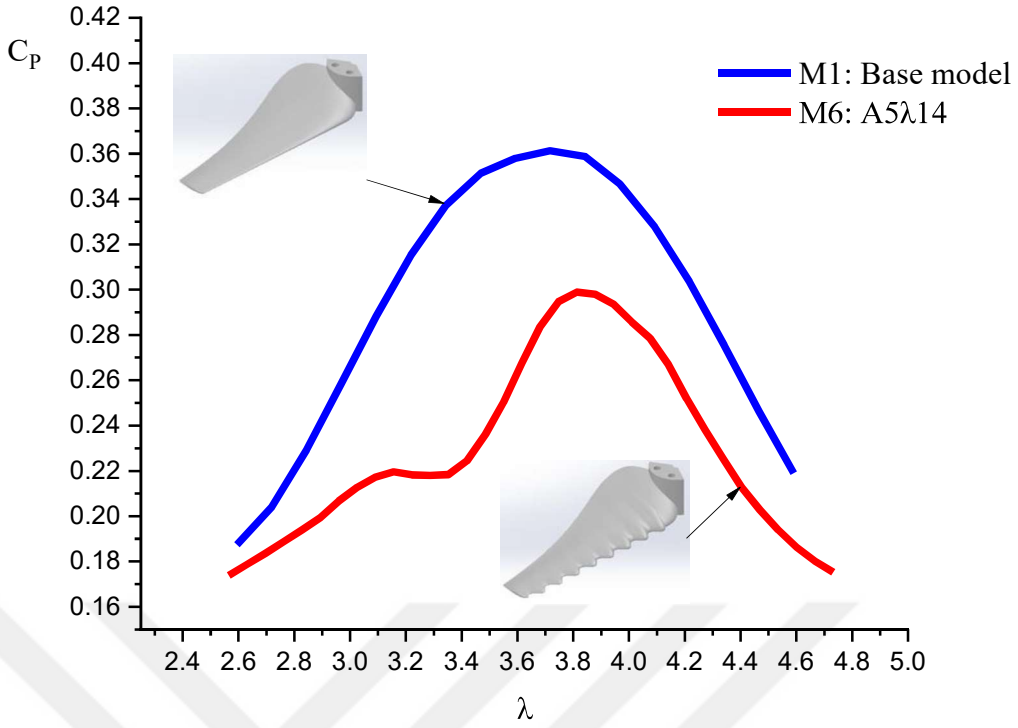

Figure 6.14. Power coefficient versus tip speed ratio for M6 rotor model

6.1.8 M7 rotor model experimental results

In Figure 6.15, the power coefficient curve for M7 (X30cL10cD20t) and M1 rotor model were introduced. M7 model has shown higher performance for lower tip speed ratios espacially up to 3.76 and beyond 4.38 a slight increase is indicated. In the region between 3.76 and 4.38 a little advantage of the base model is noticed. The maximum power coefficient of 0.366 is obtained for $\lambda = 3.644$. Based on the results, M7 has overcome the base model M1 specifically for lower tip speed ratios.

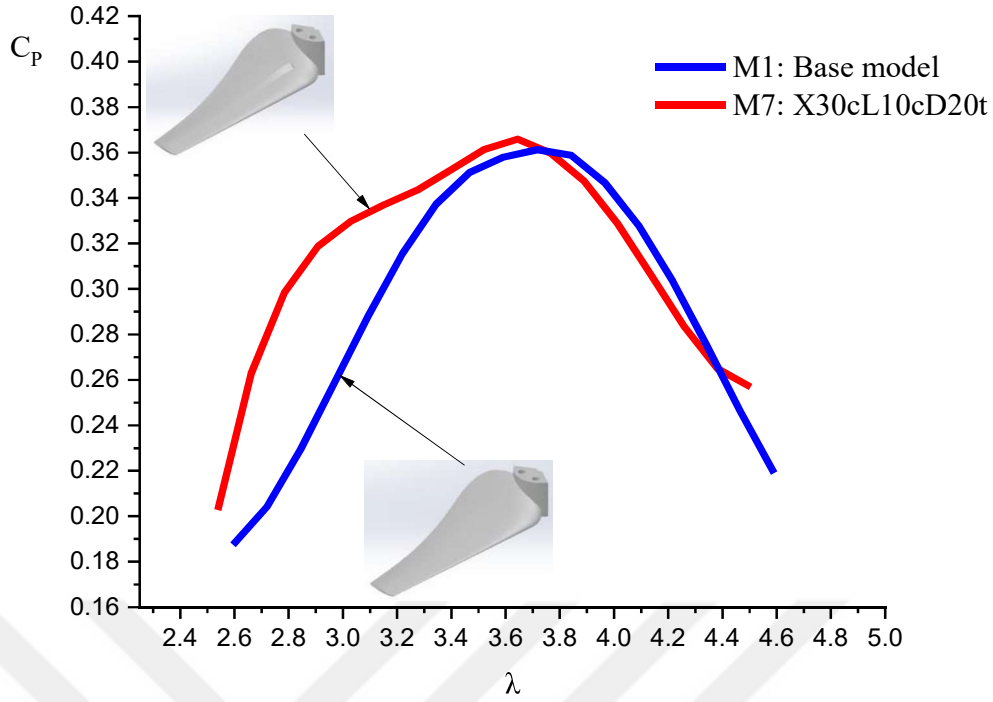

Figure 6.15. Power coefficient versus tip speed ratio for M7 rotor model

6.1.9 M8 rotor model experimental results

Figure 6.16, represents the power coefficient curves for M8 (X40cL20cD35t) rotor model and M1 base model. It is worth mentioning that for lower tip speed ratios, this model has shown a better performance compared to base model M1, especially lower than 3.15. The optimum power coefficient for this rotor was found between $\lambda = 2.59$ and $\lambda = 3.36$, while the maximum power coefficient of 0.32 was obtained for $\lambda = 2.849$.

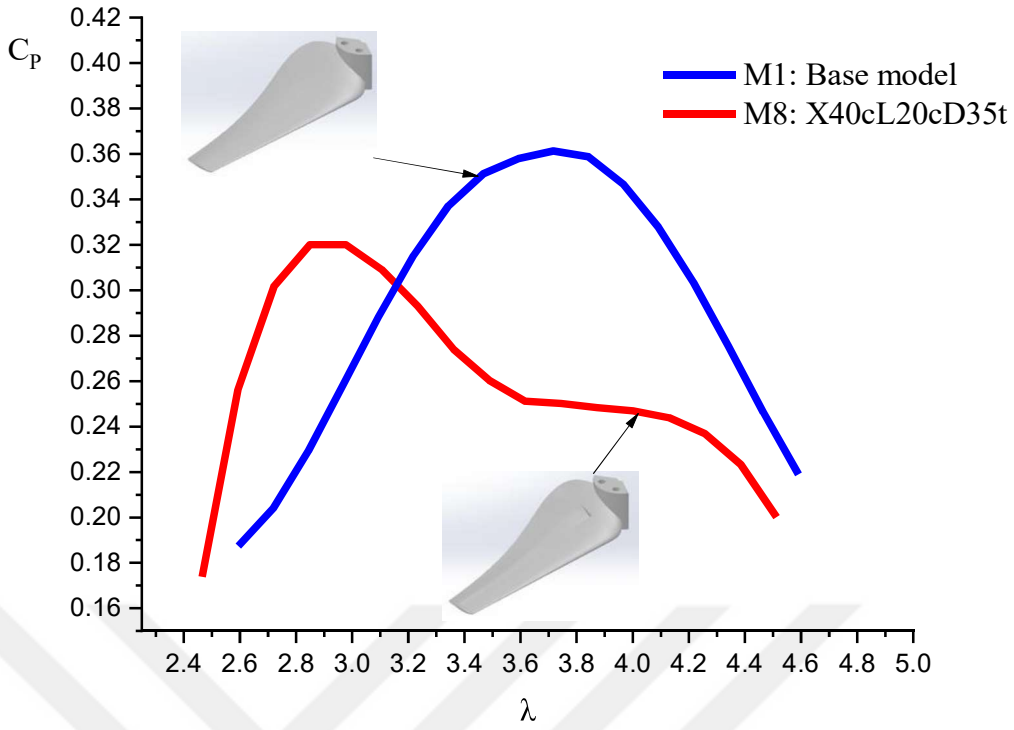

Figure 6.16. Power coefficient versus tip speed ratio for M8 rotor model

6.1.10 M9 rotor model experimental results

In Figure 6.17, the power coefficient curves for M1 and M9 (X50cL25cD19t) rotor models were presented. This model same as M8 has shown a better performance only for lower tip speed ratio, especially for lower than 3.22. Meanwhile, the maximum power coefficient for this model is around 0.34 for $\lambda = 2.917$, on the other hand, the optimum power coefficient lies between $\lambda = 2.79$ and $\lambda = 3.27$.

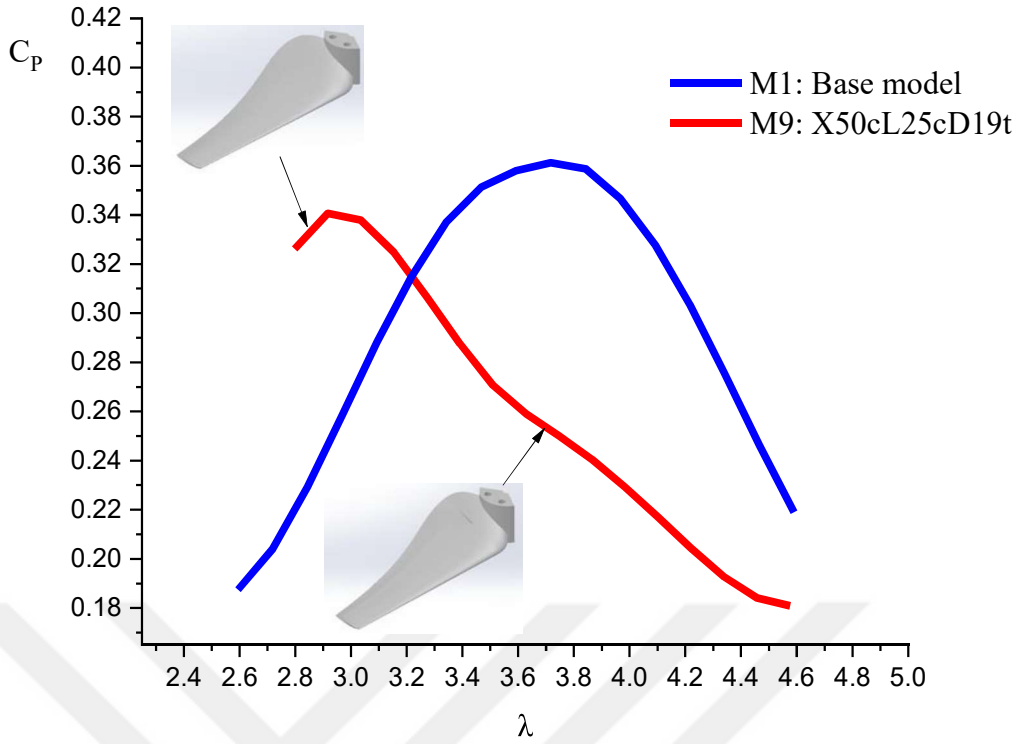

Figure 6.17. Power coefficient versus tip speed ratio for M9 rotor model

6.1.11 M10 rotor model experimental results

In Figure 6.18, M10 (X50cL30cD50t) and M1 rotor models were introduced. The optimum power coefficient for the rotor is observed to be between $\lambda = 2.82$ and $\lambda = 3.31$, and the maximum power coefficient of 0.323 for $\lambda = 2.939$. Same as M8 and M9, this model has shown a better performance only for lower tip speed ratio, especially for lower than 3.18.

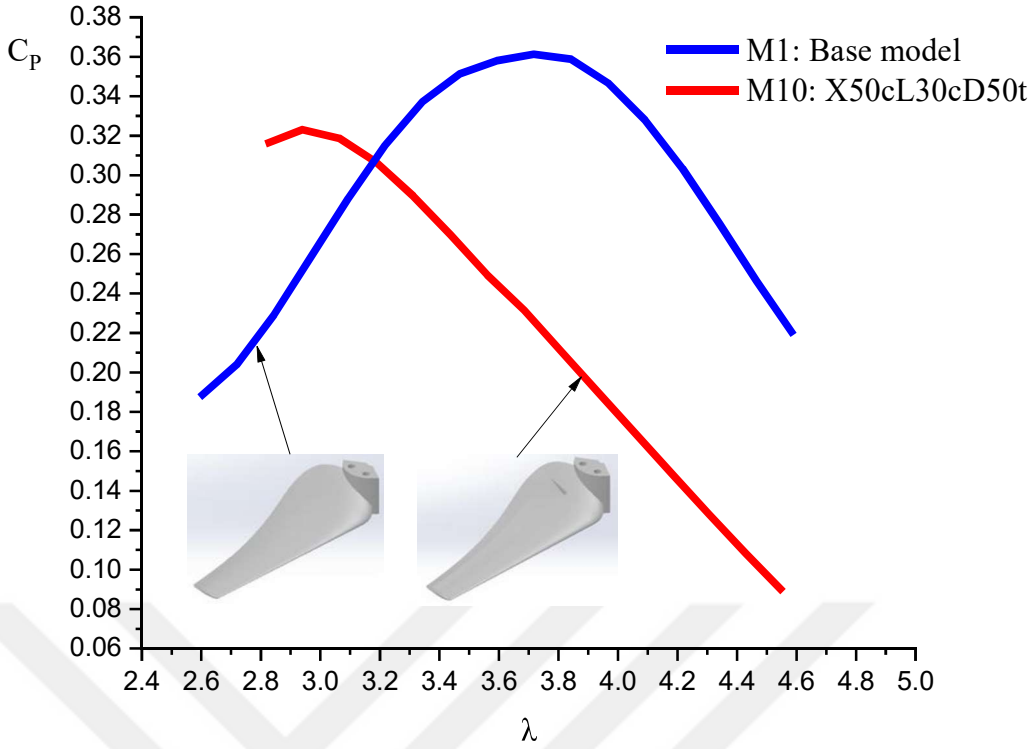

Figure 6.18. Power coefficient versus tip speed ratio for M10 rotor model

6.1.12 M11 rotor model experimental results

The power coefficient curves for M1 and M11 (A2λ7.5-X50cL25cD19t) hybrid rotor model were presented. The optimum power coefficient for this rotor lies between λ = 2.83 and λ = 3.82, whereas the maximum power coefficient is 0.319 at λ = 3.451. Same as M8, M9, and M10, this model has also shown a better performance only for lower tip speed ratio than 3.22.

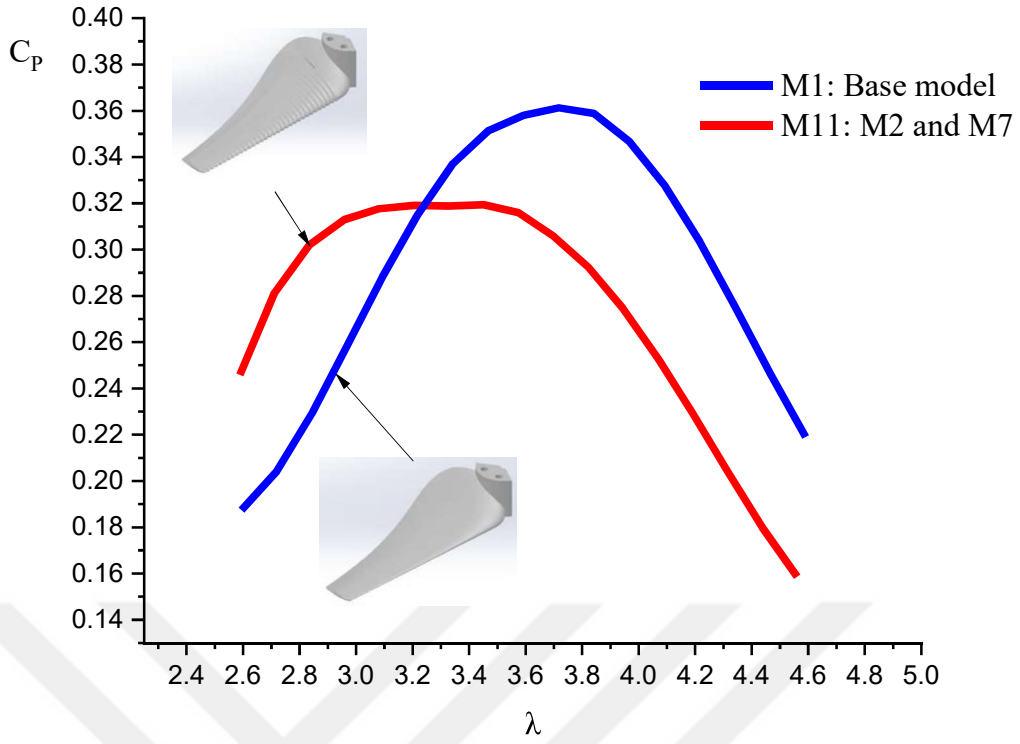

Figure 6.19. Power coefficient versus tip speed ratio for M11 rotor model

6.1.13 Summary of wind turbine power coefficient graphs

Basically, the wind turbine is designed according to some specific input design parameters and normally it is expected to reach the maximum efficiency only at design point. In this study, wind turbine rotors will be subjected to off-design conditions to investigate the performance limits occurring in this working region. The performance level of the wind turbine rotors is defined by the power coefficient curves obtained in the wind tunnel testing at different free stream velocities and tip speed ratios.

At the beginning of the true experimental study, some pre-experimental tests needed to be done to define the proper approach to be followed taking into account existing laboratory conditions along with the rotor effectiveness as is described in subchapter 4.3.4.

Also, knowing the fact that wind turbine rotor occupies a considerable space in the wind tunnel test section, blockage corrections due to the influence of the tunnel walls and other interferences are a necessity to simulate a similar environment between the wind tunnel

and outdoor atmospheric conditions. In this context, Figure 6.8 introduce two power coefficient curves for the rotor model M1 with clean blades to represent the blockages due to the tunnel interferences.

In Figure 6.20, the power coefficients of all rotor configurations were presented. All rotors were tested under the same flow conditions where the aerodynamic performance of each of them was measured experimentally. Each of these curves represents the level of their performance relative to the base model M1.

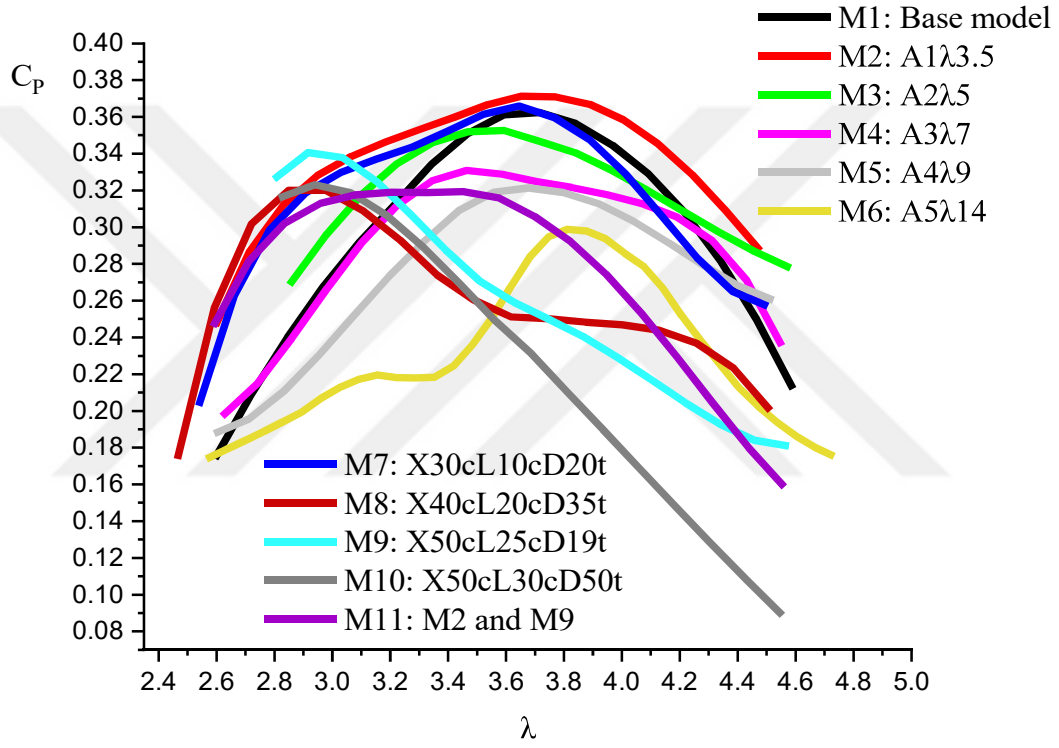

Figure 6.20. Power coefficient curves of all wind turbine rotor configurations

Meanwhile, in the following graph (Figure 6.21), power coefficient curves of M1 rotor model in relation M2, M3 M4, M5, and M6 rotor models with tubercles were presented. As can be seen from the graph below, M2 rotor model has shown advantages in all aspects compared to all models of its group and base model as well. A significant advantage can be observed for the smaller values of tip speed ratios especially below 3.3. However, other models do not have all of these features as M2. In the model M3, a decrease of the maximum power coefficient below the base model is observed in the mid region of the

tip speed ratio values between 3.46 and 4.1. On the other hand, models M4, M5, and M6 have not shown effectiveness, even affecting its reduction.

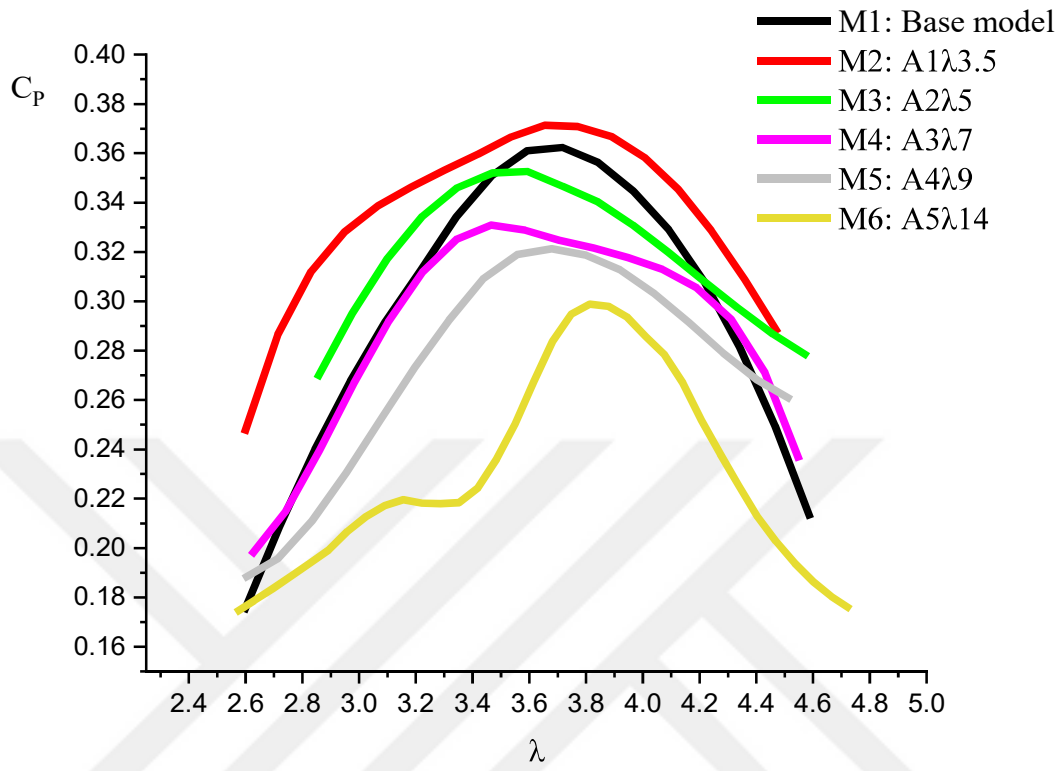

Figure 6.21. Power coefficient curves of M1 rotor model and tubercled rotor configurations

Also, the power coefficient curves of M1 rotor model along with the vortex cavity-backward facing-step blade shapes are depicted in Figure 6.22. As can be seen from the graph below, M7 rotor model has shown advantages compared to all models only in a certain range of tip speed ratios between 3.1 to 3.76. It is noticed that for smaller values of tip speed ratios this model has shown better performance compared to base model and some other models of this group. On the other hand, M8 rotor model has shown effectiveness only for smaller values of tip speed ratios than 3.15. Similar to the M8, other models M9 and M10 have not shown any improvement for larger values of tip speed ratios than 3.18.

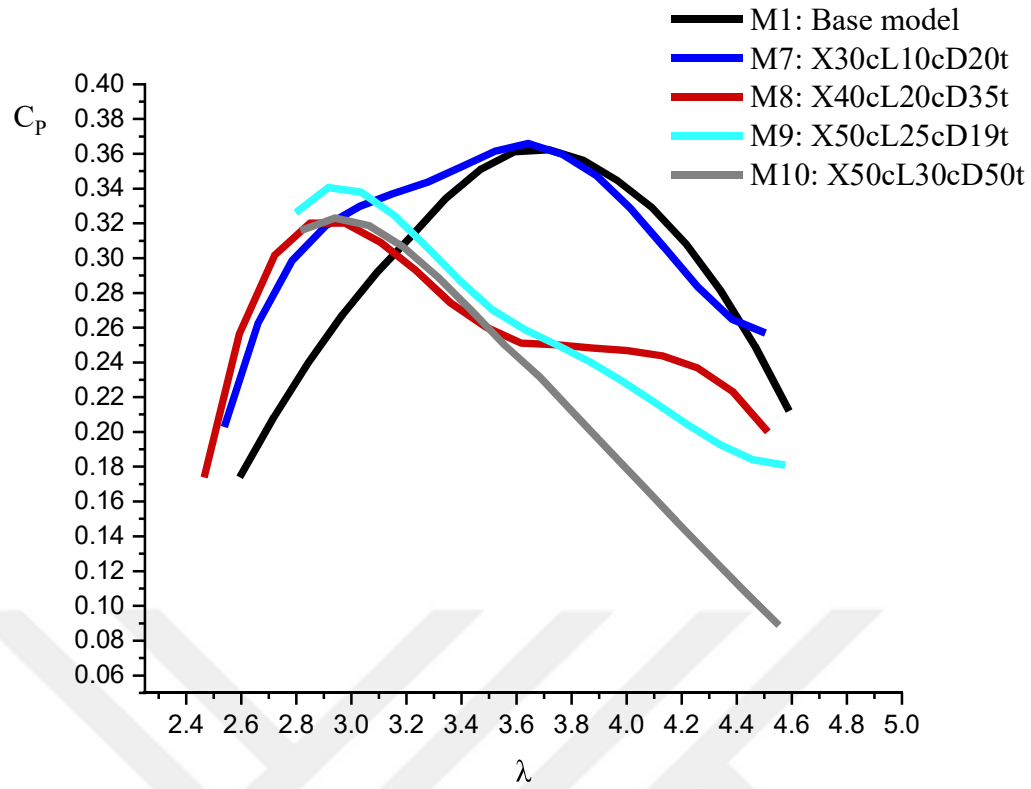

Figure 6.22. Power coefficient curves of M1 rotor model and vortex cavity rotor configurations

In Figure 6.23, the power coefficient curves of M1 rotor model along with the M11 rotor model are presented. The hybrid model M11, a combination of M2 and M9 models, has performed best for smaller values of tip speed ratios than 3.22, however, for larger values its efficiency drops.

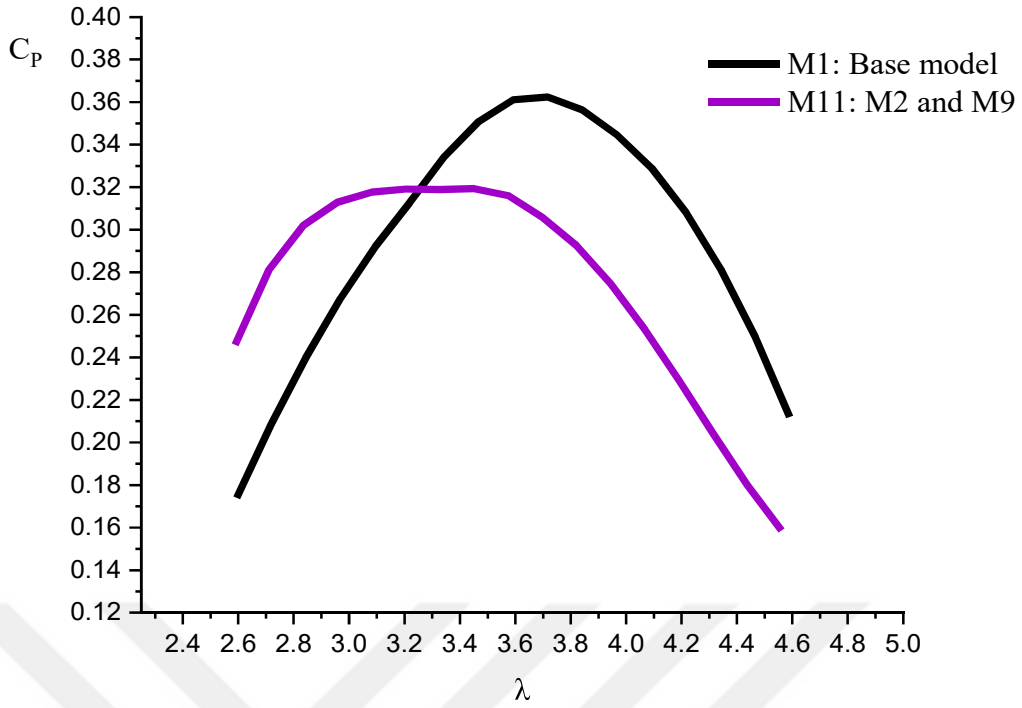

Figure 6.23. Power coefficient curves of M1 rotor model and M11 rotor model

In the next chart, the power coefficient curves of M1 rotor model and rotor models with the best performance shown in laboratory tests are depicted in Figure 6.24. It can be noticed from the graphic that two rotor configurations, M2 and M7, have shown better performance compared to the base model. As can be seen from the figure, the shape of the power coefficient curve of the M2 model is more extended overlapping the M1 power coefficient curve entirely. This means that this configuration with amplitude 1 mm and wave length 3.5 mm has overcome the base model in terms of aerodynamic efficiency in all tip speed ratios. On the other hand, the model M7 has shown also higher power coefficient compared to the base model, however, a slight decrease is noticed in a specific region of tip speed ratios.

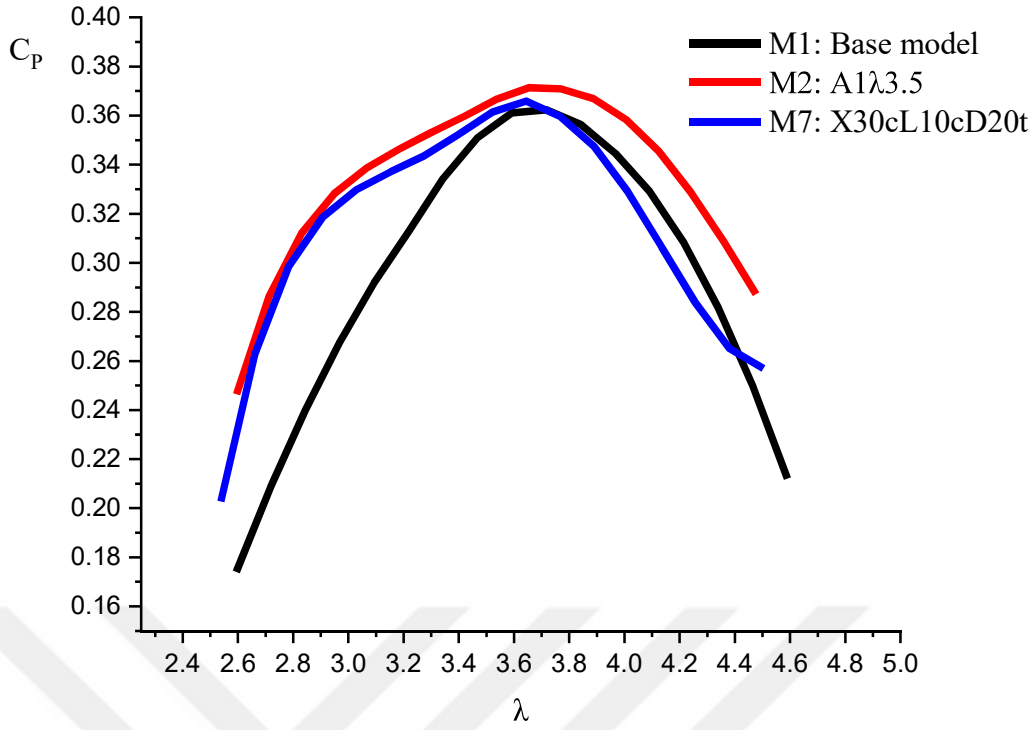

Figure 6.24. Power coefficient curves of M1 rotor model and two most efficient rotor configurations

CHAPTER VII

CONCLUSIONS

This study has investigated experimentally the aerodynamic performance of several small horizontal axis wind turbine blade rotors of different configurations realized based on passive flow control techniques. Leading edge tubercles and vortex cavity (backward facing step) techniques were applied to generate several configurations by changing the airfoil geometry parameters such as leading edge and part of upper surface. NREL S822 airfoil was used to build the entire rotor blade structure from root to tip. In this thesis, five configurations (M2, M3, M4, M5, M6) with tubercles along the leading edge with varying amplitude and wavelength, four others (M7, M8, M9, M10) with vortex cavity applied on the upper surface of the blade with varying step, location, and depth sizes, and one model (M11) by combining the two techniques were generated. A base model without any modification (M1) was tested to make comparisons with the modified models. All experimental results were obtained under stable working conditions.

From the results obtained in the wind tunnel, the following conclusions are drawn;

- Tunnel testing of four airfoil models at two Reynolds numbers: $5 \cdot 10^4$ and $1 \cdot 10^5$, uncovered the NREL S822 airfoil profile as the best section that shown highest performance compared to other airfoil models. The maximum lift coefficient of 1.011 for $Re = 5 \cdot 10^4$ is achieved at angle of attack of 14° while the maximum lift to drag ratio of 15.3 is achieved at angle of attack of 11°. Meanwhile, for $Re = 1 \cdot 10^5$ this section reaches its maximum lift coefficient value of 0.99 at angle of attack 15° and has a maximum lift to drag ratio of 20.1 at angle of attack 9°.
- Preliminary test of the rotor model M1 revealed that maintaining the tip chord relative velocity constant (tip chord-based Reynolds number) while changing the free stream velocity was more effective than other testing methods.
- Applying tunnel corrections to the power coefficient and tip speed ratio of M1 model resulted in a significant decrease of these parameters from $C_P = 0.420$ at $\lambda = 3.883$ to $C_P = 0.362$ at $\lambda = 3.717$.
- Among tubercles applied, model M2 with amplitude 1 mm and wave length 3.5 mm has overcome all rotor models for all values of tip speed ratio analyzed in this

study. Compared to base model M1, M2 model has approximately 2.8% higher power coefficient and also maintains this advantage for a wider range of tip speed ratios.

- On the other hand, the model M7 has shown also higher power coefficient of around 1.1% at tip speed ratio of 3.644 compared to the base model. However, a slight decrease is noticed in a specific region of tip speed ratios, especially between 3.76 and 4.38.
- The hybrid model M11, a combination of M2 and M9 models, has performed better than base model M1 for smaller values of tip speed ratios than 3.22, however, for larger values its efficiency drops significantly.
- Other models such as M3, M8, M9, M10, and M11, have shown their effectiveness specifically for smaller values of tip speed ratio up to around 3.5 compared to the base model.

In summary, these two passive flow control techniques have shown their effectiveness in improving the aerodynamic efficiency of the wind turbine rotor under certain conditions. Referring to the M2 rotor model, it can be concluded that the effect of amplitude and wavelength are significant in increasing the rotor performance level when their values are smaller. Whereas, with the increase of these values, the rotor efficiency decreases almost gradually but maintaining in some way the shape of the curve.

Also, it is observed that the effect of the vortex cavity is maximum mainly when its location is close to the leading edge and the size is very small compared to other configurations. An increase in these two parameters results in a displacement of the peaks of the curves toward smaller tip speed ratio values. On the other hand, the effect of step depth seems to be minor, where M7 rotor model has a smaller step location and size but almost equal step depth compared to M9.

REFERENCES

Abate, G., Mavris, D.N. and Sankar, L.N., "Performance effects of leading edge tubercles on the NREL Phase VI wind turbine blade", ***Journal of Energy Resources Technology*** 141 (5), 9, 2019.

Abbott, I.H. and Von Doenhoff, A.E., Theory of Wing Sections: Including a Summary of Airfoil data, ***Dover Publications***, New York, 1959.

Adachi, J., Kurosaki, K., Uno, M. and Yamanaka, S., "Mimicking the humpback whale: An aerodynamic perspective", ***Progress in Aerospace Sciences*** 84, 48-49, 2016.

Aftab, S.M.A. and Ahmad, K.A., "CFD study on NACA 4415 airfoil implementing spherical and sinusoidal Tubercle Leading Edge", ***Plos One*** 12 (11), 2017.

Ahrens, C.D., Meteorology Today: An Introduction to Weather, Climate, and the Environment, 9th ed., ***Brooks/Cole Publishing***, Belmont, 2009,

Akbıyık, H., Control of flow around a circular cylinder by using active and passive control methods, Master Thesis, ***NÖHU Graduate School of Natural and Applied Sciences***, Niğde, p.53-59, 2014.

Akour, S.N., Al-Heymari, M., Ahmed, T. and Khalil, K.A., "Experimental and theoretical investigation of micro wind turbine for low wind speed regions", ***Renewable Energy*** 2018.

Al-Bahadly, I.H., Wind Turbines, ***IntechOpen***, Rijeka, 2011.

Amano, R.S. and Sundén, B., Aerodynamics of Wind Turbines: Emerging Topics, ***Wit Press***, Southampton, 2014,

Ananda, G.K., Bansal, S. and Selig, M.S., "Subscale testing of horizontal-axis wind

turbines", ***35th AIAA Applied Aerodynamics Conference***, Denver, Colorado, 5-9 June, 2017.

Anant Kishore, R. and Priya, S., "Design and experimental verification of a high efficiency small wind energy portable turbine (SWEPT)", ***Journal of Wind Engineering Industrial Aerodynamics*** 118, 12-19, 2013.

Anderson, C., Wind Turbines: Theory and Practice, ***Cambridge University Press,*** Cambridge, 2020.

Anderson, J.D., Fundamentals of Aerodynamics SI, 5th int. ed., ***McGraw Hill***, New York, 2011.

Arbogast, A.F., Discovering Physical Geography, 3th ed., ***Wiley***, New York, 2013.

Bakırcı, M. and Yılmaz, S., "Theoretical and computational investigations of the optimal tip-speed ratio of horizontal-axis wind turbines", ***Engineering Science and Technology, an International Journal*** 21 (6), 1128-1142, 2018.

Barry, R.G. and Chorley, R.J., Atmosphere, Weather and Climate, 8th ed., ***Routledge***, London & New York, 2003.

Bertagnolio, F. and Sorensen, N., "Wind turbine airfoil catalogue", *Risø-R-1280 (EN),* ***Risø National Laboratory***, Roskilde, 2001.

Bertin, J.J. and Cummings, R.M., Aerodynamics for Engineers, 6th ed., ***Pearson Education Limited***, London, 2013.

Bharatdway, K., Physical Geography: Atmosphere, ***Disvovery Publishing House***, New Delhi, 2006.

Bjorck, A., "Coordinates and Calculations for the FFA-Wl-xxx, FFA-W2-xxx, FFA-W2-xxx and FFA-W3-xxx Series of Airfoils for Horizontal Axis Wind Turbines", ***FFA TN 1990-15***, Stockholm, 1990.

Bolzon, M.D., Kelso, R.M. and Arjomandi, M., "The effects of tubercles on swept wing performance at low angles of attack", ***Proceedings of the 19th Australasian Fluid Mechanics Conference***, pp. 1-4, 08-11 December, 2014.

Bolzon, M.D., Kelso, R.M. and Arjomandi, M., "Tubercles and Their Applications", ***Journal of Aerospace Engineering*** 29 (1), 10, 2016.

Boroomand, M. and Hosseinverdi, S., "Numerical investigation of turbulent flow around a stepped airfoil at high Reynolds number", ***Proceedings of ASME Fluids Engineering Division Summer Meeting Conference***, Vail, Colorado, USA, pp. 2-6 August, 2009.

Branlard, E., Wind Turbine Aerodynamics and Vorticity-Based Methods: Fundamentals and Recent Applications, ***Springer International Publishing***, New York, 2017.

Brusca, S., Lanzafame, R. and Messina, M., "Flow similitude laws applied to wind turbines through blade element momentum theory numerical codes", ***International Journal of Energy and Environmental Engineering*** 5 (4), 313-322, 2014.

Burdet, T.A. and Treuren, K.W. Van, "Scaling small-scale wind turbines for wind tunnel testing", ***Proceedings of ASME Turbo Expo: Power for Land, Sea, and Air***, Copenhagen, Denmark, pp. 881-820, 11-15 June, 2012.

Burton, T., Jenkins, N., Sharpe, D. and Bossanyi, E., Wind Energy Handbook, 2nd ed., ***Wiley***, New York, 2011.

Chaudhary, M.K. and Roy, A., "Design and optimization of a small wind turbine blade for operation at low wind speed", ***World Journal of Engineering*** 12 (1), 83-94, 2015.

Clausen, P.D. and Wood, D.H., "Research and development issues for small wind turbines", ***Renewable Energy*** 16 (1-4), 922-927, 1999.

Coleman, H. W. and Steele, Jr., Experimentation and Uncertainty Analysis for Engineers, 2nd ed, ***Wiley***, New York, 1999.

Corda, S., Introduction to Aerospace Engineering with a Flight Test Perspective, ***Wiley***, New York, 2017.

Corke, T., Wind Energy Design, ***CRC Press***, Boca Raton, 2018.

Dehouck, V., Lateb, M., Sacheau, J. and Fellouah, H., "Application of the Blade Element Momentum Theory to Design Horizontal Axis Wind Turbine Blades", ***ASME Journal of Solar Energy Engineering*** 140 (1), 9, 2018.

Discetti, S. and Ianiro, A., Experimental Aerodynamics, ***CRC Press***, Boca Raton, 2017.

DNV GL Energy, ***Energy Transition Outlook 2020 Report - A Global and Regional Forecast to 2050***, Høvik, Norway, 2020.

Donelli, R.S., De Gregorio, F. and Pierluigi, I., "Flow separation control by trapped vortex", ***48th AIAA Aerospace Sciences Meeting Including the New Horizons Forum and Aerospace Exposition***, Orlando, Florida, USA, 04-07 January, 2010.

Duquette, M.M., Swanson, J. and Visser, K.D., "Solidity and blade number effects on a fixed pitch, 50W horizontal axis wind turbine", ***Wind Engineering*** 27 (4), 299-316, 2003.

Earnest, J. and Rachel, S., Wind Power Technology, 3rd ed.,. ***Phi Learning Private Limited***, Delhi, 2019.

Ehrlich, R., Renewable Energy: A First Course, ***CRC Press***, Boca Raton, 2013.

Emeis, S., "Wind Energy Meteorology: Atmospheric Physics for Wind Power Generation", ***Green Energy Technology***, ***Springer-Verlag***, Berlin, 2013.

Eppler, R., Airfoil Design and Data, ***Springer-Verlag***, Berlin, 1990.

EWEA, ***Wind Energy - The Facts***, Brussels, 2009.

Fertis, D.G., "New Airfoil-Design Concept with Improved Aerodynamic

Characteristics", ***ASCE Journal of Aerospace Engineering*** 7 (3), 328-339, 1994.

Finaish, F. and Witherspoon, S., "Aerodynamic Performance of an Airfoil with Step-Induced Vortex for Lift Augmentation", ***ASCE Journal of Aerospace Engineering***, 11 (1), 9-16, 1998.

Fischer, O., Investigation of Correction Methods for Interference Effects in Open-Jet Wind Tunnels, ***Springer Vieweg***, Wiesbaden, 2018.

Pritchard, P.J., Fox and McDonald's Introduction to Fluid Mechanics, 8th ed., ***Wiley***, New York, 2010.

Fuglsang, P. and Bak, C., "Development of the Risø wind turbine airfoils", ***Wiley Wind Energy*** 7 (2), 145-162, 2004.

Gao, X. and Hu, J., "Numerical Research of Reynolds Number Impact on Scale Model of Wind Turbine", ***IEEE 2009 World Non-Grid-Connected Wind Power and Energy Conference***, Nanjing, pp. 1-4, 24-26 September, 2009.

Gasch, R. and Twele, J., Wind Power Plants: Fundamentals, Design, Construction and Operation, 2nd ed., ***Springer-Verlag***, Berlin, 2012.

Giguère, P. and Selig, M.S., "Low Reynolds number airfoils for small horizontal axis wind turbines", ***Wind Engineering*** 21 (6), 367-380, 1997.

Gipe, P., Wind Power: Renewable Energy for Home, Farm, and Business, ***Chelsea Green Publishing***, Chelsea, 2004.

Le Gourieres, D., Wind Power Plants: Theory and Design, ***Pergamon Press***, Oxford, 1982.

Gregorio, F. De and Fraioli, G., "Flow control on a high thickness airfoil by a trapped vortex cavity", ***14th International Symposium Applications of Laser Techniques to Fluid Mechanics***, Lisbon, Portugal, 12, 7-10 July, 2008.

Gudmundsson, S., General Aviation Aircraft Design: Applied Methods and Procedures, ***Butterworth-Heinemann***, Oxford, 2013.

Hansen, K.L., Kelso, R.M. and Dally, B.B., "The effect of leading edge tubercle geometry on the performance of different airfoils", ***7th World Conference on Experimental Heat Transfer, Fluid Mechanics, and Thermodynamics***, Krakow, Poland, 8, 28-03 July, 2009.

Hansen, K.L., Kelso, R.M. and Dally, B.B., "Performance variations of leading-edge tubercles for distinct airfoil profiles", ***AIAA Journal*** 49 (1), 10 , 2011.

Hansen, M.O.L., Aerodynamics of Wind Turbines, 3rd ed., ***Routledge***, London & New York, 2015.

Hasanuzzaman, M. and Rahim, N.A., Energy for Sustainable Development: Demand, Supply, Conversion and Management, ***ACADEMIC PRESS***, London, 2020.

Hau, E., Wind Turbines: Fundamentals, Technologies, Application, Economics, 3rd ed., ***Springer-Verlag***, Berlin, 2013.

Hirahara, H., Hossain, M.Z., Kawahashi, M. and Nonomura, Y., "Testing basic performance of a very small wind turbine designed for multi-purposes", ***Renewable Energy*** 30 (8), 1279-1297, 2005.

Holmes, J.D., Wind Loading of Structures, ***Spon Press***, London, 2001.

Hsiao, F. Bin, Bai, C.J. and Chong, W.T., "The performance test of three different horizontal axis wind turbine (HAWT) blade shapes using experimental and numerical methods", ***Energies*** 6 (6), 2784-2803, 2013.

Husher, J.D., Crises of the 21st Century: Start Drilling-the Year 2020 Is Coming Fast, ***iUniverse***, New York, 2009.

Institution of Mechanical Engineers, The International Vehicle Aerodynamics

Conference, ***Elsevier Science***, Amsterdam, 2014.

Ingram, G., "Wind Turbine Blade Analysis using the Blade Element Momentum Method", Version 1.0, 2011.

Intaratep, N., Borgoltz, A. and Devenport, W.J., "Evaluation of wall interference for 360 degree testing of wind turbine airfoils", ***AIAA Scitech 2019 Forum***, San Diego, California, USA, 14, 7-11 January, 2019.

Iollo, A. and Zannetti, L., "Optimal control of a vortex trapped by an airfoil with a cavity", ***Springer Flow, Turbulence and Combustion*** 65, 417-430, 2000.

Jain, P., Wind Energy Engineering, ***McGraw Hill***, New York, 2010.

Jamieson, P., Innovation in Wind Turbine Design, ***Wiley***, New York, 2011.

Jewel B. Barlow, William H. Rae, A.P., Low-Speed Wind Tunnel Testing, ***Wiley***, New York, 1999.

Jha, A.R., Wind Turbine Technology, ***CRC Press***, Boca Raton, 2010.

Kang, S.-H., Shin, E.S., Ryu, K.-W. and Lee, J., "Separation blockage-correction method for the airfoil of a wind turbine blade", ***Springer Journal of Mechanical Sciences and Technology*** 27,1321-1327, 2013.

Karthikeyan, N. and Suthakar, T., "Computational studies on small wind turbine performance characteristics", ***IOP Journal of Physics: Conference Series*** 759, 6, 2016.

Katz, J., Race Car Aerodynamics : Designing for Speed, 2nd ed., ***Bentley Publication***, Cambridge, 1995.

Katz, J., Automotive Aerodynamics, ***Wiley***, New York, 2016,

Khaled, M., "Aerodynamic Design and Blade Angle Analysis of a Small Horizontal–Axis

Wind Turbine", ***American Journal of Modern Energy*** 3 (2), 23-37, 2017.

King, G.C., Physics of Energy Sources, ***Wiley***, New York, 2018.

Kishore, R., Stewart, C. and Priya, Wind Energy Harvesting: Micro-to-Small Scale Turbines, ***De Gruyter***, Berlin, 2018.

Kishore, R.A., Coudron, T. and Priya, S., "Small-scale wind energy portable turbine (SWEPT)", ***Journal of Wind Engineering and Industrial Aerodynamics*** 116, 21-31, 2013.

Korakianitis, T., Rezaienia, M.A., Shen, X., Avital, E.J., Munjiza, A., Wen, P.H. and Williams, J.J.R., Aerodynamics of Wind Turbine Technology, ***Wiley***, New York, 2015.

Kulunk, E. and Yilmaz, N., "Aerodynamic design and performance analysis of HAWT blades", ***Proceedings of ASME 2009 Fluids Engineering Division Summer Meeting***, Vail, Colorado, USA, pp. 1211-1222, 26 July, 2009.

Kumar Gupta, R., Warudkar, V., Purohit, R. and Singh Rajpurohit, S., "Modeling and Aerodynamic Analysis of Small Scale, Mixed Airfoil Horizontal Axis Wind Turbine Blade", ***Materials Today Proceedings*** 4 (4), 5370-5384, 2017.

Landberg, L., Meteorology for Wind Energy: An Introduction, ***Wiley***, 2015.

Lee, J. and Zhao, F., Wind Energy Technology, ***GWEC Global Wind Report***, Brussels, Belgium 2020.

Letcher, T.M., Wind Energy Engineering: A Handbook for Onshore and Offshore Wind Turbines, ***Elsevier Science***, Amsterdam, 2017.

Liebeck, H.R., Subsonic Airfoil Design, ***American Institute of Aeronautics and Astronautics***, USA, 1990.

Lissaman, P.B.S., "Low-Reynolds-Number Airfoils", ***Annu. Rev. Fluid Mech.*** 15, 223-

239, 1983.

Liu, S. and Janajreh, I., "Development and application of an improved blade element momentum method model on horizontal axis wind turbines", ***Int. J. Energy Environ. Eng.*** 3 (1), 10, 2012.

Lohry, M.W., Clifton, D. and Martinelli, L., "Characterization and design of tubercle leading-edge wings", ***7th Int. Conf. Comput. Fluid Dyn.***, Big Island, Hawaii, 11, 9-13 July, 2012.

Looney, B., Statistical Review of World Energy, ***BP***, London, UK, 2020.

Maalawi, K.Y. and Badr, M.A., "A practical approach for selecting optimum wind rotors", ***Renew. Energy*** 28 (5), 803-822, 2003.

Manwell, J.F., McGowan, J.G. and Rogers, A.L., Wind Energy Explained: Theory, Design and Application, 2nd ed., ***Wiley***, Chichester, 2010.

Mathew, S. and Geeta Susan, P., Advances in Wind Energy Conversion Technology, ***Springer-Verlag***, Berlin, 2011.

Miley, S.J., Catalog of Low Reynolds Number Airfoil Data for Wind Turbine Applications, ***Nation. Tech. Info. Service***, USA, 11, 22-24 March, 1982.

Mo, J. and Rho, B., "Characteristics and effects of laminar separation bubbles on NREL S809 airfoil using the γ-Re_θ transition model" ***Applied Sciences*** 10 (17), 6095, 2020.

Mueller, T.J. and Jansen, J.B., "Aerodynamic Measurements at Low Reynolds Numbers", ***12th Aerodynamic Testing Conference***, Williamsburg, Virginia, USA, 1982.

Muhsen, H., Al-Kouz, W. and Khan, W., "Small wind turbine blade design and optimization", ***Symmetry*** 12 (1), 14, 2020.

Nelson, V., Wind Energy: Renewable Energy and the Environment, 2nd ed., ***CRC Press***,

Boca Raton, 2013.

Nelson, V. and Starcher, K., Wind Energy: Renewable Energy and the Environment, 3rd ed., ***CRC Press***, Boca Raton, 2018.

Ng, B.F., New, T.H.D. and Palacios, R., "Bio-inspired Leading-Edge Tubercles to Improve Fatigue Life in Horizontal Axis Wind Turbine Blades", ***35th Wind Energy Symp.***, Grapevine, Texas, USA, 11, 9-13 January, 2017.

Ni, Z., Su, T.C. and Dhanak, M., "An empirically-based model for the lift coefficients of twisted airfoils with leading-edge tubercles", ***AIP Adv.*** 8 (4), 16, 2018.

Olsman, W.F.J. and Colonius, T., "Numerical simulation of flow over an airfoil with a cavity", ***AIAA J.*** 49 (1), 7, 2011.

Osei, E.Y., Opoku, R., Sunnu, A.K. and Adaramola, M.S., "Development of High Performance Airfoils for Application in Small Wind Turbine Power Generation", ***Hindawi J. Energy*** 2020, 9, 2020.

Paraschivoiu, I., Wind Turbine Design: With Emphasis on Darrieus Concept, ***Polytechnic International Press***, Montreal, 2002.

Pechlivanoglou, G., Passive and active flow control solutions for wind turbine blades, PhD Thesis, ***TU Berlin***, Berlin, 236, 2012.

Pelletier, A. and Mueller, T.J., "Effect of endplates on two-dimensional airfoil testing at low Reynolds number", ***J. Aircr.*** 38 (6), 4, 2001.

Philip Barnes, J., "Math modeling of airfoil geometry", ***SAE Tech. Pap. Ser.***, 19, 1996.

Pierce, K.G. and Migliore, P.G., "Maximizing energy capture of fixed-pitch variable-speed wind turbines", ***2000 ASME Wind Energy Symp.*** Reno, Nevada, USA, 10, 10-13 January, 2000.

Prabhukhot, P.R. and Prabhukhot, A.R., "Computer analysis of S822 aerofoil section for blades of small wind turbines at low wind speed", ***ASME J. Sol. Energy Eng. Trans.*** 139 (5), 4, 2017.

Qu, H., Hu, J. and Gao, X., "The impact of Reynolds number on two-dimensional aerodynamic airfoil flow", ***IEEE 2009 World Non-Grid-Connected Wind Power Energy Conf.***, Nanjing, China, 2009.

Ragheb, M. and M., A., Wind Turbines Theory - The Betz Equation and Optimal Rotor Tip Speed Ratio, ***IntechOpen***, London, 2011.

Rao, K.R., Wind Energy for Power Generation: Meeting the Challenge of Practical Implementation, ***Springer***, Cham, 2019.

Rehman, S., Mahbub Alam, M., Alhems, L.M. and Mujahid Rafique, M., "Horizontal AxisWind Turbine Blade Design Methodologies for Efficiency Enhancement A Review", ***Energies*** 11 (3), 30, 2018.

Reible, D.D., Fundamentals of Environmental Engineering, ***CRC Press***, Boca Raton, 2017.

Reynolds, S.J., Rohli, R. V., Johnson, J.K., Waylen, P.R. and Francek, M.A., Exploring Physical Geography, 2nd ed., ***McGraw-Hill***, New York, 2017,

Rosato, M.A., Small Wind Turbines for Electricity and Irrigation, ***CRC Press***, Boca Raton, 2018.

Sawhney, G.S., Nonconventional Resources of Energy, ***PhiLearning Private Limited***, Delhi, 2012,

Schaffarczyk, A.P., "Introduction to Wind Turbine Aerodynamics", ***Springer-Verlag***, Berlin, 2014.

Schmitz, S., Aerodynamics of Wind Turbines: A Physical Basis for Analysis and Design,

Wiley, New York, 2020.

Schubel, P.J. and Crossley, R.J., Wind turbine blade design, ***CRC Press***, Boca Raton, 2014.

Selig, M., Deters, R. and Wiliamson, G., "Wind Tunnel Testing Airfoils at Low Reynolds Numbers", **49th AIAA Aerospace Sciences Meeting**, Orlando, Florida, USA, 32, 04-07 January, 2011.

Selig, M.S. and Guglielmot, J.J., "High-lift low Reynolds number airfoil design", ***J. Aircr.*** 34 (1), 72-79, 1997.

Serdar Genç, M., Koca, K., Demir, H. and Hakan Açıkel, H., Traditional and New Types of Passive Flow Control Techniques to Pave the Way for High Maneuverability and Low Structural Weight for UAVs and MAVs, ***IntechOpen***, London, 2020.

Shah, H., Bhattarai, N., Mathew, S. and Lim, C.M., "Low Reynolds Number Airfoil for Small Horizontal Axis Wind Turbine Blades", ***Wind Eng.***, 21 (6), 367-380, 1997.

Shi, S., New, T.H. and Liu, Y., "On the flow behaviour of a vortex-trapping cavity NACA0020 aerofoil at ultra-low Reynolds number", ***17th Int. Symp. Appl. Laser Tech. to Fluid Mech.***, Lisbon, Portugal, 12, 07-10 July, 2014.

Singh, R.K., Ahmed, M.R., Zullah, M.A. and Lee, Y.H., "Design of a low Reynolds number airfoil for small horizontal axis wind turbines", ***Renew. Energy*** 42, 66–76, 2012.

Spera, D.A., Wind Turbine Technology: Fundamental Concepts of Wind Turbine Engineering, ***ASME Press***, New York, 2009.

Sumathi, S., Ashok Kumar, L. and Surekha, P., Solar PV and Wind Energy Conversion Systems, ***Springer***, Cham, 2015.

Tahir, A., Elgabaili, M., Rajab, Z., Buaossa, N., Khalil, A. and Mohamed, F., "Optimization of small wind turbine blades using improved blade element momentum

theory", ***Wind Eng.*** 43 (3), 299-310, 2019.

Tangler, J. and Somers, D., NREL airfoil families for HAWTs, ***Technical Report***, USA, 1995.

Timmer, W.A. and Van Rooij, R.P.J.O.M., "Summary of the Delft University wind turbine dedicated airfoils", ***ASME J. Sol. Energy Eng.*** 125 (4), 488-496, 2003.

Timmer, W.A. and Bak, C., Aerodynamic characteristics of wind turbine blade airfoils, ***Woodhead Publishing***, Cambridge, 2013.

Van Treuren, K.W., "Small-scale wind turbine testing in wind tunnels under low reynolds number conditions", ***ASME J. Energy Resour. Technol.*** 137 (5), 11, 2015.

Van Treuren, K.W., "Small horizontal axis wind turbines: Current status and future challenges", ***Proc. ASME Turbo Expo 2016: Turb. Tech. Conf. Expo.***, Seoul, South Korea, 12, 13-17 June, 2016.

Tropea, C., Yarin, A.L. and Foss, J.F., Springer Handbook of Experimental Fluid Mechanics, ***Springer Verlag***, Berlin, 2007.

Twidell, J. and Weir, T., Renewable Energy Resources, 2nd ed., ***Taylor & Francis***, London, 2006.

EIA International Energy Outlook 20019, ***Annu. Energy Outlook 2019 with Proj. to 2050***, Washington, USA, 2019.

Vaidyanathan, A., Kingman, D. and Kurth, T., "When do endplates work?", ***52nd Aerosp. Sci. Meet.***, National Harbor, Maryland, USA, 11, 13-17 January, 2014.

Wagner, H.J., "Introduction to wind energy systems", ***EPJ Web Conf.*** 189, Varenna, Italy, 16, 21-26 July, 2018.

Wang, J. and Feng, L., Flow Control Techniques and Applications, ***Cambridge***

University Press, Cambridge, 2018.

Wang, L., Tang, X. and Liu, X., "Blade Design Optimisation for Fixed-Pitch Fixed-Speed Wind Turbines", ***ISRN Renew. Energy*** 2012, 8, 2012.

Wata, J., Faizal, M., Talu, B., Vanawalu, L., Sotia, P. and Ahmed, M.R., "Studies on a low Reynolds number airfoil for small wind turbine applications", ***Sci. China Technol. Sci.*** 54, 1684-1688, 2011.

Watts, P. and Fish, F.E., "The influence of passive, leading edge tubercles on wing performance", ***Proc. 12th Intl. Symp. Unmanned Untethered Submers. Technol.***, Durham, New Hampshire, USA, 2001.

Wei, Z., New, T.H. and Cui, Y.D., "An experimental study on flow separation control of hydrofoils with leading-edge tubercles at low Reynolds number", ***Ocean Eng.*** 108, 336-349, 2015.

Winslow, J., Otsuka, H., Govindarajan, B. and Chopra, I., "Basic understanding of airfoil characteristics at low Reynolds numbers (10^4–10^5)", ***J. Aircr.*** 55 (3), 1050-1061, 2018.

Witherspoon, S. and Finaisht, F., "Experimental and computational studies of flow developments around an airfoil with backward-facing steps", ***14th Appl. Aerodyn. Conf.***, New Orleans, Louisiana, USA, 11, 17-20 June, 1996.

Wizelius, T., Developing Wind Power Projects: Theory and Practice, ***Earthscan***, Sterling, 2015.

Wood, D., Small Wind Turbines: Analysis, Design, and Application, ***Springer***, London, 2011.

Xiao, Z., Zhao, Q., Yang, X. and Zhu, A.F., "A power performance online assessment method of a wind turbine based on the probabilistic area metric", ***Appl. Sci.*** 10 (9), 18, 2020.

URL-1: “The wavy shape of the humpback whale flippers”, https://en.wikipedia.org/wiki/Flipper_(anatomy)#/media/File:Humpback_stellwagen.JPG, 19.02.2021.

URL-2: “Wind turbine components”, https://str.llnl.gov/april-2014/miller, 10.12.2018.

URL-3: “Wind turbine types”, https://www.klein-windkraftanlagen.com/technik/vertikale-windkraftanlagen, 15.12.2020.

APPENDICES

App-A Uncertainty analysis applied to airfoil tunnel testing

The experimental result r as a function of measured variables according to Pritchard (2010) is given by:

$$r = r\left(X_1, X_2, \dots, X_J\right) \tag{A.1}$$

Where X_i denotes measured independent variable.

The general expression for computing the relative uncertainty of the result regarding to Eq. A.1, is given by the formula:

$$U_r = \pm\sqrt{\left(\frac{X_1}{r}\cdot\frac{\partial r}{\partial X_1}\cdot U_{X_1}\right)^2 + \left(\frac{X_2}{r}\cdot\frac{\partial r}{\partial X_2}\cdot U_{X_2}\right)^2 + \cdots} \tag{A.2}$$

Where U_{X_i} stands for relative uncertainty of measured variable X_i.

According to Coleman and Steele (1998), in the case when experimental parameters are expressed in the form:

$$r = kX_1^a X_2^b X_3^c \dots \tag{A.3}$$

where *k* is a constant, X_i^j is the measured value of an independent variable raised to power;

The relative uncertainty of the experimental result *r* is expressed as:

$$U_r = \frac{W_r}{r} = \sqrt{a^2\left(U_{x_1}\right)^2 + b^2\left(U_{x_2}\right)^2 + c^2\left(U_{x_3}\right)^2 + \cdots} \tag{A.4}$$

App-A (Continue) Uncertainty analysis applied to airfoil tunnel testing

Where U_{X_i} - denotes uncertainty of measured independent variable X_i.

In this study, quantities such as free stream speed, force, density, temperature, etc., were measured experimentally. With the help of these experimental results obtained, several nondimensional parameters such as Reynolds number, lift and drag force coefficients, were determined according to Akbıyık (2014) approach.

Other variables used in this study are atmospheric pressure (P_{atm}), air temperature (T_∞), air density (ρ), air viscosity (μ), airfoil chord length (c), airfoil length (b), airfoil thickness ($t = 0.16 \cdot c$), lift force (F_L), drag force (F_D), free stream velocity measured with a pitot-static tube.

Uncertainty in the measurement of atmospheric pressure

According to the manufacturer's technical specifications for micromanometer model ManoAir500-2, an error of 1 kPa may occur in the measurement of 86 kPa atmospheric pressure. In this case the uncertainty of the atmospheric pressure is 1.2%;

$$U_{P_{atm}} = \frac{W_{P_{atm}}}{P_{atm}} = \frac{1000}{86000} = 0.012 = 1.2\% \tag{A.5}$$

Uncertainty in the measurement of air temperature

The ManoAir500 micromanometer model manual states that the accuracy of the temperature probe in measuring the temperature from 0 to 70 °C is 0.2 °C. In this case, the uncertainty of the temperature measured at 27 °C is not 0.7%, but 0.067% because the temperature used is in Kelvin;

$$U_{T_\infty} = \frac{W_{T_\infty}}{T_\infty} = \frac{0.2}{(T_\infty + K)} = \frac{0.2}{300} = 0.000666 = 0.067\% \tag{A.6}$$

App-A (Continue) Uncertainty analysis applied to airfoil tunnel testing

Uncertainty in the measurement of chord length of airfoil S822

The uncertainty due to 1 mm error in measuring the chord length of airfoil of 150 mm is 0.67%;

$$U_c = \frac{W_c}{c} = \frac{1}{150} = 0.00666 = 0.67\% \quad \text{(A.7)}$$

Uncertainty in the measurement of length of airfoil S822

The uncertainty of 0.2 mm in measuring the airfoil length of 450 mm is 0.044%;

$$U_L = \frac{W_L}{L} = \frac{0.2}{450} = 0.000444 = 0.044\% \quad \text{(A.8)}$$

Uncertainty in the measurement of the thickness of airfoils S822

The relative uncertainty of the thickness of airfoil is 0.83%:

$$U_t = \frac{W_t}{t} = \frac{0.2}{0.16 \cdot 150} = \frac{0.2}{24} = 0.00833 = 0.83\% \quad \text{(A.9)}$$

Uncertainty in the measurement of air dynamic viscosity

The relative uncertainty in air dynamic viscosity at 25 °C with the change of 2 °C is 0.51%;

$$U_\mu = \frac{W_\mu}{\mu} = 0.0051 = 0.51\% \quad \text{(A.10)}$$

App-A (Continue) Uncertainty analysis applied to airfoil tunnel testing

Uncertainty in the measurement of air density

The uncertainty value of the air density varies depending on the atmospheric pressure and the temperature. The air density is defined as:

$$\rho = \frac{P_{atm}}{R \cdot T_{\infty}} = \frac{86000}{287 \cdot (27 + 273)} \cong 1 \ \frac{kg}{m^3} \tag{A.11}$$

The uncertainty equation for air density according to Eq. A.4 is expressed as:

$$U_{\rho} = \frac{W_{\rho}}{\rho} = \left[(1)^2\left(U_{P_{atm}}\right)^2 + (-1)^2\left(U_{T_{\infty}}\right)^2\right]^{1/2} = 0.012 = 1.2\% \tag{A.12}$$

Uncertainty in the measurement of frontal area view of airfoil S822

The relative uncertainty of the frontal area view of airfoil S822 according to Eq. A.3 is expressed as:

$$U_{A_F} = \frac{W_{A_F}}{A_F} = [(U_t)^2 + (U_L)^2]^{1/2} = 0.00835658 = 0.84\% \tag{A.13}$$

Uncertainty in the measurement of lift force

Uncertainty values affecting the lift force component are obtained for Reynolds number of $1 \cdot 10^5$ corresponding to wind speed of 12.7 m/s;

X_1 – Uncertainty value in the lift force measurement in the load cell is 0.06%; Load cell uncertainty is obtained from the manufacturer's calibration datasheet for the lift force of 4.87 N at design angle of attack of 8° is 0.4%;

$$U_{X_1} = \frac{W_{X_1}}{X_1} = \frac{32 \cdot 0.0006}{4.87} = 0.0039 = 0.4\% \tag{A.14}$$

App-A (Continue) Uncertainty analysis applied to airfoil tunnel testing

X_1 – Uncertainty for ±1° angle of attack adjustment deviation error;

X_2 – The uncertainty in the lift force quantity measured as 5.08 N at 9 and 4.49 at 7 is 6.1%; Force change for 2° angle of attack is 5.08 - 4.49 = 0.59 N. In the case of 1° angle of attack adjustment bias has an error of W_{X_2} = 0.295 N. X_2 = 4.785 N;

$$U_{X_2} = \frac{W_{X_2}}{X_2} = \frac{0.295}{4.785} = 0.061 = 6.1\% \tag{A.15}$$

The total uncertainty in lift force measurement considering the uncertainty values from X_1 through X_2, is 6.2%;

$$U_{F_L} = \frac{W_{F_L}}{F_L} = \left[\left(\frac{W_{X_1}}{X_1}\right)^2 + \left(\frac{W_{X_2}}{X_2}\right)^2\right]^{1/2} = 0.062 = 6.2\% \tag{A.16}$$

Uncertainty in the measurement of drag force

Uncertainty values affecting the lift force component are obtained for Reynolds number of $1 \cdot 10^5$ corresponding to wind speed of 12.7 m/s;

X_3 – Uncertainty value in the lift force measurement in the load cell is 0.06%; Load cell uncertainty is obtained from the manufacturer's calibration datasheet for the lift force of 0.2405 N at design angle of attack of 8° is 8%;

$$U_{X_3} = \frac{W_{X_3}}{X_3} = \frac{32 \cdot 0.0006}{0.2405} = 0.0798 = 8\% \tag{A.17}$$

X_3 – Uncertainty for ±1° angle of attack adjustment deviation error;

X_4 – The uncertainty in the lift force quantity measured as 0.250 N at 9 and 0.255 at 7 is 5.5%; In the case of 1° angle of attack adjustment bias has an error of W_{X_4} = 0.014 N; X_4 = 0.253 N;

$$U_{X_4} = \frac{W_{X_4}}{X_4} = \frac{0.014}{0.253} = 0.0553 = 5.5\% \tag{A.18}$$

The total uncertainty in lift force measurement considering the uncertainty values from X_3 through X_4, is 6.2%;

$$U_{F_D} = \frac{W_{F_D}}{F_D} = \left[\left(\frac{W_{X_3}}{X_3}\right)^2 + \left(\frac{W_{X_4}}{X_4}\right)^2\right]^{1/2} = 0.097 = 9.7\% \tag{A.19}$$

Uncertainty in the measurement of velocity by the pitot-static tube micromanometer

Uncertainty values affecting the velocity measurement with static-pitot tube are obtained for Reynolds number of $5 \cdot 10^4$ corresponding to wind speed of 6.4 m/s.

X_5 – Uncertainty in the pitot-static tube considering the accuracy of ±0.5 Pa of the measuring device ManoAir 500 according to Eq. A.4 is 1.34%;

$$U_{\Delta p} = \frac{0.5}{\frac{1}{2} \cdot \frac{P_{atm}}{R \cdot (T_\infty + K)} \cdot \mathrm{V}^2} = \frac{0.5}{\frac{1}{2} \cdot \frac{86000}{287 \cdot (27 + 273)} \cdot 6.4^2} = 0.024 = 2.4\% \tag{A.20}$$

$$U_{V_{pitot}} = \frac{W_{V_{pitot}}}{V_{pitot}} = \left[\left(\frac{1}{2}\right)^2 \left(U_{\Delta p}\right)^2 + \left(-\frac{1}{2}\right)^2 \left(U_\rho\right)^2\right]^{1/2} = 0.0134 = 1.34\% \tag{A.21}$$

Uncertainty in measuring the Reynolds number

The uncertainty value for the Reynolds number varies depending on the air density, relative flow velocity, chord length, and viscosity according to Eq. A4 is obtained as:

$$U_{Re} = \frac{W_{Re}}{Re} = \left[\left(U_\rho\right)^2 + \left(U_{V_{pitot}}\right)^2 + (U_c)^2 + \left(U_\mu\right)^2\right]^{1/2}$$
$$= [(0.012)^2 + (0.0134)^2 + (0.00666)^2 + (0.0051)^2]^{1/2} \quad \text{(A.22)}$$
$$= 1.9\%$$

Uncertainty in the measurement of lift force coefficient

The uncertainty value for the lift force coefficient varies depending on the lift force, air density, relative flow velocity, and frontal view area of airfoil according to Eq. A.4 is obtained as:

$$U_{C_L} = \frac{W_{C_L}}{C_L} = \left[\left(U_{F_L}\right)^2 + \left(U_\rho\right)^2 + 4\left(U_{V_{pitot}}\right)^2 + \left(U_{A_F}\right)^2\right]^{1/2}$$
$$= [(0.062)^2 + (0.012)^2 + 4(0.0134)^2 + (0.00835)^2]^{1/2} \quad \text{(A.23)}$$
$$= 0.0691 = 6.9\%$$

Uncertainty in the measurement of drag force coefficient

The uncertainty value for the drag force coefficient varies depending on the lift force, air density, relative flow velocity, and frontal view area of airfoil according to Eq. A.4 is obtained as:

$$U_{C_D} = \frac{W_{C_D}}{C_D} = \left[\left(U_{F_D}\right)^2 + \left(U_\rho\right)^2 + 4\left(U_{V_{pitot}}\right)^2 + \left(U_{A_F}\right)^2\right]^{1/2}$$
$$= [(0.097)^2 + (0.012)^2 + 4(0.0134)^2 + (0.00835)^2]^{1/2} \quad \text{(A.24)}$$
$$= 0.102 \cong 10.2\%$$

App-B Uncertainty analysis applied to wind turbine tunnel testing

Uncertainty values for the three main wind turbine design parameters such as tip speed ratio (λ), power coefficient (C_p), and Reynolds number (Re) were obtained for maximum performance condition of the baseline model (M1) under tip chord-based Reynolds number of $4.7 \cdot 10^4$ corresponding to free stream speed V = 11.29 m/s, blade tip speed of V_R = 42 m/s, shaft speed of 2866 rpm, air density of ~1 kg/m^3, atmospheric pressure of 86 kPa, and temperature of 27 °C.

In this study, uncertainties of these three main design parameters were determined: tip speed ratio, power coefficient, and Reynolds number.

Uncertainty in the measurement of tip speed ratio

The uncertainty equation for tip speed ratio according to Eq. A.4, is expressed as:

$$U_\lambda = \frac{w_\lambda}{\lambda} = \left[(1)^2\left(U_{V_R}\right)^2 + (-1)^2(U_V)^2\right]^{1/2} \tag{A.25}$$

Where;

U_{V_R} – Uncertainty value in the rotating blade speed based on the accuracy of the measuring device in the range (±0.5% + 1) according to Eq. A.4 is 0.554%;

$$U_{V_R} = \frac{W_{V_R}}{V_R} = [(U_n)^2 + (U_R)^2]^{1/2} = [(0.00535)^2 + (0.00143)^2]^{1/2} = 0.00554 = 0.554\% \tag{A.26}$$

U_n – Uncertainty value in the number of rotations of the rotor shaft measurement based on the accuracy of the torque sensor device range (±0.5% + 1) is 0.535%;

$$U_n = \frac{W_n}{n} = \frac{0.005 \cdot 2866 + 1}{2866} = \frac{15.33}{2866} = 0.00535 = 0.535\% \tag{A.27}$$

App-B (Continue) Uncertainty analysis applied to wind turbine tunnel testing

U_R – Uncertainty value due to an error of +0.2 mm in measuring the rotor radius of 140 mm and based on the device accuracy specifications (1/1000) is 0.143%;

$$U_R = \frac{W_R}{R} = \frac{0.0002}{0.14} = 0.00143 = 0.143\% \tag{A.28}$$

U_V – Uncertainty value in measuring the freestream velocity considering other inaccuracies of 1% according to Eq. A.4 is 1.3%;

$$U_V = \frac{W_V}{V} = \left[\left(U_{\Delta p}\right)^2 + (0.01)^2\right]^{1/2} = [(0.00785)^2 + (0.01)^2]^{1/2} = 0.013 = 1.3\% \tag{A.29}$$

$U_{\Delta p}$ – Uncertainty in the dynamic fluid pressure flowing at speed of 11.29 m/s considering the accuracy of ±0.5 Pa of the measuring device ManoAir 500 is 0.785%;

$$U_{\Delta p} = \frac{W_{\Delta p}}{\Delta p} = \frac{0.5}{\frac{1}{2} \cdot \frac{P_{atm}}{R \cdot (T_\infty + K)} \cdot \mathrm{V}^2} = \frac{0.5}{63.658} = 0.00785 = 0.785\% \tag{A.30}$$

The total uncertainty in the tip speed ratio measurement according to Eq. A.4 is 1.41%;

$$U_\lambda = \frac{W_\lambda}{\lambda} = [(0.00554)^2 + (0.013)^2]^{1/2} = 0.0141 = 1.41\% \tag{A.31}$$

Uncertainty in the measurement of power coefficient

The uncertainty equation for power coefficient according to Eq. A.4 is expressed as:

$$U_{C_p} = \frac{w_{C_p}}{C_p} = \left[(1)^2(U_n)^2 + (1)^2\left(U_Q\right)^2 + (-1)^2\left(U_\rho\right)^2 + (-2)^2(U_D)^2 + (-3)^2(U_V)^2\right]^{1/2} \quad \text{(A.32)}$$

Where;

Uncertainty values for $U_\rho = 1.2\%$, $U_n = 0.535\%$, and $U_V = 1.3\%$ are known from Eqs. A.12, A.36, and A.38 respectively;

U_Q – Uncertainty value in the torque magnitude of 0.0586 Nm according to the device accuracy range of ±0.1% is 0.1%;

$$U_Q = \frac{W_Q}{Q} = \frac{0.0000586}{0.0586} = 0.001 = 0.1\% \quad \text{(A.33)}$$

U_D – Uncertainty value due to an error of +0.2 mm in measuring the rotor diameter of 280 mm and based on the device accuracy specifications (1/1000) is 0.0714%;

$$U_D = \frac{W_D}{D} = \frac{0.0002}{0.28} = 0.000714 = 0.0714\% \quad \text{(A.34)}$$

The total uncertainty according to Eq. A.43 in power coefficient is 4.1%;

$$U_{C_p} = \frac{w_{C_p}}{C_p} = [(0.00554)^2 + (0.001)^2 + (0.012)^2 + 4(0.000714)^2 + 9(0.013)^2]^{1/2} = 0.041 = 4.1\% \quad \text{(A.35)}$$

Uncertainty in the measurement of Reynolds number

The uncertainty equation for Reynolds number according to Eq. A.4, is expressed as:

$$U_{Re} = \frac{W_{Re}}{Re} = \left[(1)^2\left(U_\rho\right)^2 + (1)^2\left(U_{V_{rel}}\right)^2 + (1)^2\left(U_{c_{11}}\right)^2 + (-1)^2\left(U_\mu\right)^2\right]^{1/2} \quad \text{(A.36)}$$

Where;

Uncertainty values for $U_\mu = 0.51\%$, $U_\rho = 1.2\%$, and $U_V = 1.3\%$ are known from the Eqs. A.10, A.12, A.36, and A.38 respectively;

$U_{V_{rel}}$ – Uncertainty in the relative wind velocity obtained according to Eq. A.2 is 0.633%:

$$U_{V_{rel}} = \sqrt{\left(\frac{V^2}{V^2 + {V_R}^2} \cdot {U_V}^2\right) + \left(\frac{{V_R}^2}{V^2 + {V_R}^2} \cdot {U_{V_R}}^2\right)} = 0.00633 = 0.633\% \quad \text{(A.37)}$$

$U_{c_{11}}$ – Uncertainty value due to an error of +0.2 mm in measuring the blade tip chord length c_{11} = 20 mm and based on the device accuracy specifications (1/1000) is 1%;

$$U_{c_{11}} = \frac{W_{c_{11}}}{c_{11}} = \frac{0.0002}{0.02} = 0.01 = 1\% \quad \text{(A.38)}$$

The total uncertainty according to Eq. A.4 in Reynolds number is 1.8%;

$$U_{Re} = \frac{W_{Re}}{Re} = [(0.012)^2 + (0.00633)^2 + (0.01)^2 + (0.0051)^2]^{1/2} = 0.018 = 1.8\% \quad \text{(A.39)}$$

PUBLICATIONS PRODUCED DURING THESIS WORK

From this thesis, 1 (one) paper were produced. The produced study is provided below.

Morina, R. and Akansu, Y.E., “Effects of leading edge wavy shape on a horizontal axis wind turbine blade at low speed conditions”, Manuscript prepared to be submitted to a SCI-expanded Journal, 2021.